Application of Rarefied Gas Dynamics to the Head-Disk Interface in Hard Disk Drives

By

Nan Liu

A dissertation submitted in partial satisfaction of the

requirements for the degree of

Doctor of Philosophy

in

Engineering–Mechanical Engineering

in the

Graduate Division

of the

University of California, Berkeley

Committee in charge:

Professor David B. Bogy, Chair
Professor James Casey
Professor Tarek I. Zohdi
Professor Jon Wilkening

Fall 2010

The dissertation of Nan Liu, titled Application of Rarefied Gas Dynamics to the Head-Disk Interface in Hard Disk Drives, is approved:

Chair D Bogy Date 6/10/2010

Ian Wilding Date 5/10/2010

Tarek Zohdi Date 5/10/2010

James Casey Date 7 June 2010

University of California, Berkeley

Application of Rarefied Gas Dynamics to the Head-Disk Interface in Hard Disk Drives

by

Nan Liu

Abstract

Application of Rarefied Gas Dynamics to the Head-Disk Interface in Hard Disk Drives

by

Nan Liu

Doctor of Philosophy in Engineering–Mechanical Engineering

University of California, Berkeley

Professor David B. Bogy, Chair

To compete with solid state drives (SSDs), hard disk drives (HDDs) must improve their performance in capacity, speed and reliability, which requires the spacing between the magnetic disk, used to store information, and the magnetic transducer, used to read information from and write information onto the disk, to decrease. This distance is now approaching 5nm, and, accordingly, the distance between a slider, embedding the transducer, and the disk ranges from several nanometers to several micrometers, which makes the gas flowing between the slider and the disk rarefied. This dissertation applies rarefied gas dynamics to investigate several issues related to HDDs' performance.

Particle contamination on the slider may scratch the disk and induce loss of data. An improved model is proposed to numerically study particle contamination on a thermal flying-height control (TFC) slider, which adjusts the transducer-disk spacing by use of a small heater embedded in the slider near the transducer. It is found that the currently used model is sufficiently accurate despite its simple form.

The temperature increase inside HDDs during operation may affect their reliability. This dissertation derives an analytical formula for the gas-flow induced shear force in the head-disk interface (HDI) and uses it to investigate how the raised temperature affects the slider's flying attitude and the shear forces on the slider and the disk.

Numerical prediction of a TFC slider's flying performance lays the foundation for commercial designs of TFC sliders. An improved model is proposed to calculate the heat flux on the TFC slider and it is found that the currently used model is accurate enough for this purpose. Finally, a general approach is proposed to numerically investigate a TFC slider flying in gas mixtures.

To my parents

Contents

List of Figures iv

List of Tables vii

1 Introduction 1
- 1.1 Brief history and structure of hard disk drives . . . 1
- 1.2 Structure of a modern hard disk drive . . . 4
- 1.3 Rarefied gas dynamics . . . 7
- 1.4 Motivation and organization of the dissertation . . . 9

2 Boundary effect on slider particle contamination 10
- 2.1 Introduction . . . 10
- 2.2 Numerical study of a particle's motion in the HDI . . . 11
- 2.3 Boundary effect on a particle's motion in the HDI . . . 12
- 2.4 Contamination criterion . . . 15
- 2.5 Integration scheme . . . 16
- 2.6 Numerical results and discussion . . . 17
- 2.7 Summary and conclusion . . . 18

3 Lift force on a rotating particle in a shear flow of a highly rarefied gas 20
- 3.1 Introduction . . . 20
- 3.2 Statement of the problem . . . 21
- 3.3 Forces on a unit area on the surface of the sphere . . . 23
- 3.4 Special case: the axis of rotation is the same as the gradient of the shear flow 24
- 3.5 General case: the axis of rotation may be different from the gradient of the shear flow . . . 26
- 3.6 Conclusion . . . 29

4 Effect of lift force on particle contamination on a slider 30
- 4.1 Introduction . . . 30
- 4.2 Statement of the problem . . . 31
- 4.3 Lift force due to a nonuniform flow field . . . 34
- 4.4 Effect of lift force on a particle's motion in the HDI . . . 35
- 4.5 Summary and conclusion . . . 37

5 Particle contamination on a TFC slider **38**
5.1 Introduction . . . 38
5.2 Theory . . . 39
5.2.1 Temperature field in the HDI . . . 39
5.2.2 Thermophoretic force . . . 40
5.2.3 Simulation of a particle's motion in the HDI . . . 41
5.3 Results and discussions . . . 41
5.4 Summary and conclusion . . . 44

6 Temperature effect on a HDD slider's flying performance at steady state **45**
6.1 Introduction . . . 45
6.2 Shear forces on the slider and the disk . . . 46
6.3 The generalized Reynolds equation and the variable soft sphere (VSS) model 49
6.3.1 The generalized Reynolds equation . . . 49
6.3.2 The variable soft sphere (VSS) Model . . . 50
6.4 Results and discussion . . . 51
6.5 Summary and conclusion . . . 55

7 Numerical prediction of a TFC slider's flying performance **57**
7.1 Introduction . . . 57
7.2 Heat conduction between a slider and a disk . . . 59
7.3 Viscous heating . . . 61
7.3.1 Viscous heating in Couette flow . . . 62
7.3.2 Viscous heating in Poiseuille flow . . . 63
7.4 Importance of heat dissipation compared to heat conduction . . . 66
7.4.1 Importance of heat dissipation due to the Couette flow part . . . 66
7.4.2 Importance of heat dissipation due to the Poiseuille flow part . . . 66
7.5 Accuracy of the currently used heat conduction model . . . 67
7.6 Summary and conclusion . . . 71

8 TFC sliders in air-helium gas mixtures **72**
8.1 Introduction . . . 72
8.2 Numerical approach . . . 73
8.3 Physical properties of gas mixtures . . . 74
8.4 Results and discussion . . . 76
8.5 Summary and conclusion . . . 81

9 Summary and conclusion **82**

List of Figures

1.1 The first hard disk drive. [Wikipedia 2010] . . . 2
1.2 Sketch showing the working principle of the first hard disk drive. . . . 2
1.3 Increase of HDDs' areal density since their invention. The major technological innovations that enable the increase are also shown in the figure. [HGST 2010; INSIC 2010] . . . 3
1.4 Increase of HDDs' mean time between failure (MTBF) in recent years. [HGST 2010] . . . 4
1.5 A modern HDD with upper cover removed. PCGuide [2010] . . . 5
1.6 Structure of a magnetic disk and a thermal flying height control (TFC) slider in a HDD. . . . 6
1.7 A typical air bearing surface (ABS). Different color denotes different etching depth. . . . 7

2.1 A sketch of the head-disk interface showing the recess region. . . . 11
2.2 A particle moving near a boundary, where R is the particle radius and δ is the gap between the particle and the boundary. . . . 13
2.3 Comparison of Eq. (2.5) with the exact results. . . . 14
2.4 A particle moving between two boundaries, where d the distance between the two walls. . . . 15
2.5 Comparison of Eq. (2.7) with numerical results obtained by boundary collocation method for a particle moving at a relative speed U perpendicular to two parallel walls. . . . 16
2.6 Accuracy of using different time steps to calculate a particle's trajectory. . . . 17
2.7 A particle's trajectories for two cases: including the boundary effect and excluding the boundary effect. . . . 18
2.8 Comparison of the present contamination profile (a) and that obtained previously with a limited correction factor for the boundary effect. . . . 19

3.1 The two coordinate systems set up for a spherical particle rotating at angular velocity Ω in a linear shear flow of a highly rarefied gas with the gradient of the shear being G. Note the axis of rotation is not necessarily parallel to the gradient direction . . . 22

4.1 The coordinate system . . . 31

4.2 The drag and lift forces as well as the torque on a sphere with slip flow. Each quantity is nondimensionalized by its value with no slip. Kn $= \mu/\beta R$ for a sphere moving in a rarefied gas and Kn $= \lambda_s/R$ for a sphere with hydrophobic or porous surfaces. 36

5.1 A particle moving into the HDI between a TFC slider and a disk. The slider's flying height, h, at the leading edge is around 300nm while that at the trailing edge can be as low as 10nm. A coordinate system is set up with the z axis perpendicular to the disk. Note: This figure is not to scale 38
5.2 A typical temperature profile in the head-disk interface. Here $\lambda = 65$nm, $h = 1\mu$m, $T_s = 40°$C and $T_d = 20°$C. Due to the discontinuity of temperature at the boundary, the temperature near the disk is different from the temperature of the disk. 40
5.3 The profile of the air bearing surface used in the calculation of particle trajectories in the head-disk interface. Different color denotes different etching depth. 42
5.4 Typical particle's trajectories in the head-disk interface. The two trajectories superpose on each other. Here h_m is a nominal flying height used as a reference value to normalize z. 42

6.1 Collision between two air molecules with relative speed c_r. Here b is the projected distance, χ is the angle after collision, and d is the diameter of air molecules. 50
6.2 Air bearing surface (ABS) of slider A and slider B. Both sliders are Femto sliders (with length $l = 0.85$mm and width $b = 0.7$mm). Different colors correspond to difference etching depths. 52
6.3 Change of the slider's flying height (FH) with temperature for the slider flying at the inner track, middle track or the outer track. 52
6.4 Change of pitch angle with the temperature. 53
6.5 Change of roll angle with the temperature. 53
6.6 Shear force due to the Couette flow component in the head disk interface for slider A. (a) the shear force at $T = 25°$C. (b) The difference of the shear force at $T = 25°$C from that at $T = 100°$C 54
6.7 Shear force due to the Couette flow component in the head disk interface for slider B. (a) the shear force at $T = 25°$C. (b) The difference of the shear force at $T = 25°$C from that at $T = 100°$C. Note that the zero value in this figure corresponds to a different color from that in Fig. 6.6. 55

7.1 One molecule moves close to one boundary (a) and two boundaries (b). . . . 60
7.2 Heat conduction predicted by the original model, the new model with the modified mean free path and numerical results from the linearized Boltzmann equation. The non-dimensional heat flux $Q = q/[\rho_0\sqrt{2RT_0}(T_s - T_d)/T_0]$ . . . 61
7.3 Couette flow confined between two boundaries moving relative to each other at a speed of u_0 62
7.4 Poiseuille flow confined between two boundaries and driven by a pressure gradient of $\mathrm{d}p/\mathrm{d}x$ 64

7.5 Pressure in isothermal Poiseuille flow. 67
7.6 Comparison of the shear force on the boundary predicted by the analytical formula Eq. (6.7) and that by the DSMC method. 68
7.7 Heat flux on the boundary of an isothermal Poiseuille flow calculated by the DSMC method. 68
7.8 Heat flux on the boundary of a non-isothermal Poiseuille flow calculated by the DSMC method. 69
7.9 Typical air pressure distribution on the ABS of the slider. The peak is located near the transducer. x_l is the slider's length, p is the air pressure in the HDI, p_0 is the ambient pressure outside the HDI, and x and y are along the length and width directions of the slider respectively. 70
7.10 The loss of the slider's flying height at the read-write transducer. The model 1 refers to the model based on the first order slip theory as represented by Eq. (7.1) and the model 2 refers to Chen *et al.*'s model with the modified mean free path in Eq. (7.4). 70
7.11 Relative difference in minimum flying height predicted by the two models. . 71

8.1 Changes of the mean free path and thermal conductivity of air-helium gas mixtures with the fraction of helium in the mixture. 76
8.2 Change of the viscosity of air-helium gas mixtures with the fraction of helium in the mixture. The results obtained from Eq. (8.2) are compared with experiments excerpted from Ref. [Johns et al. 1982]. The relative error is generally within 5%. 77
8.3 Typical pressure distribution on the TFC slider's ABS. The maximum pressure appears near the transducer. 77
8.4 Relative change of the gap spacing under the transducer with the fraction of helium in the gas mixture, normalized to the value at $\alpha = 0$. The gap spacing at $\alpha = 0$ without power applied to the heater element is 16.1nm, and that with power is 7.2nm. 78
8.5 Change of the maximum pressure with the fraction of helium in the gas mixture. 78
8.6 Change of the maximum temperature rise with the fraction of helium in the gas mixture. 79
8.7 Change of the slider's protrusion at the transducer with the fraction of helium in the gas mixture. 80
8.8 Change of the thermal actuation efficiency with the fraction of helium in the gas mixture. The square points are numerical results and the dotted line is a smooth fit of the data with a fourth order polynomial. 81

List of Tables

8.1 Physical properties of air-helium gas mixtures. 75

Chapter 1

Introduction

1.1 Brief history and structure of hard disk drives

As the last moving part in modern computers, hard disk drives (HDDs) were invented by R. Johnson in 1954 and were introduced by IBM two years later as an alternatives to the then existing magnetic storage devices such as magnetic drums and floppy disks [Stevens 1981; Harker et al. 1981]. The first HDD, weighing over one ton and shown in Fig. 1.1 [Wikipedia 2010], does not bear a lot of similarity with its modern counterparts. It used 50 disks to store information data which were read and written by two transducers. Each transducer was embedded in an externally pressurized head as shown in Fig. 1.2 [Harker et al. 1981]. During the HDDs' operation, compressed air was supplied to the head such that the head was positioned at hundreds of micrometers from the disk. Since this HDD only had one pair of heads, the heads needed to move from one disk to another in order to read/write information data on different disks. The first generation HDDs were so sophisticated that they needed regular maintenance, and IBM licensed them to their customers for $3500 per month, instead of selling them [Wikipedia 2010].

The next two decades saw much improvement and technological innovation, such as lightly loaded self-acting air bearing sliders, lubricated disks and voice coil motors, applied to HDDs, which finally led to the appearance of IBM's Winchester HDD. Despite their large size and small capacity when compared to modern HDDs, the Winchester HDDs had an almost identical inner structure and working principle as the modern HDDs which are sometimes also called the Winchester type HDDs. This then new type of HDDs was so reliable that regular maintenance was no longer needed, and HDDs could be sold to customers at a reasonable price, which paved the way to the popularization of IBM's personal computer (PC). Further improvement in the HDDs' performance appeared in the following several decades, which enabled HDDs to dominate the magnetic recording data storage market.

HDD performance mainly refers to its capacity, speed and reliability. The first one is characterized by the HDD's areal density defined as its capacity on an area of one square inch on the magnetic disk. As HDDs are now approaching the superparamagnetic limit, which limits further miniaturization a magnetic grain can have, the HDDs' current compound growth rate, as shown in Fig. 1.3 [HGST 2010; INSIC 2010], has decreased from 100% during the 1990s to about 40%, which is still larger than that for the number of transistors predicted by Moore's law [Grochowski and Halem 2003]. The HDDs' areal density is expected

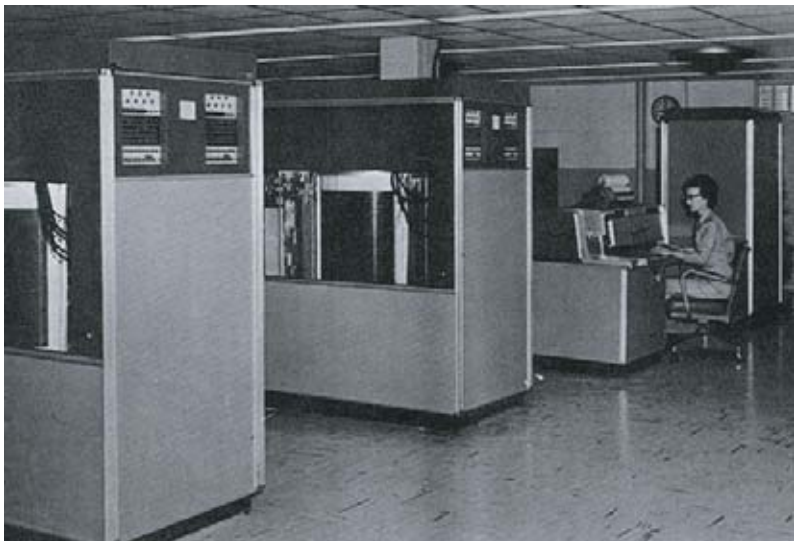

Figure 1.1: The first hard disk drive. [Wikipedia 2010]

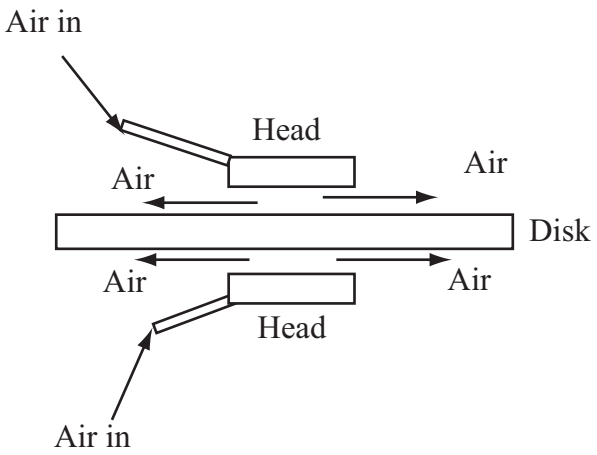

Figure 1.2: Sketch showing the working principle of the first hard disk drive.

to be larger than 10TeraBit/in^2 in the next decade as the emerging techniques such as bit patterned media and heat assisted magnetic recording become mature [Shiroishi et al. 2009; Wood 2009]. A HDD's speed is characterized by its seeking time which has decreased from 10ms in 1990s to the current 3ms, and a HDD's mean time between failure (MTBF) characterizing the HDD's reliability has increased from less than 50,000 hours in 1990s to the current 1,500,000 hours as shown in Fig. 1.4.

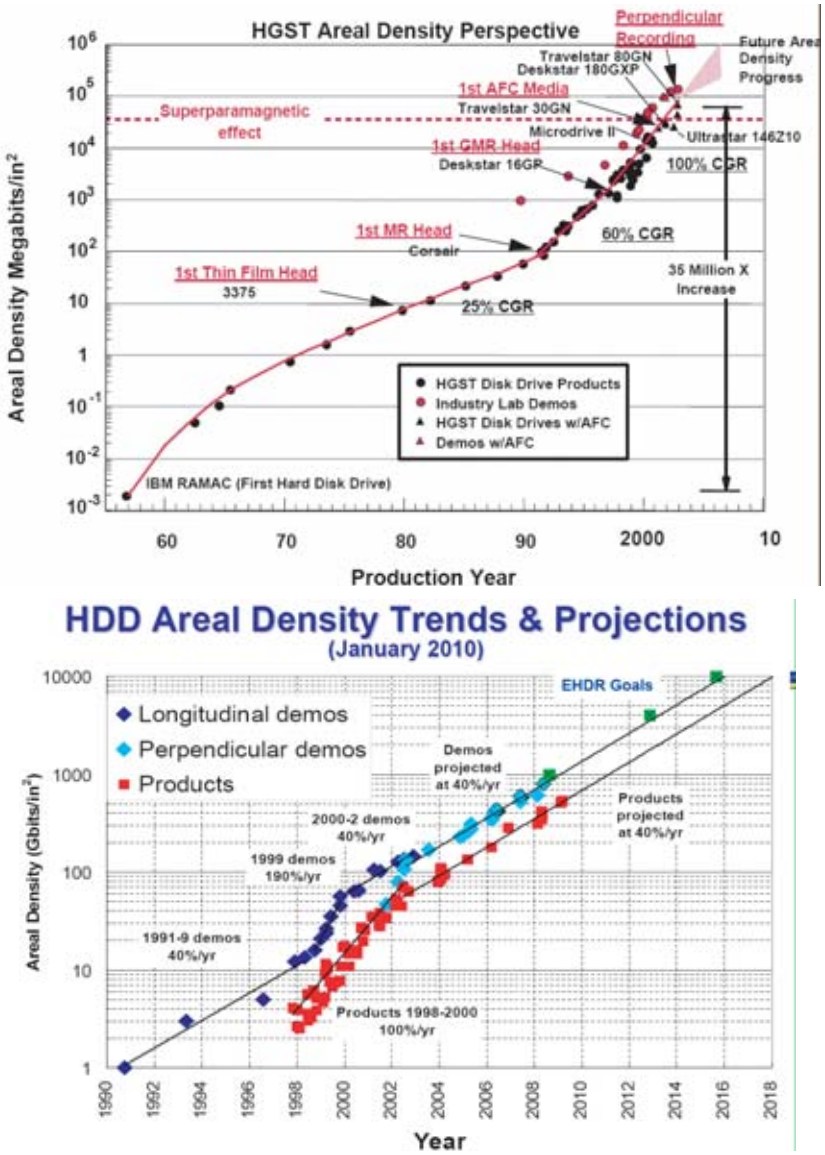

Figure 1.3: Increase of HDDs' areal density since their invention. The major technological innovations that enable the increase are also shown in the figure. [HGST 2010; INSIC 2010]

HDDs can have different form factors which refers to the size of HDDs. In the history of HDDs, several forma factors have appeared and then disappeared. Most recently, the 0.8inch and 1.0inch HDDs with a capacity of tens of gigabytes disappeared due to the competitions from solid state "flash" drives with a comparable capacity. Nowadays, HDDs

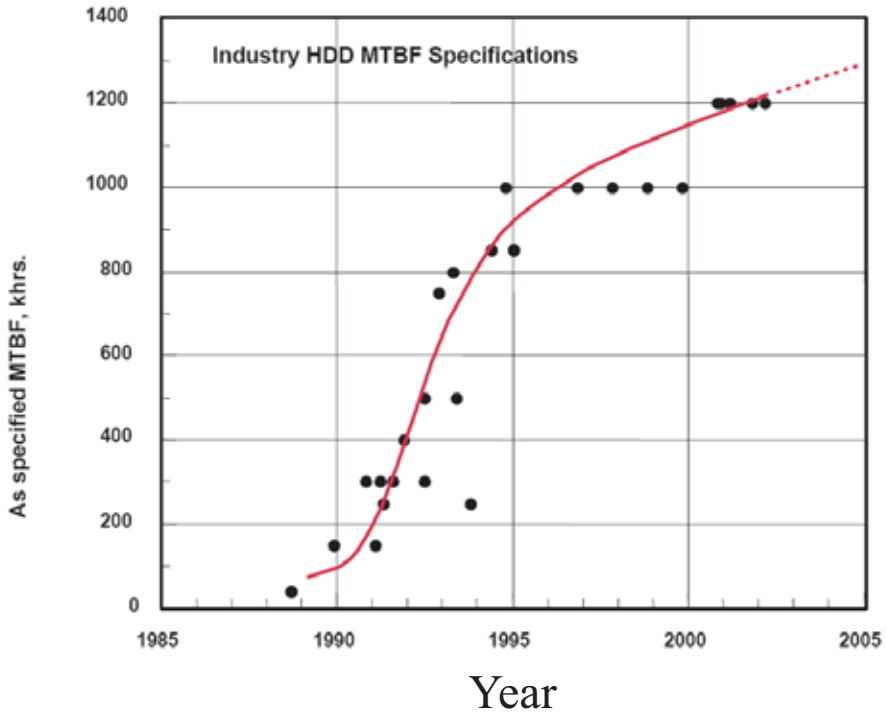

Figure 1.4: Increase of HDDs' mean time between failure (MTBF) in recent years. [HGST 2010]

mainly have three form factors: 3.5inch HDDs for desktop application, 2.5inch HDDs for laptop application, and 1.8inch HDDs for mobile application such as MP3 players and smart phones. Despite their different form factors, all the HDDs have the same structure.

1.2 Structure of a modern hard disk drive

A modern HDD with its upper cover removed is shown in Figure 1.5 PCGuide [2010] and sketched in Fig. 1.6. The HDD usually contains up to 4 magnetic disks to store information. Figure 1.6 shows the typical structure of a magnetic disk. The information data are stored on a 20-50nm-thick magnetic layer deposited onto the substrate. On top of the magnetic layer, an ultra-thin diamond-like carbon (DLC) overcoat of 2-5nm thickness is deposited to protect the magnetic layer from impact, corrosion and wear. The DLC overcoat is covered by a layer of lubricant of thickness less than 2nm to reduce the DLC film's wear and further protect the magnetic layer.

The information data stored on the magnetic disk are read and written by a read-write transducer, made by integrated circuit (IC) technology and embedded in a self-acting slider. The slider is attached to the end of a suspension which itself is connected to a voice coil motor (VCM). When data at different locations need to be manipulated, the VCM drives the suspension so that the slider can be positioned over the designated location. For the HDDs' reliability, the slider needs to fly stably over the disk, i.e., the slider's flying attitude (height, pitch and roll) should change no more than 10 percent when it is positioned over different

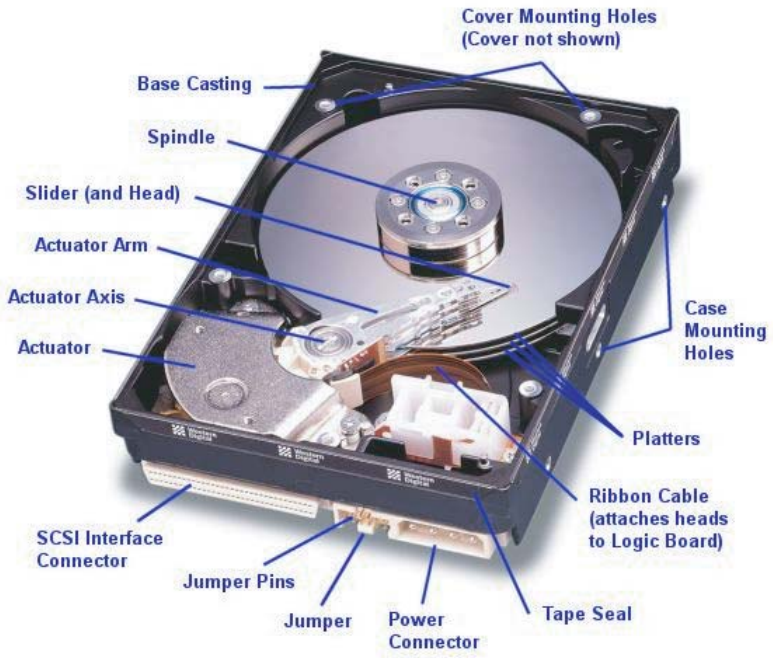

Figure 1.5: A modern HDD with upper cover removed. PCGuide [2010]

locations on the disk. This stable flying attitude is achieved through a careful design of the pattern on the slider's surface facing the disk, known as the air bearing surface (ABS). A typical ABS design is shown in Fig. 1.7, and much more complicated designs are not uncommon in state-of-the-art commercial hard disk drives. During the HDDs' operation, the magnetic disk rotates at a speed up to 15000 revolutions per minute (RPM), producing a linear speed at the slider around 10–30m/s [Liu et al. 2010b]. The rotating disk drags air (due to its viscosity) into the region between the slider and the disk, known as the head-disk interface (HDI), and the air gets compressed and rarefied by the slider's ABS, so that the total air pressure on the ABS balances the load applied by the suspension and the slider is kept away from the disk at a designated distance.

The state-of-the-art sliders, known as thermal flying-height control (TFC) sliders [Meyer et al. 1999; Tang et al. 2007; Kurita and Suzuki 2004], have an embedded heater element near the transducer. The slider spacing can be at a safe distance but during the HDD's reading or writing operations, power is applied to this heater element and, due to the thermo-mechanical coupling, the slider protrudes locally over a very small area near the transducer so that the distance between the transducer and the disk can be further decreased. The heater element is surrounded by thermal insulators, and additional thermal shields are inserted between the heater and the writer, as shown in Fig. 1.6. This complex structure does not lend itself to analytical studies of the slider's deformation induced by the power applied to the heater, and numerical approaches are instead widely used, which lays the foundation for designs of TFC sliders [Liu et al. 2010b].

According to the Wallace magnetic spacing law [Wallace 1951], the strength of a reading signal decreases exponentially with the distance between the magnetic disk and the

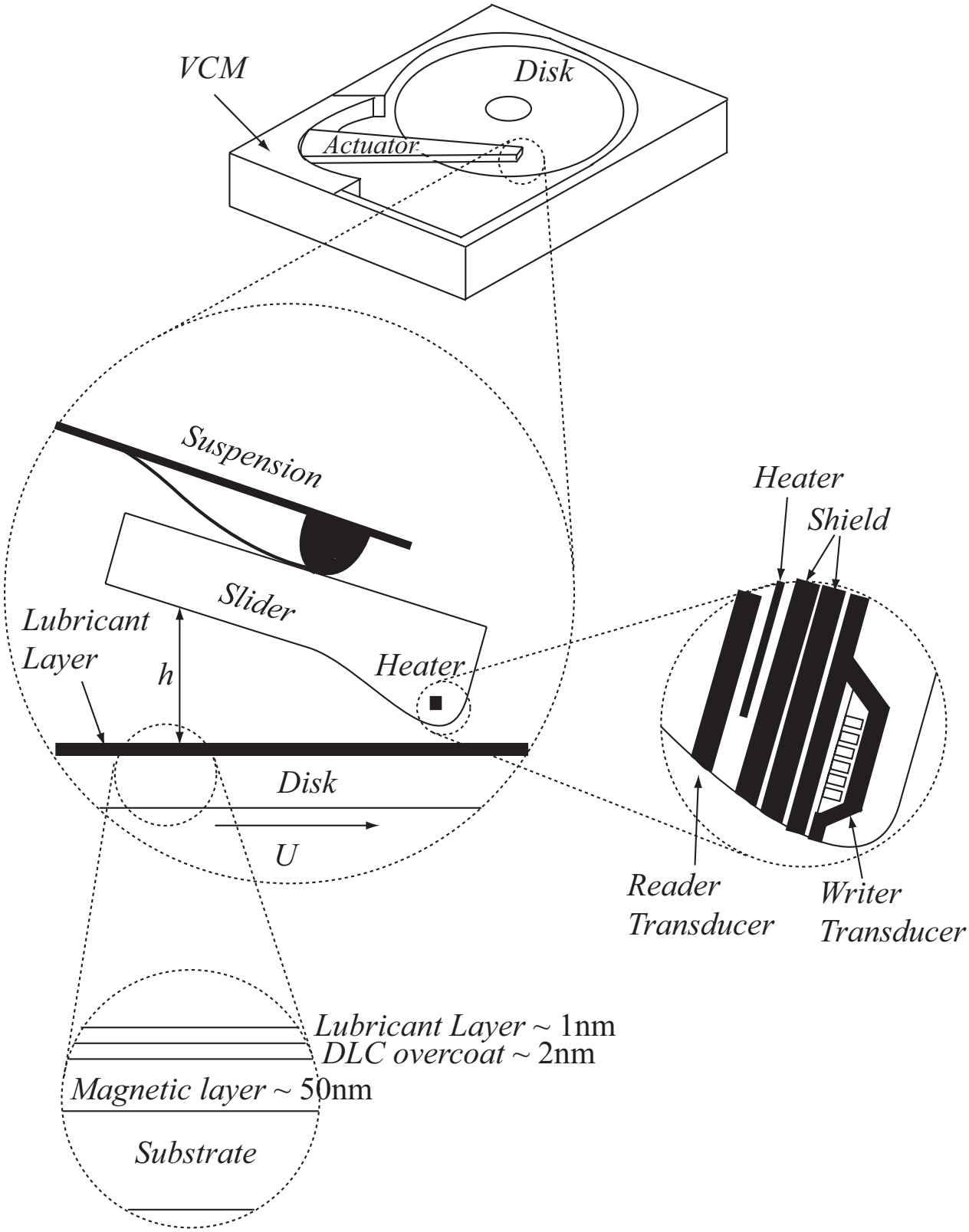

Figure 1.6: Structure of a magnetic disk and a thermal flying height control (TFC) slider in a HDD.

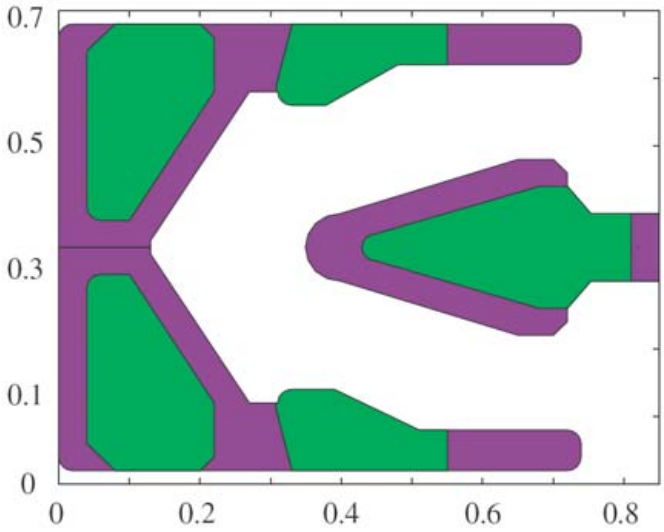

Figure 1.7: A typical air bearing surface (ABS). Different color denotes different etching depth.

transducer. Thus, regardless of the approach to increase the HDDs' capacity, the air gap thickness underneath the transducer keeps decreasing and is now approaching a distance less than 5nm [Grochowski and Halem 2003]. In state-of-the-art HDDs, the air gap thickness in the region between the slider and the disk, the HDI, ranges from several nanometers to several micrometers which are comparable to the mean free path of air, defined as the average distance air molecules can travel between collisions [Bird 1994], and therefore the air's discrete nature needs to be considered.

1.3 Rarefied gas dynamics

Continuum theory for a gas considers the gas as occupying all space that contains it. It neglects the discrete nature of the gas and uses mathematically continuous macroscopic quantities such as density and pressure to describe the gas's behavior through the Navier-Stokes equation [Batchelor 1967]:

$$\begin{aligned} \frac{\partial \rho}{\partial t} + \nabla \cdot (\rho \mathbf{v}) &= 0 \\ \rho \frac{\partial \mathbf{v}}{\partial t} + \mathbf{v} \cdot \nabla \mathbf{v} &= -\nabla p + (\mu_1 + \mu)\nabla(\nabla \cdot \mathbf{v}) + \mu \nabla^2 \mathbf{v} \end{aligned} \tag{1.1}$$

where ρ is gas density, $\mathbf{v}$ is gas velocity, p is gas pressure, μ the dynamic viscosity of the gas, and μ_1 is the bulk viscosity of the gas. The boundary conditions supplementing Eq. (1.1) are the so called no slip boundary conditions which state that the velocity of the gas at a boundary is equal to that of the boundary.

It is generally agreed that continuum theory holds when the Knudsen number, defined as the ratio of the mean free path of the gas, λ, to the characteristic length scale of the gas occupied region, l, is much less than 1 and usually less than 0.01, or Kn=$\lambda/h < 0.01$,

beyond which the gas' discrete nature needs to be considered [Schaaf and Chambré 1961; Kogan 1969; Springer 1971; Bird 1994; Cercignani 2000]. When 0.01 <Kn< 0.1, the gas is called slightly rarefied, and Eq. (1.1) still applies but no-slip boundary conditions break down. Velocity slip then needs to be allowed at the boundary, and the most widely used slip boundary condition states that the difference between the velocity of gas near a boundary and that of the boundary is proportional to the normal gradient of the local gas velocity, or $\mathbf{v} - \mathbf{U} = \beta \nabla \mathbf{v} \cdot \mathbf{n}$ where $\mathbf{U}$ is the velocity of the boundary, $\mathbf{n}$ is the normal direction of the boundary, β is a constant characterizing the slip of gas near the boundary, and all the values are taken at the boundary [Lamb 1945].

When the Knudsen number is even higher, the Navier-Stokes equation breaks down due to the breakdown of the Newtonian constitutive equation, and the gas flow is instead described by the Boltzmann equation, which, for a steady problem, is [Bird 1994]

$$\xi_i \frac{\partial f}{\partial x_i} = J(f, f), \tag{1.2}$$

where f is the velocity distribution function of the gas molecules related to the gas density ρ by $\rho = \iiint f \mathrm{d}\xi_1 \mathrm{d}\xi_2 \mathrm{d}\xi_3$, x_i are Cartesian coordinates, and ξ_i are the molecular velocity components with i ranging over 1, 2, 3 and the summation convention is used. $J(f, f)$ is a complicated integral involving f. When the Knudsen number is much higher which usually needs to be larger than 10, the gas is said to be highly rarefied and collision between gas molecules is rare. Then the right hand side of Eq. (1.2) vanishes and the velocity distribution function f is constant along the molecule's trajectory.

For a general case where the Knudsen number is on the order of 1, we cannot avoid using the full Boltzmann equation. As a differential-integral equation, Eq. (1.2) is very difficult to solve even with numerical methods. Several models have been proposed to phenomenologically model the collision between any two molecules such that no integral appears on the right hand side of Eq. (1.2). The most widely accepted model is the one proposed by Bhatnagar, Gross and Krook [Bhatnagar et al. 1954], which uses a relaxation model to replace the right hand side of Eq. (1.2), with which the Boltzmann equation becomes the so called BGK-Boltzmann equation

$$\xi_i \frac{\partial f}{\partial x_i} = \nu (f_e - f) \tag{1.3}$$

with

$$f_e = \frac{\rho}{(2\pi RT)^{3/2}} \exp\left(-\frac{(\xi_i - u_i)(\xi_i - u_i)}{2RT} \right),$$

where ν is a parameter related to the collision frequency of molecules, f_e is the local Maxwellian distribution function determined by local density ρ, local temperature T, and local gas velocity u_i, all of which are determined by the local velocity distribution function f, and R is the specific gas constant. Thus despite its simple form, the BGK-Boltzmann equation is a nonlinear equation since f_e implicitly depends on f through the dependence of ρ, u_i and T on f.

For the gas flow in the HDI, the flow velocity is much less than the average thermal velocity of the gas molecules which is on the order of the speed of sound in the gas, and, thus, all of the quantities can be expanded as Taylor series of the ratio of the characteristic gas speed to the average thermal speed of the gas. The BGK-Boltzmann equation can then

be linearized by retaining only linear terms in the series, and the linearized BGK-Boltzmann equation for a steady flow of an isothermal gas is:

$$\xi_i \frac{\partial \phi}{\partial x_i} = \nu \left(-\phi - 1 + \frac{\rho}{\rho_0} + \frac{\xi_i v_i}{RT_0} \right). \tag{1.4}$$

where $\phi = f/f_0 - 1$, f_0 is the Maxwellian distribution function at the ambient state

$$f_0 = \frac{\rho_0}{(2\pi RT_0)^{3/2}} \exp\left(-\frac{\xi_i \xi_i}{2RT_0} \right),$$

ρ_0, T_0 are the ambient density and the ambient temperature.

The corresponding boundary condition accompanying Eq. (1.4), is [Sone 2006]

$$\phi(x_i, \xi_i) = (1-\alpha)\phi(x_i, \xi_i - 2\xi_j n_j n_i) - \alpha \frac{2\sqrt{\pi}}{(2RT_0)^2} \int_{\xi_k n_k < 0} \xi_j n_j \phi \exp(-\frac{\xi_k \xi_k}{2RT_0}) d\boldsymbol{\xi}, \tag{1.5}$$

where α is the accommodation coefficient and n_i is the outward unit normal to the boundary.

Equation (1.4) together with the boundary condition Eq. (1.5) forms the basis for studying the gas flow in the HDI. One example is the derived generalized Reynolds equation used to characterize the slider's flying performance.

1.4 Motivation and organization of the dissertation

With the introduction of solid state drives (SSDs), HDDs have lost their dominance in the small-capacity storage market such as MP3 players and smart cell phones, but HDDs hold firmly the massive storage market, such as servers and workstations, for which Terabytes of storage capacity is quite common nowadays. To compete with SSDs in the future, the HDDs need to improve their performance [Burr et al. 2008; Freitas and Wilcke 2008; Kryder and Kim 2009]. This dissertation applies rarefied gas dynamics to investigate several issues related to HDDs' performance: particle contamination, temperature rise inside HDDs and TFC sliders. It is organized as follows. Chapter 2 reviews the numerical approach to study particle contamination on a slider and investigates how the presence of the slider and disk affects the particle contamination on the slider. Chapter 3 derives analytical formulae for lift forces on a particle moving in a highly rarefied gas. Chapter 4 derives analytical formulae for lift forces on a particle moving in a slightly rarefied gas and uses this formula together with those derived in Chapter 3 to discuss the effect of lift force on particle contamination on a slider. Chapter 5 investigates particle contamination on a thermal flying-height control (TFC) slider and discusses the applicability of the current particle contamination model to a TFC slider. Chapter 6 investigates the temperature effect on a slider's flying performance. Chapter 7 reviews the numerical approach to investigate the flying performance of a TFC slider and studies the heat flux on the TFC slider which serves as a boundary condition in the numerical approach. Chapter 8 investigates the flying performance of a TFC slider in air-helium gas mixtures, and, finally, a summary and conclusion is given in Chapter 9.

Chapter 2

Boundary effect on slider particle contamination

2.1 Introduction

Hard disk drives (HDDs) are not free of particles, which are generated due to different causes such as manufacturing debris, the slider's loading/unloading process, and its occasional contact onto the disk. Particles entering the HDI may stick to the region on the slider under the read/read transducer and affect the transducer's effectiveness. Other particles might accumulate on the slider and increase the possibility of the slider's contact with the disk, which could further cause the loss of data stored on the disk. Thus particle contamination on the slider can be critical to the HDDs' reliability especially for sliders with an ultra-low flying height which is required for achieving an areal density of 10Terabit/in^2 in the next decades [Zhang and Bogy 1997a,b; Shen et al. 2004; Liu and Bogy 2008]. Specific designs used to reduce contamination can be found on some state-of-the-art commercial sliders, but the physical mechanism of contamination is still unclear. The study of the contamination mechanism will help to better understand and better design specific features on a slider to reduce the contamination.

Due to the low volume fraction of particles in the HDI, which is less than 1%, the influence of the particles on the flow field is localized, i.e. their presence does not affect the flow field around other particles, and, thus, the presence of other particles can be neglected when calculating the forces on any one particle. Likewise, the collision between particles is rare, and, therefore, the trajectory of each particle can be calculated separately. The governing equation for a particle moving in a non-uniform flow field is quite complex [Maxey and Riley 1983; Maxey 1993], but it can be simplified for the current problem. It turns out that only the drag and lift forces as well as other microscale forces, if present, are important. Despite the particle's small size, the effect of Brownian motion is negligible due to the large Peclet number [Shen and Bogy 2003], which characterizes the importance of Brownian motion compared to non-Brownian motion. The larger the Peclet number the less important the Brownian motion.

The gap spacing between the slider and the disk in the HDI varies from several nanometers to a few micrometers with the largest spacing appearing in the recess region, as shown in Fig. 2.1. Since the gap spacing at the entrance is about 300 nanometers, the sizes of the

particles entering the HDI range from several nanometers to around 300 nanometers. Zhang and Bogy [Zhang and Bogy 1997a] found that the lift force is only important for particles of radius larger than 100nm and for particles crossing the transition region between the leading pad and the recess region, and, accordingly, these particles, under the influence of the lift force, move upward with possibility to contact the slider. But for other particles, the lift force is negligible and these particles' motion follows the local streamline. Shen, Suk and Bogy [Shen et al. 2004] found that particles entering the recess region experience an additional drag force due to the local vertical (perpendicular to the disk) air flow velocity. By incorporating this force into Zhang and Bogy's model, Shen, Suk and Bogy showed that their numerical results compare better with experiments [Shen et al. 2004].

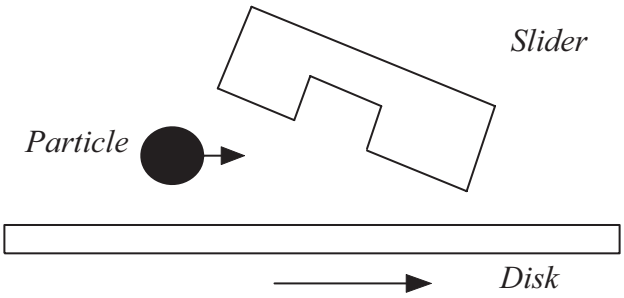

Figure 2.1: A sketch of the head-disk interface showing the recess region.

For particles moving in the HDI, their motion is affected by the presence of the slider and the disk. This effect, however, has not been fully considered and will be further studied here. This chapter is organized as follows. Section 2.2 reviews the numerical approach to simulate particle contamination and the analytical formulae to calculate forces on a particle moving in the HDI. Section 2.3 shows how to include boundary effects in the calculation of drag forces. Section 2.4 proposes a criterion to determine when particles contaminate the slider. Section 2.5 discusses the accuracy of the integration scheme used in previous studies. Section 2.6 presents and discuses the numerical results, and a summary and conclusion is given in Sec. 2.7.

2.2 Numerical study of a particle's motion in the HDI

After neglecting all unimportant contributions, the governing equation for a particle moving in the HDI is simply:

$$m\frac{\mathrm{d}^2\mathbf{r}}{\mathrm{d}t^2} = \mathbf{F}_{lift} + \mathbf{F}_{drag} \tag{2.1}$$

where m is the particle's mass, $\mathbf{r}$ is the particle's location, t is time, and the two forces considered are the drag force $\mathbf{F}_{lift}$ and the lift force $\mathbf{F}_{drag}$.

The drag force is due to the difference in the velocity of the particle and the local air flow, and it is given by

$$\mathbf{F}_{drag} = \frac{\pi}{2} C_d C_w \rho_g R^2 \|\mathbf{u}_g - \mathbf{u}_p\|(\mathbf{u}_g - \mathbf{u}_p) \tag{2.2}$$

where C_d is the drag coefficient for a particle moving in a rarified gas field extending to infinity [Liu et al. 1965] accounting for the gas rarefaction effect, C_w is the correction factor accounting for the effect of the presence of the slider and/or the disk, R is the radius of the assumed spherical particle, ρ_g is the air density, $\mathbf{u}_g$ is the air velocity and $\mathbf{u}_p$ is the particle velocity. The previous correction factor C_w used by Zhang and Bogy [Zhang and Bogy 1997b] was valid only for a sphere moving at some specific location between a slider and a disk, and one goal of this chapter is to get a more general correction factor C_w that is uniformly valid.

The lift force contains two contributions: Saffman force and Magnus force. The Magnus force is due to the particle's rotation [Rubinow and Keller 1961], and has been shown to be negligible for particles moving in the HDI [Zhang and Bogy 1997a]. The Saffman force is due to the local non-uniformity of the flow field and, given our particles' small size, it can be calculated by [Saffmann 1965; Cox and Hsu 1977]:

$$F_{saffman} = \frac{9}{\pi} J \mu R^2 \triangle U \sqrt{\frac{|G|\rho_g}{\mu}} \tag{2.3}$$

where μ is the air viscosity, $\triangle U$ is the magnitude of the particle velocity relative to the air flow, G is the velocity gradient of the air flow, and J is expressed as

$$J = \frac{\pi^2}{16}\left(\frac{\triangle U}{\sqrt{|G|\mu/\rho_g}} + \frac{11}{6}\sqrt{\frac{|G|\rho_g}{\mu}} l_w\right)$$

where l_w is the distance from the particle's center to the wall. We note that Eq. (2.3) is derived from the continuum theory and might not hold for our case where the gas is rarefied. In the next chapter, we will investigate how to calculate this force in a rarefied gas field. Results in later chapters show that replacing Eq. (2.3) by the correct formula only slightly affects the final results. Thus, in this chapter, we will use Eq. (2.3) as done in all the previous studies.

2.3 Boundary effect on a particle's motion in the HDI

In the HDI, the slider and the disk are almost parallel to each other, and, given our particles' small size, we model the HDI as two parallel plates. Even without gas rarefaction, the motion of a particle between two parallel plates is not analytically solvable. Here we adopt an approximate approach of using continuum theory to get the correction factor C_w, and we assume that this C_w applies to our problem [Liu and Bogy 2009a].

Given our particle's small size, the inertial effect is negligible, and a particle's motion in the HDI can be seen as a linear combination of two motions: the particle's motion parallel to the two plates and that perpendicular to the plates [Happel and Brenner 1983; Kim and Karrila 2005]. To account for the effect of the presence of the two boundaries, let us first consider the case where only one plate is present, as shown in Fig. 2.2. Although analytical results exist for this simple case, they are too complex to implement in our code. Instead, we propose the following formula to approximate the exact results:

$$\mathbf{F}^I = \mathbf{F}^I_{far}\left[1 - \exp\left(-\beta_1 \frac{\delta}{R}\right)\right] + \mathbf{F}^I_{close} \exp\left(-\beta_2 \frac{\delta}{R}\right) \tag{2.4}$$

where $\mathbf{F}^I_{far}$ is the drag force on a particle moving far from a wall, $\mathbf{F}^I_{close}$ is that on a particle moving close to a wall, β_1 and β_2 are parameters to be determined by nonlinear regression to fit this expression with exact results, and δ is the gap between the particle and the wall, as shown in Fig. 2.2.

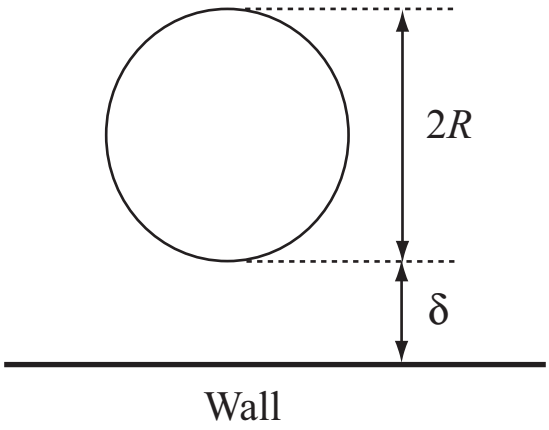

Figure 2.2: A particle moving near a boundary, where R is the particle radius and δ is the gap between the particle and the boundary.

More specifically, for a particle moving at a speed U perpendicular to a boundary, the two asymptotic results for the particle moving close and far from the wall are documented in Ref. [Glodman et al. 1967] and the exact result, involving summation over infinite terms, has already been obtained by Brenner [Happel and Brenner 1983]. Based on these, we can determine β_1, β_2 to be 0.1 and 0.008, respectively, and the drag force is

$$\frac{F^I}{6\pi\mu UR} = \left[1 - \frac{9}{8}\frac{R}{z} + \frac{1}{2}\left(\frac{R}{z}\right)^3\right]^{-1}\left[1 - \exp\left(-0.1\frac{\delta}{R}\right)\right] + \left[\frac{R}{R-z} - \frac{1}{5}\ln\left(\frac{R}{R-z}\right) + 0.9712\right]\exp\left(-0.08\frac{\delta}{R}\right) \tag{2.5}$$

Similarly, for a particle moving at a speed U parallel to the boundary, we can use the two asymptotic results [Glodman et al. 1967] and the exact result, which involves solution of a system of equations, to determine β_1 and β_2 to be 2.93 and 2.68. The drag force for this case is

$$\frac{F^I}{6\pi\mu UR} = \left[1 - \frac{9}{16}\frac{R}{z} + \frac{1}{8}\left(\frac{R}{z}\right)^3 - \frac{45}{256}\left(\frac{R}{z}\right)^4 - \frac{1}{16}\left(\frac{R}{z}\right)^5\right]^{-1}\left[1 - \exp\left(-2.93\frac{\delta}{R}\right)\right] + \left[0.9588 - \frac{8}{15}\ln\left(\frac{z}{R} - 1\right) + 0.9712\right]\exp\left(-2.68\frac{\delta}{R}\right) \tag{2.6}$$

Figure 2.3 compares Eq. (2.5) with Brenner's exact results [Happel and Brenner 1983] for a particle moving perpendicular to a wall. As shown in the figure, the maximum relative error is around 2%. Similar accuracy holds for Eq. (2.6).

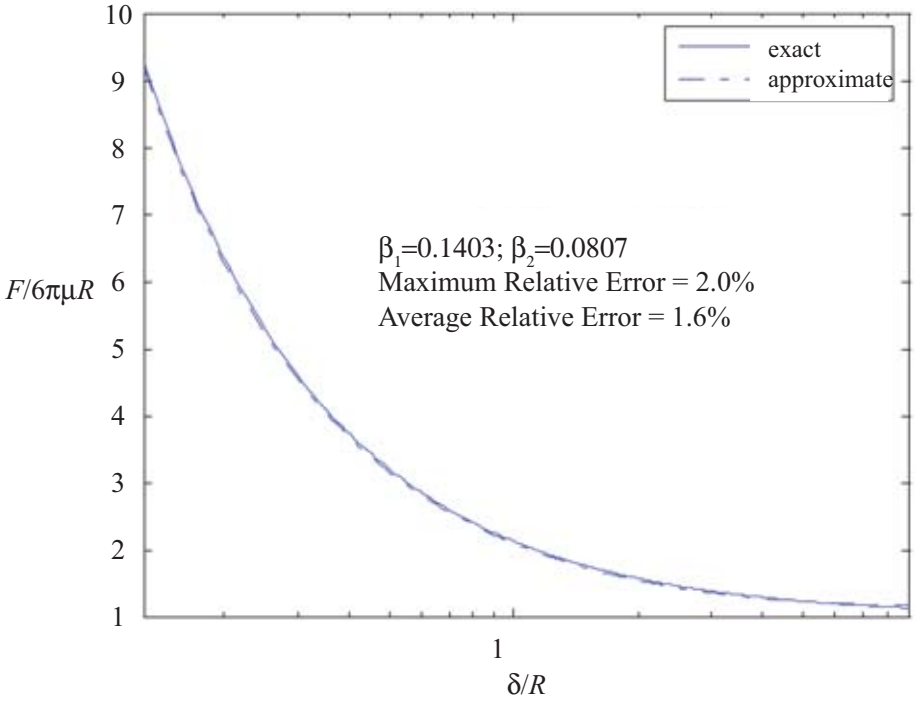

Figure 2.3: Comparison of Eq. (2.5) with the exact results.

Next, we determine the effect of two walls–the slider and the disk–on a particle moving between them. Although this problem can be solved via the boundary collocation or boundary integral equation method, the result is not analytical and can not be efficiently incorporated into Eq. (2.2) as a correction factor. However, by using the method of reflection, an approximate formula was derived based on Eq. (2.4) [Lobry and Ostrowsky 1996; Liu et al. 2000]:

$$\mathbf{F}^{II}(z) \approx \mathbf{F}_0 + \sum_{n=0}^{\infty}[\mathbf{F}^{I}(z+nh) - \mathbf{F}_0] + \sum_{n=0}^{\infty}[\mathbf{F}^{I}(nh-z) - \mathbf{F}_0] - 2\sum_{n=1}^{\infty}[\mathbf{F}^{I}(nh) - \mathbf{F}_0] \quad (2.7)$$

where $\mathbf{F}^{II}$ is the drag force on a particle moving between two walls, $\mathbf{F}^{I}$ is the drag force derived from Eq. (2.4), $\mathbf{F}_0 = 6\pi\mu\mathbf{U}R$ is the Stokes drag force, $\mathbf{U}$ is the particle's velocity relative to the flow, h is the distance between the two walls, and z is the distance from the center of the particle to the lower wall, as shown in Fig. 2.4. The C_w's for different motions of the particle are now determined by $\mathbf{F}^{II}/\mathbf{F}_0$

Figure 2.5 shows a comparison between Eq. (2.7) and the numerical results obtained from the boundary collocation method [Ganatos et al. 1980], which solves an equivalent integral form of the Stokes equation, for a particle moving perpendicular to two parallel walls. The two results overlap and can not be distinguished from each other. Equation (2.7) involves a summation over an infinite number of terms and still can not be efficiently incorporated in Eq. (2.2). As shown in the next section, when a particle moves very close to a wall, a contamination criterion will be invoked. Thus, we only need to calculate here the trajectory of particles that are not close to the wall. For these particles, the contributions from the

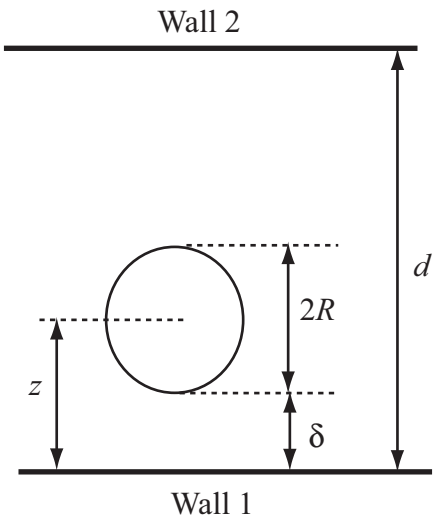

Figure 2.4: A particle moving between two boundaries, where d the distance between the two walls.

higher order terms in the summation are negligible. Therefore, we only need to consider the first few terms in Eq. (2.7) in the following calculation.

As shown in Fig. 2.5, the drag force, predicted by Eq. (2.5) becomes unbounded when a particle moves very close to a wall. But the Saffman force is finite. Therefore, to make contamination possible, some other forces need to be considered when particles approach a boundary.

2.4 Contamination criterion

Intermolecular forces exist between any two bodies, and the intermolecular force between a spherical particle and a wall is

$$F_{IM} = \frac{A_H}{6}\left[\frac{R}{\delta^2} + \frac{R}{(\delta+2R)^2} + \frac{1}{\delta} - \frac{1}{\delta+2R}\right] \tag{2.8}$$

where A_H is the Hamaker constant, which can be determined via Lifshitz theory and is always around $10^{-19} - 10^{-21}$J [Israelachvili 1992].

When a particle moves toward a boundary and is far enough from the boundary, the intermolecular force is negligible when compared to other forces, and the particle's velocity decreases due to the drag force. As the particle approaches the boundary, the intermolecular force becomes more and more important. When the gap between the particle and the boundary, δ, is much smaller than the particle's radiu R, the intermolecular force is asymptotically

$$F_{IM} \sim \frac{A_H R}{6\delta^2} \tag{2.9}$$

while the drag force perpendicular to the boundary, as derived from Eq. (2.5), is

$$F_{drag} \sim \frac{2F_0 R^2}{\delta^2} \tag{2.10}$$

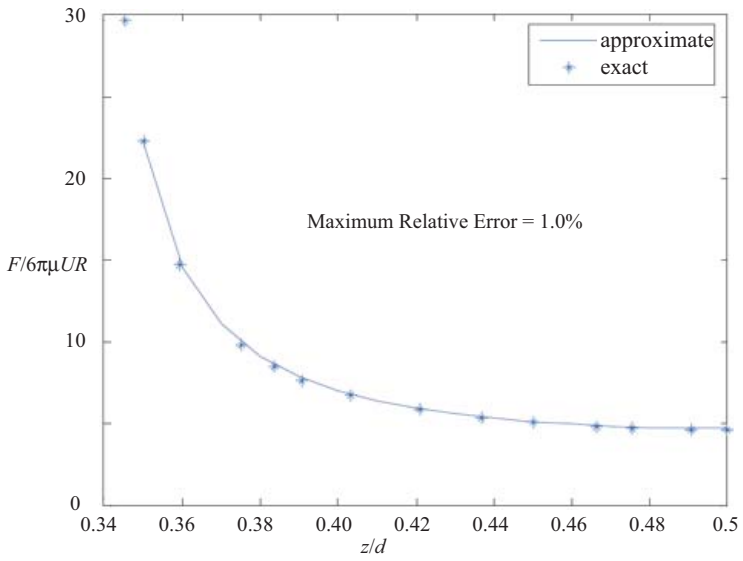

Figure 2.5: Comparison of Eq. (2.7) with numerical results obtained by boundary collocation method for a particle moving at a relative speed U perpendicular to two parallel walls.

where $F_0 = 6\pi\mu UR$ is the Stokes drag force on a spherical particle in a free stream. Both the drag and intermolecular force change inversely proportional to δ^2 and will finally balance each other when the particle's velocity perpendicular to the boundary reduces to $A_H/(48\pi\mu R^2)$. Then the particle will move at this velocity and finally contact the boundary. Thus, our contamination criterion is: for a particle moving towards a boundary, when the particle's relative velocity perpendicular to the boundary reduces to $A_H/(48\pi\mu R^2)$, the particle will finally contact the boundary. Here the relative velocity refers to the particle's velocity relative to the flow.

We note that a particle's trajectory can also be calculated through Eq. (2.1) incorporating the intermolecular force. However, near the boundary, the drag force and the intermolecular force both increases to large values, and the numerical simulation would involve subtraction of two large quantities, which generally introduces large errors. Using the contamination criterion avoids this potential source of errors.

2.5 Integration scheme

To integrate Eq. (2.1), a fourth order Runge-Kutta method was used in previous studies [Zhang and Bogy 1997a]. In this method, a very small time step is required for arriving at convergent results. When the time step is too small, errors accumulate during the integration, leading to inaccurate results. Here, we use a fourth order Runge-Kutta method with automatic step size control to check the accuracy of previous studies with different fixed time step sizes. As shown in Fig. 2.6, a dimensionless time step of 10^{-4} is sufficient for convergence, and this time step will be used in the following calculation of particle contamination profiles.

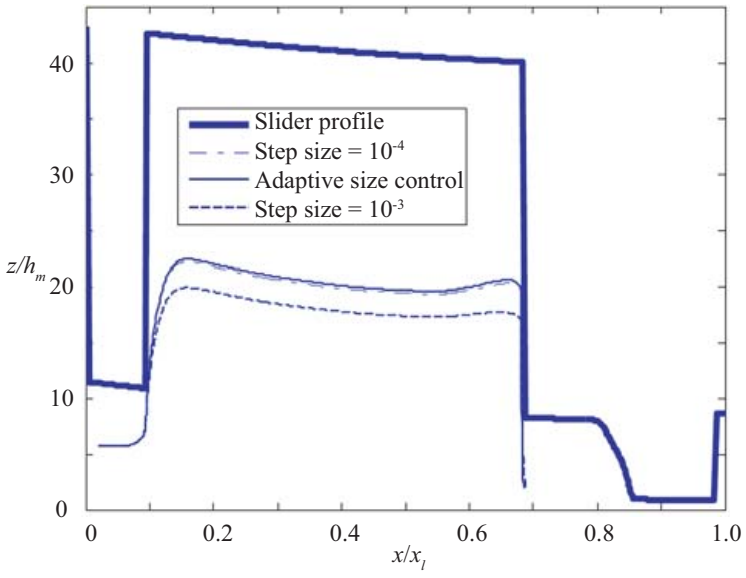

Figure 2.6: Accuracy of using different time steps to calculate a particle's trajectory.

2.6 Numerical results and discussion

Calculation of forces on a particle, involved in integrating the governing equation Eq. (2.1), requires information of the gas flow field in the HDI, which is accomplished here through the use of CML Quick 4, an in-house program to solve the generalized Reynolds equation using the finite volume method [Lu 1997].

Figure 2.7 shows a particle's trajectories for two cases: including the boundary effects and excluding the boundary effects. In both cases, the particle initially experiences the Saffman force and moves upward. When the boundary effect is excluded, the particle crosses the transition region and moves into the recess region. Near the trailing edge, it experiences a downward air flow field and moves downward, leading to its finally contacting the disk. In contrast, when the boundary effect is included, due to the increasing drag force induced by the wall, the particle can not cross the transition region and instead contacts the leading pad.

Figure 2.8 compares particle contamination profiles for the two cases mentioned above: one with boundary effects included, and the other without. The two profiles are only slightly different at some specific locations on the ABS, and more particles contaminate the slider when the boundary effect is considered. This can be understood as follows. When particles move far from the boundary, the correction factor accounting for the boundary effect used in the previous studies and that used in the current one are close to each other, and the particle's trajectories calculated by the two approaches are also similar. When particles move close to the boundary, the previous studies give a finite correction factor for the boundary effect, which, in essence, seems to have the same effects as the use of an unbounded correction with the contamination criterion. Only in some special cases as shown in Fig. 2.7, the particles' trajectories calculated through the two approaches diverge from each other.

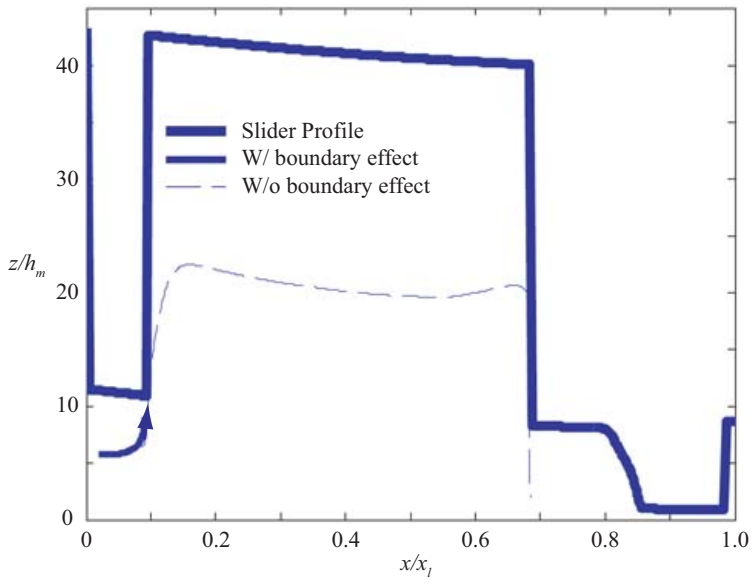

Figure 2.7: A particle's trajectories for two cases: including the boundary effect and excluding the boundary effect.

2.7 Summary and conclusion

This chapter investigates the boundary effect, which is induced by the presence of the slider and the disk, on a particle's motion in the HDI. An approximation is used to account for the boundary effect, and a contamination criterion is proposed to determine when particles contaminate the slider. It is shown that the incorrect correction factor used in previous studies to account for the boundary effect seems to have the same effect as the use of the improved correction factor together with the contamination criterion, and the contamination profile calculated through the new method is only slightly different from that through the previous approach.

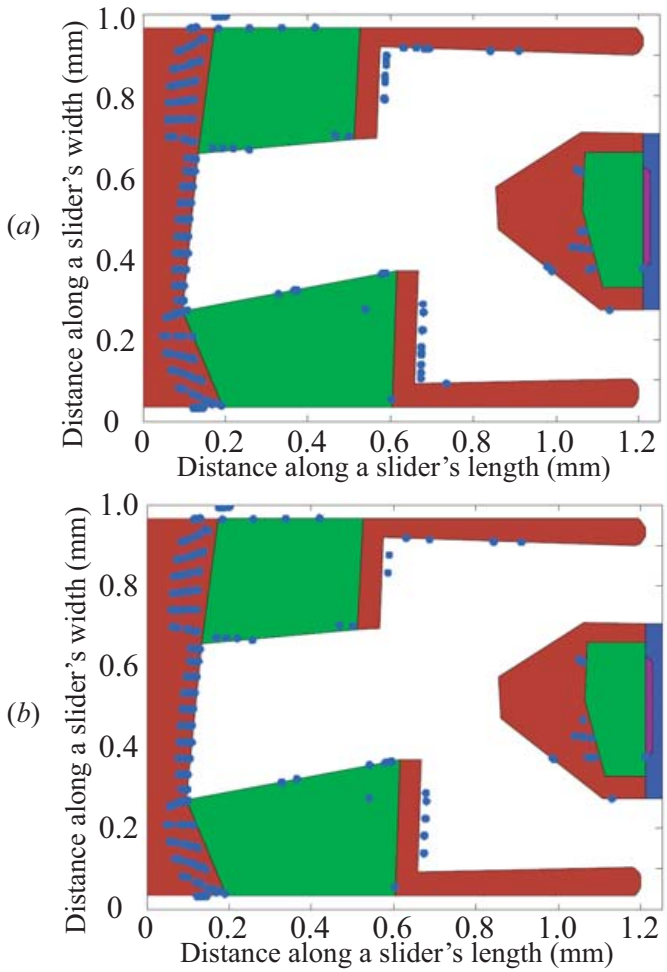

Figure 2.8: Comparison of the present contamination profile (a) and that obtained previously with a limited correction factor for the boundary effect.

Chapter 3

Lift force on a rotating particle in a shear flow of a highly rarefied gas

3.1 Introduction

When a spherical particle moves in a shear flow of a rarefied gas, there are three relevant length scales: the radius of the particle R_0, the mean free path of the gas λ, and a length characterizing the shear strength G of the incoming flow $l_G = U_{f0}/G$ where U_{f0} is the speed of the flow relative to the center of the sphere, which moves at a reference speed. Based on these three lengths, two Knudsen numbers can be defined: $\mathrm{Kn}_p = \lambda/R$ and $\mathrm{Kn}_G = \lambda/l_G$ [Liu et al. 2009a]. When the radius of the sphere is much smaller then the mean free path of the gas molecules, i.e., $\mathrm{Kn}_p \gg 1$, the flow, seen by the particle, is highly rarefied. By "weak shear flow" we mean that the shear strength G is so small that the other Knudsen number Kn_G is much smaller than 1. One application of this kind of problem is the motion of small particles in the gap between the slider and the disk in a hard disk drive. These particles may contact the slider and accumulate there, which increases the possibility of slider-induced damage of the disk and a resulting data loss. The flow in the gap, which is called the head-disk interface (HDI), is set up by the disk moving at a speed of $10 - 30$m/s and is mainly a shear flow. For a large portion of the HDI, the gap spacing is around 1μm [Zhang and Bogy 1997a]. Given that the mean free path of air is 65nm, the Knudsen number Kn_G in those regions is on the order of 0.1. The particles are generated from different means and their sizes range from a few nanometers to hundreds of nanometers. For many slider designs, the gap spacing at the entrance of the HDI is less than 300nm, so only those particles with radius less than this value can enter the HDI. For smaller particles with size around 10nm, which are of concern here, the Knudsen number $\mathrm{Kn}_p \gg 1$.

The motion of a single particle in a fluid is usually calculated using Newton's second law [Zhang and Bogy 1997a; Guha 2008], and the essential part of this calculation is to obtain the forces on the particle. A widely known and documented result is the drag force on a sphere moving without rotation in a highly rarefied gas [Epstein 1924; Schaaf and Chambré 1961; Cercignani et al. 1968; Bird 1994; Li and Wang 2003a,b; Loth 2008]. The first step in the investigate of the general motion of particles is to consider the effect of the particle's rotation. Wang [Wang 1972] studied the forces on a particle rotating around an axis perpendicular to the direction of the incoming *uniform* flow of a highly rarefied gas, and

showed that the particle's rotation induces a lift force along the direction perpendicular to both the incoming flow and the axis of rotation. This lift force was found to be in the opposite direction from its counterpart in a continuum flow. This result was recently rediscovered by Borg, Söderholm and Essén [Borg et al. 2003; Dubinsky and Elperin 2004]. Ivanov and Yanshin [Ivanov and Yanshin 1980] extended Wang's work to a symmetrical body, which includes a sphere as a special case. Unaware of Wang's and Ivanov and Yanshin's work, Weidmann and Herczynski [Weidman and Herczynski 2004] used a particle dynamics model and studied the inverse Magnus force on an arbitrary body rotating in a uniform flow of a highly rarefied gas. Further studies considered nonuniformities of the incoming flow, among which a linear shear flow is the simplest. The linear shear flow is also a good approximation to a flow with its characteristic length scale much larger than the size of the particle, which underlies Saffman's explanation of the drift of small spheres in Poiseuille flow based on his result for the lift force on a sphere in a linear shear flow of continuum fluid [Saffmann 1965]. Kröger and Hütter [Kröger and Hütter 2006] studied the forces on a sphere in a linear shear flow of a highly rarefied gas and qualitatively showed that an additional force is induced by the shear. They showed that the lift force in this case is not zero and is in the opposite direction of the Saffman force, but they did not give an explicit formula for the lift force.

The last chapter is devoted to improving the calculation of the drag force by considering the boundary effect. This and the next chapter will discuss improvement on the calculation of the lift force, or more specifically, the Saffman force, by considering the gas rarefaction effect. In this chapter, we model the particle as a sphere and consider a more general case than a fixed particle lying in a linear shear flow. The main goal here is to get force formulae on a rotating particle in a shear flow of a highly rarefied gas. These formulae will enable us to calculate the particle's trajectory in the HDI. The chapter is organized as follows. In Sec. 3.2, the problem is formulated and all of the assumptions are stated. In Sec. 3.3, the force on a unit area at some location on the surface of a spherical particle is calculated, which is then used to get the total force on a particle with its axis of rotation being the same of the gradient of the flow in Sec. 3.4. The latter results are extended to the general case where the axis of rotation is allowed to be different from the gradient of the flow in Sec. 3.5. A summary and conclusion is given in Sec. 3.6.

3.2 Statement of the problem

Although the particles of interest may be of different shapes, we model them here as spheres. As discussed in the introduction section, the Knudsen number based on the gap spacing in the recess region is much smaller than one, whereas the Knudsen number based on particle size is much greater than one. Thus, when a particle is considered, the gas is highly rarefied, or is a free molecular gas. Then the interaction between the incoming molecules and those reflected by a sphere is neglected. Thus we can get the velocity distribution function of the molecules neglecting the presence of the sphere. For a shear flow in the recess region where the Kundsen number based on the gap spacing is much smaller than one, the above velocity distribution function can be obtained from the Chapman-Enskog theory [Bird 1994]:

$$f = \left[1 - B(C_i' C_j' - \frac{1}{3} C'^2 \delta_{ij}) \frac{\partial C_{0i}}{\partial x_j}\right] f_0 \tag{3.1}$$

where f_0 is the equilibrium Maxwellian distribution function, C is the total molecular velocity, C_0 is the mass average velocity, C' is the thermal velocity and B is a function of C' and the temperature T.

In the following analysis, two coordinate systems–one global and one local–are used and are shown in Fig. 3.1. In the global coordinate system $\{XYZ\}$, the axis X points in the flow direction, the axis Y points to the gradient direction of the shear flow, the axis Z is perpendicular to both the flow direction and the gradient direction of the shear flow, and the flow velocity is $U_f = U_{f0} + GY$. In the local coordinate system $\{xyz\}$ fixed to the sphere and located at (R_0, θ, ϕ), x is along the direction tangential to the parallel while y points to the center of the sphere. In the special case, the axis of rotation is the same as the gradient, but in the general one, the two can be different.

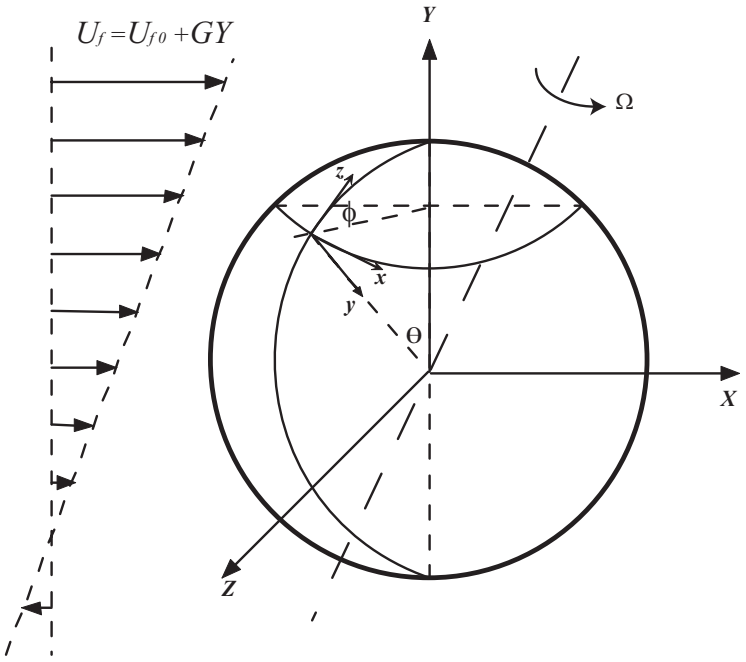

Figure 3.1: The two coordinate systems set up for a spherical particle rotating at angular velocity Ω in a linear shear flow of a highly rarefied gas with the gradient of the shear being G. Note the axis of rotation is not necessarily parallel to the gradient direction

Since the gradient of the flow field is along the Y direction, the general Chapman-Enskog distribution, Eq. (3.1), in the present case, becomes

$$f = f_0 \left(1 + DU'V'\right) \tag{3.2}$$

where $f_0 = \left(\frac{\beta}{\sqrt{\pi}}\right)^3 \exp\left\{-\beta^2[U'^2 + V'^2 + W'^2]\right\}$, $D = -\frac{5}{4}\sqrt{\pi}\beta G\lambda$, $\beta = \frac{1}{\sqrt{2RT}}$, λ is the mean free path of air, R is the gas constant, U_0, V_0, W_0 are mass average velocity components, and $U' = U - U_0, V' = V - V_0, W' = W - W_0$ are the thermal velocity components. Note that the mass average velocity is different from the velocity of the shear flow since the coordinate system is fixed to the sphere, which is itself rotating with an angular velocity Ω.

3.3 Forces on a unit area on the surface of the sphere

To calculate the forces on a unit area at a specific location on the surface of the sphere, we set up a local coordinate system $\{xyz\}$ at that location, as shown in Fig. 3.1. The y direction points to the center of the sphere while the x and z directions are tangential to the parallel and meridian, respectively. Let u, v, w denote the velocity components in this local coordinate system. Then the Chapmann-Enskog distribution, when expressed in terms of u, v, w is of the same form as Eq. (3.2), but now

$$U'V' = u'w' \sin\theta \sin\phi - u'v' \cos\theta \sin\phi + \frac{1}{2}(w'^2 - v'^2) \sin 2\theta \cos\phi - v'w' \cos 2\theta \cos\phi \tag{3.3}$$

and

$$f_0 = \left(\frac{\beta}{\sqrt{\pi}}\right)^3 \exp\left\{-\beta^2[(u-u_0)^2 + (w-v_0)^2 + (w-w_0)^2]\right\} \tag{3.4}$$

where u_0, v_0, and w_0 are related to U_{f0} as discussed in next two sections.

According to kinetic theory [Schaaf and Chambré 1961; Bird 1994], the normal force along the y direction is

$$p = p_i + p_r = (2 - \sigma_p)p_i + \sigma_p p_w \tag{3.5}$$

and the shear forces along the x and z directions are

$$\tau_x = \tau_{xi} - \tau_{xr} = \sigma_\tau \tau_{xi} \tag{3.6}$$

$$\tau_z = \tau_{zi} - \tau_{zr} = \sigma_\tau \tau_{zi} \tag{3.7}$$

In the above expressions, $p_i, \tau_{xi}, \tau_{zi}$ are due to the incoming molecules while $p_r, \tau_{xr}, \tau_{zr}$ are contributed by the molecules reflected by the sphere. p_w is the pressure due to the outgoing molecules that obey the equilibrium Maxwellian distribution function f_0 at the wall temperature. Here we assume the sphere is thermally highly conductive and of uniform temperature T_w, which is assumed to be the same as the temperature T_∞ at infinity. $\sigma_p = \frac{p_i - p_r}{p_i - p_w}$ and $\sigma_\tau = \frac{\tau_i - \tau_r}{\tau_i}$ are accommodation coefficients, which represent the percentage of incoming molecules that are diffusely reflected, or are accommodated to a Maxwellian distribution at the wall temperature. Here we allow for different accommodation coefficients for normal and shear forces.

Based on the assumption of a highly rarefied gas [Schaaf and Chambré 1961],

$$\begin{aligned} p_i &= \rho \int_{-\infty}^{+\infty} \int_{0}^{+\infty} \int_{-\infty}^{+\infty} v^2 f \mathrm{d}u\mathrm{d}v\mathrm{d}w \\ \tau_{xi} &= \rho \int_{-\infty}^{+\infty} \int_{0}^{+\infty} \int_{-\infty}^{+\infty} uv f \mathrm{d}u\mathrm{d}v\mathrm{d}w \\ \tau_{zi} &= \rho \int_{-\infty}^{+\infty} \int_{0}^{+\infty} \int_{-\infty}^{+\infty} wv f \mathrm{d}u\mathrm{d}v\mathrm{d}w \end{aligned} \tag{3.8}$$

where the lower limit for v is 0 since we are considering only the incoming molecules.

Using the Chapman-Enskog distribution function expressed in the local coordinate system, we can integrate the above equations to get the normal and shear forces. The integration is actually performed with u', v', w' and the results are

$$\begin{aligned} p_i = & \frac{\rho}{2\sqrt{\pi}\beta^2}\left\{\beta v_0 \exp(-\beta^2 v_0^2) + \sqrt{\pi}(\frac{1}{2}+\beta^2 v_0^2)[1+\mathrm{erf}(\beta v_0)]\right\} \\ & - \frac{\rho D}{4\beta^4}[1+\mathrm{erf}(\beta v_0)]\sin\theta\cos\theta\cos\phi \end{aligned} \tag{3.9}$$

$$\begin{aligned} \tau_{xi} = & \frac{\rho U_{f0}}{2\sqrt{\pi}\beta}\left(\sin\phi - \frac{\Omega R_0}{U_{f0}}\sin\theta\right)\left\{\exp(-\beta^2 v_0^2) + \sqrt{\pi}\beta v_0[1+\mathrm{erf}(\beta v_0)]\right\} \\ & - \frac{\rho D}{8\beta^4}[1+\mathrm{erf}(\beta v_0)]\sin\phi\cos\theta - \frac{\rho D}{4\sqrt{\pi}\beta^3}u_0\exp(-\beta^2 v_0^2)\sin\theta\cos\theta\cos\phi \end{aligned} \tag{3.10}$$

$$\begin{aligned} \tau_{zi} = & \frac{\rho w_0}{2\sqrt{\pi}\beta}\left\{\exp(-\beta^2 v_0^2) + \sqrt{\pi}\beta v_0[1+\mathrm{erf}(\beta v_0)]\right\} \\ & + \frac{\rho D}{8\beta^4}[1+\mathrm{erf}(\beta v_0)](\sin^2\theta - \cos^2\theta)\cos\phi - \frac{\rho D}{4\sqrt{\pi}\beta^3}u_0\exp(-\beta^2 v_0^2)\sin\theta\cos\theta\cos\phi \end{aligned} \tag{3.11}$$

where $\mathrm{erf}(z) = \frac{2}{\sqrt{\pi}}\int_0^z \mathrm{e}^{-t^2}dt$ is the error function.

Based on the previous discussion, p_w denotes the pressure due to the outgoing molecules as if they all obey the Maxwellian velocity distribution function at the wall temperature. The contribution from every molecule of this kind is

$$\frac{p_w}{N_w} = \frac{\int_{-\infty}^{+\infty}\int_{-\infty}^{0}\int_{-\infty}^{+\infty} v^2 f_0 \mathrm{d}u\mathrm{d}v\mathrm{d}w}{\int_{-\infty}^{+\infty}\int_{-\infty}^{0}\int_{-\infty}^{+\infty} f_0 \mathrm{d}u\mathrm{d}v\mathrm{d}w} \tag{3.12}$$

where N_w is the number of molecules. From the conservation of the number of molecules, N_w is equal to the total number of incoming molecules:

$$N_w = n\int_{-\infty}^{+\infty}\int_{0}^{+\infty}\int_{-\infty}^{+\infty} v f \mathrm{d}u\mathrm{d}v\mathrm{d}w \tag{3.13}$$

where n is the volume density of molecules. Thus

$$\begin{aligned} p_w &= N_w\frac{m\sqrt{\pi}}{2\beta} \\ &= \frac{\rho}{4\beta^2}\left\{\exp(-\beta^2 v_0^2) + \sqrt{\pi}\beta v_0[1+\mathrm{erf}(\beta v_0]\right\} - \frac{\rho D}{8\beta^4}\mathrm{e}^{-\beta^2 v_0^2}\sin\theta\cos\theta\cos\phi \end{aligned} \tag{3.14}$$

For a sphere rotating in an otherwise uniform flow, $D = 0$ and Eqs. (3.9)– (3.11) and (3.14) reduce to Wang's corresponding results [Wang 1972].

3.4 Special case: the axis of rotation is the same as the gradient of the shear flow

To illustrate our approach to getting the total force and torque on the particle, we first consider a simple case where the axis of rotation is the same as the gradient of the shear

flow. This case has a simple relationship relating the local and global mass average velocity: $u_0 = U_{f0}\sin\phi - \Omega R_0 \sin\theta, v_0 = U_{f0}\sin\theta\cos\phi$ and $w_0 = U_{f0}\cos\theta\cos\phi$.

Based on the above results in Sec. 3.3, the total force can be obtained by performing the integration of the force components over the surface of a sphere. To do this, we need to transform all of the above formulae back to the global coordinate system. According to the geometry shown in Fig. 3.1,

$$F_X = \int_0^{2\pi}\int_0^{\pi} \{p\sin\theta\cos\phi + \tau_x\sin\phi + \tau_z\cos\theta\cos\phi\}\, R_0^2\sin\theta \mathrm{d}\theta\mathrm{d}\phi \tag{3.15}$$

Using the results for p, τ_x, τ_z obtained above in Eq. (3.15), we obtain, after lengthy integration, the *drag force* in the X direction as

$$F_X = \frac{1}{2}\pi R_0^2 \rho U_{f0}^2 \left\{ \frac{2-\sigma_p+\sigma_\tau}{2S^3}\left[\frac{4S^4+4S^2-1}{2S}\mathrm{erf}(S) + \frac{2S^2+1}{\sqrt{\pi}}\mathrm{e}^{-S^2}\right] + \frac{2\sigma_p}{3S}\sqrt{\pi}\right\} \tag{3.16}$$

where $S = U_{f0}/\sqrt{2RT}$. Equation (3.16) is a well-known result [Kogan 1969] and is the same as the drag force obtained by Wang for a particle rotating in a uniform flow of a highly rarefied gas [Wang 1972]. In this and the following integrations, we make use of the relation

$$\int_0^{2\pi} \mathrm{erf}(b\cos\phi)\cos\phi \mathrm{d}\phi = \frac{2b}{\sqrt{\pi}}\int_0^{2\pi} \mathrm{e}^{-b^2\cos^2\phi}\sin^2\phi \mathrm{d}\phi \tag{3.17}$$

where b is any function independent of ϕ.

The parameters of rotation and shear flow, i.e. Ω and G do not appear in Eq. (3.16), thus the drag force is not affected by the rotation of the sphere or the gradient of the shear flow. Equation (3.16) is actually the same as what would be obtained if the sphere were fixed in a uniform flow of a highly rarefied gas at the speed U_{f0}.

Similarly, we can calculate the lift force along the Y and Z directions and the results are

$$F_Z = -\frac{2}{3}\sigma_\tau \pi\rho\Omega R_0^3 U_{f0} \tag{3.18}$$

$$F_Y = -\frac{1}{6}(2+\sigma_\tau-\sigma_p)\pi\rho G R_0^2 \lambda U_{f0} \tag{3.19}$$

In Eq.(3.19), we retain only the term linear in U_{f0} since higher order terms involve βU_{f0} which is much smaller than one in our case. The direction of F_Y is along the gradient of the incoming flow. Equation (3.19) can also be written as

$$F_Y = -\frac{1}{6}(2+\sigma_\tau-\sigma_p)\pi\rho U_{f0}^2 R_0^2 \frac{\lambda}{U_{f0}/G} \tag{3.20}$$

Here U_{f0}/G corresponds to a characteristic length of the incoming flow [Bird 1994]. Thus the ratio $\frac{\lambda}{U_{f0}/G}$ in the above equation turns out to be a Knudsen number based on the shear strength of the incoming shear flow. The fact that F_Y is proportional to this Knudsen number is consistent with our use of the Chapmann-Enskog distribution, where only terms of order up to one in Knudsen number are retained.

The lift force in the Z direction involves only the rotation parameter Ω while that in the Y direction involves only G. Thus the rotation effect and shear flow effect are decoupled. It is worth pointing out that this conclusion might not be true when higher order terms are included in the velocity distribution function. But for our case, where the gradient is not large and only linear terms in Knudsen number are needed in the velocity distribution function, the rotating effect and shear flow effect do not produce any coupling effect. Equation (3.18) is the same as that derived by Wang [Wang 1972] for the case when the fluid flow is uniform.

Equation (3.19) gives the lift force in the Y direction. This force is in the opposite direction from the Saffman force, Eq. (2.3), for the case when the fluid is a continuum. Comparison of Eq. (3.19) and Eq. (2.3) shows that they have the same dependence on the velocity of the center of the sphere relative to the fluid flow and the radius of the sphere. However, the dependence on the gradient of the shear flow is different. The force is proportional to $\sqrt{G}$ when the rarefaction effect is absent but becomes linear in G when the fluid is highly rarefied. At first sight, Eq. (3.19) appears to be independent of the viscosity. But according to kinetic theory, the viscosity is proportional to $\rho\lambda$. Thus F_Y is linearly proportional to the viscosity μ in contrast to the Saffman force where the force is proportional to $\sqrt{\mu}$. The Saffman force also depends on $\sqrt{\rho}$ which is absent in Eq. (3.19).

Since the particle's size R_0 is usually quite small, F_Z, which depends on R_0^3, becomes less important than F_Y, which is proportional to R_0^2. This is the same as in the continuum case where the Saffman force is usually much more important than the Magnus force when the Reynolds number of the flow is low [Zhang and Bogy 1997a].

3.5 General case: the axis of rotation may be different from the gradient of the shear flow

For this general case, the local and global mass average velocity components are related by

$$\begin{aligned} u_0 =& U_{f0}\sin\phi - \Omega_Y R_0 \sin\theta - \Omega_X R_0 \cos\theta\cos\phi \\ &+ \Omega_Z R_0 \cos\theta \sin\phi, \qquad (3.21) \\ v_0 =& U_{f0}\sin\theta\cos\phi, \qquad (3.22) \\ w_0 =& U_{f0}\cos\theta\cos\phi + \Omega_X R_0 \sin\phi + \Omega_Z R_0 \cos\phi, \qquad (3.23) \end{aligned}$$

Using the same approach as used in Sec. 3.4, we obtain, after a lengthy integration and retaining only terms up to the linear order in βU_{f0}, the force components $\{F_X, F_Y, F_Z\}$ on

the sphere

$$\begin{aligned} F_X =& \int_0^{2\pi}\int_0^{\pi} (p\sin\theta\cos\phi + \tau_x \sin\phi \\ & +\tau_z\cos\theta\cos\phi)\, R_0^2\sin\theta \mathrm{d}\theta\mathrm{d}\phi \\ =& \frac{1}{3}\rho\sqrt{2\pi RT}\left[4(2+\sigma_\tau-\sigma_p)+\pi\sigma_p\right] R_0^2 U_{f0}, \end{aligned} \tag{3.24}$$

$$\begin{aligned} F_Y =& \int_0^{2\pi}\int_0^{\pi} (-p\cos\theta + \tau_z\sin\theta)\, R_0^2\sin\theta\mathrm{d}\theta\mathrm{d}\phi \\ =& -\frac{1}{6}(2+\sigma_\tau-\sigma_p)\pi\rho G R_0^2\lambda U_{f0} \\ & +\frac{2}{3}\sigma_\tau\pi\rho\Omega_Z R_0^3 U_{f0}, \end{aligned} \tag{3.25}$$

$$\begin{aligned} F_Z =& \int_0^{2\pi}\int_0^{\pi} (-p\sin\theta\cos\phi + \tau_x\cos\phi \\ & -\tau_z\cos\theta\sin\phi)\, R_0^2\sin\theta\mathrm{d}\theta\mathrm{d}\phi \\ =& -\frac{2}{3}\sigma_\tau\pi\rho\Omega_Y R_0^3 U_{f0}, \end{aligned} \tag{3.26}$$

and the torque components $\{T_X, T_Y, T_Z\}$ about the center of the sphere

$$\begin{aligned} T_X =& \int_0^{2\pi}\int_0^{\pi} (\tau_x\cos\theta\cos\phi - \tau_z\sin\phi)\, R_0^3\sin\theta\mathrm{d}\theta\mathrm{d}\phi \\ =& -\frac{4}{3}\sigma_\tau\rho R_0^4\sqrt{2\pi RT}\Omega_X - \frac{1}{12}\sigma_\tau\rho\pi R_0^4\lambda G\Omega_Y, \end{aligned} \tag{3.27}$$

$$\begin{aligned} T_Y =& \int_0^{2\pi}\int_0^{\pi} \tau_x R_0^3\sin^2\theta\mathrm{d}\theta\mathrm{d}\phi \\ =& -\frac{4}{3}\sigma_\tau\rho R_0^4\sqrt{2\pi RT}\Omega_Y - \frac{1}{12}\sigma_\tau\rho\pi R_0^4\lambda G\Omega_X, \end{aligned} \tag{3.28}$$

$$\begin{aligned} T_Z =& \int_0^{2\pi}\int_0^{\pi} (-\tau_x\cos\theta\sin\phi - \tau_z\cos\phi)\, R_0^3\sin\theta\mathrm{d}\theta\mathrm{d}\phi \\ =& -\frac{4}{3}\sigma_\tau\rho R_0^4\sqrt{2\pi RT}\Omega_Z + \frac{5(2\pi-1)}{48}\sigma_\tau\rho R_0^3\sqrt{2\pi RT}\lambda G, \end{aligned} \tag{3.29}$$

or written in vector form

$$\begin{aligned}\mathbf{F} =& \frac{1}{3}\rho\sqrt{2\pi RT}\left[4(2+\sigma_\tau-\sigma_p)+\pi\sigma_p\right]R_0^2\mathbf{U}_{f0}\\ &-\frac{2}{3}\sigma_\tau\rho\pi R_0^3\mathbf{U}_{f0}\times\mathbf{\Omega}\\ &-\frac{1}{6}(2+\sigma_\tau-\sigma_p)\rho\pi R_0^2U_{f0}\lambda\mathbf{G} \qquad (3.30)\\ \mathbf{T} =& -\frac{4}{3}\sigma_\tau\rho R_0^4\sqrt{2\pi RT}\mathbf{\Omega}\\ &-\frac{1}{12}\sigma_\tau\rho\pi R_0^4\lambda\left(\mathbf{G}\cdot\mathbf{\Omega}\frac{\mathbf{U}_{f0}}{U_{f0}}+\frac{\mathbf{\Omega}\cdot\mathbf{U}_{f0}}{U_{f0}}\mathbf{G}\right)\\ &+\frac{5}{48}(2\pi-1)\sigma_\tau\rho R_0^3\sqrt{2\pi RT}\lambda\frac{\mathbf{U}_{f0}\times\mathbf{G}}{U_{f0}} \qquad (3.31)\end{aligned}$$

where $\mathbf{G}=G\mathbf{J}$, $\mathbf{\Omega}=\Omega_X\mathbf{I}+\Omega_Y\mathbf{J}+\Omega_Z\mathbf{K}$, and $\{\mathbf{IJK}\}$ are the unit vectors along the $\{XYZ\}$ axes in the global coordinate system respectively.

The first term in Eq. (3.30) is the drag force experienced by the particle. At first sight, this term looks different from the well-known result for the drag force on a sphere moving in a quiescent flow of a highly rarefied gas. Since we consider here the case in which the speed of the flow is much less than the speed of sound, only terms up to the linear order in βU_{f0} are retained, and the first term in Eq. (3.30) is just the reduced form of the general drag force formula with higher order terms in βU_{f0} neglected. The second term in Eq. (3.30) is the lift force induced by the rotation, and the last term is the lift force induced by the nonuniformity of the flow. These lift forces have opposite directions from their counterparts in a continuum flow. For the particular case of a particle rotating about an axis perpendicular to the incoming uniform flow of a highly rarefied gas, i.e., $\Omega_Z=0$ and $G=0$, Eq. (3.30) reduces to Wang's result [Wang 1972]. When the axis of rotation is in the same direction as the shear direction, i.e., $\Omega_X=\Omega_Z=0$, Eq. (3.30) reduces to the formula derived in Ref. [Liu and Bogy 2008]. The contributions of the shear and the rotation to the total force are decoupled, which is the same as in the special case studied in Sec. 3.4 [Liu and Bogy 2008].

As in the continuum case [Saffmann 1965], the torque $\mathbf{T}$ is independent of U_{f0}. However, due to the rarefaction of the gas, the torque here is proportional to the tangential accommodation coefficient σ_τ. The normal accommodation coefficient σ_p does not come into play since the normal force at any location on the surface of the sphere produces no torque. The first term in Eq. (3.31) is induced by the particle's rotation and is along the direction of the axis of rotation. A similar result exists for a particle rotating in a continuum flow, since, due to asymmetry of the flow field, the forces experienced by the upper half and lower half spheres are different, and torque arises. The last term in Eq. (3.31) is induced by the nonuniformity of the flow and points to a direction perpendicular to both the flow direction and the gradient direction of the flow. A particle moving in a linear shear flow of a continuum fluid experiences a similar torque, which is again induced by the asymmetry of the flow field around the sphere. The second term in Eq. (3.31) is due to the coupling effect of the shear and the rotation. This term is absent in the classical analysis of a particle rotating in a linear shear flow of a continuum fluid [Saffmann 1965]. This kind of classical analysis is

usually based on the linear Stokes equation, which is a reduced Navier–Stokes equation for the case when the flow velocity is so small or the viscosity is so large that the inertial effect can be neglected. Due to the linearity of the Stokes flow, the effects of rotation and shear are decoupled and no coupling terms similar to the second term in Eq. (3.31) appears. Lift force can not exist in such a Stokes flow analysis as well. In a classical paper analyzing the motion of a sphere in a weak shear flow of a continuum fluid, Saffman [Saffmann 1965] used a perturbation method [Van Dyke 1975] and derived an analytical formula for the lift force on the sphere. Due to the complexity involved in this derivation, he did not carry out the study of the torque to the same level of approximation as the lift force. Since the Navier-Stokes equation itself is nonlinear, coupling between the shear and the rotation effects might also exist for the continuum case based on it rather than the Stokes approximation.

The terms solely due to the rotation effects, i.e., the first terms in Eq. (3.30) and (3.31), are independent of the Knudsen number while the other terms, involving $\mathbf{G}$, are all of the first order in the Knudsen number Kn_G since the term λG can be written as $U_{f0}\lambda/(U_{f0}/G)$, or $U_{f0}\mathrm{Kn}_G$. This fact is consistent with our use of the Chapman-Enskog distribution function where only terms up to the linear order in Kn_G are retained.

Given the formulae Eqs. (3.30) and (3.31), the motion of particles in a shear flow of a highly rarefied gas, with appropriate initial conditions, can be determined from Newton's second law.

3.6 Conclusion

In summary, the force and torque on a spherical particle in a weak shear flow of a highly rarefied gas are investigated in this chapter. Built upon previous results for the forces on a unit area of the surface of the sphere, we derive analytical formulae for the force and the torque, which include as special cases Wang's formula [Wang 1972] for the force on a sphere rotating in a uniform flow of a highly rarefied gas and the formula for the force on a sphere rotating around an axis restricted to be along the same direction as the gradient direction of the flow in a linear shear flow of a highly rarefied gas. It is shown that the coupling effect of the shear and rotation does not appear in the force but it is present in the torque. When the characteristic length scale of a general flow is much larger than the size of the particle, the flow can be locally approximated as a linear shear flow, and the present formulae can then be used to calculate the force and torque on the sphere in this case as well. This knowledge of the force and torque on the sphere lays a foundation for the analysis of the motion of particles in the above mentioned cases.

Chapter 4

Effect of lift force on particle contamination on a slider

4.1 Introduction

Contaminated particles on a slider might impact and scratch the disk and lead to the loss of information data stored on the disk, which makes particle contamination an important issue for a slider's flying performance. To understand this phenomenon, we need to calculate the particle's motion inside the HDI, and the essential part of this calculation is the force on a particle, from which the particle's trajectory can be calculated based on Newton's second law, as shown in Chapter 2 [Zhang and Bogy 1997a]. The lift force is one of the two major contributions to the total force, and it is mainly induced by the non-uniformity of the flow field, since the other component of the lift force induced by the particle's rotation is insignificant. Since the gap spacing at the entrance is about 300 nanometers, the sizes of the particles entering the HDI range from several nanometers to around 300 nanometers. Although the lift force is negligible for a particle whose radius is less than 100nm, it does affect relatively large particles, which could induce more severe damage to the disk due to their larger sizes.

The formula used in previous studies to calculate the lift force, or more specifically, the Saffman force which is the part induced by the non-uniformity of the flow field, was based on a formula derived for a particle moving in a continuum flow. Since the air gap thickness in the HDI as well as the particle's size is comparable to the mean free path of the air, the gas rarefaction effect needs to be considered and continuum theory no longer holds. Fully understanding lift force on a particle moving in a rarefied gas requires solving the Boltzmann equation, and no results are currently available. To get an idea of how large this force is, we investigated the lift force on a particle in a shear flow of a highly rarefied gas in the last chapter. In this chapter, we consider another case where analytical results exists: the lift force on a particle moving in a slightly rarefied gas. Based on information obtained from these two limit cases, we discuss the accuracy of using the continuum-theory based formula to calculate Saffman force.

This chapter is organized as follows. The first two sections discuss the lift force on a particle in a slightly rarefied gas: Section 4.2 discusses theoretical background and Section 4.3 derives the analytical formula. Section 4.4 discusses how a particle's simulated trajectory is

affected by the continuum-based formula to calculate the Saffman force. A summary and conclusion is given in Sec. 4.5.

4.2 Statement of the problem

We consider here a rotating sphere with angular velocity Ω in a weak shear flow, for which the velocity field, $\mathbf{u}$, satisfies

$$-\nabla p + \mu\nabla^2\mathbf{u} = \rho\mathbf{u}\cdot\nabla\mathbf{u} \tag{4.1}$$

A coordinate system is set up with its origin lying at the center of the sphere. Its x axis

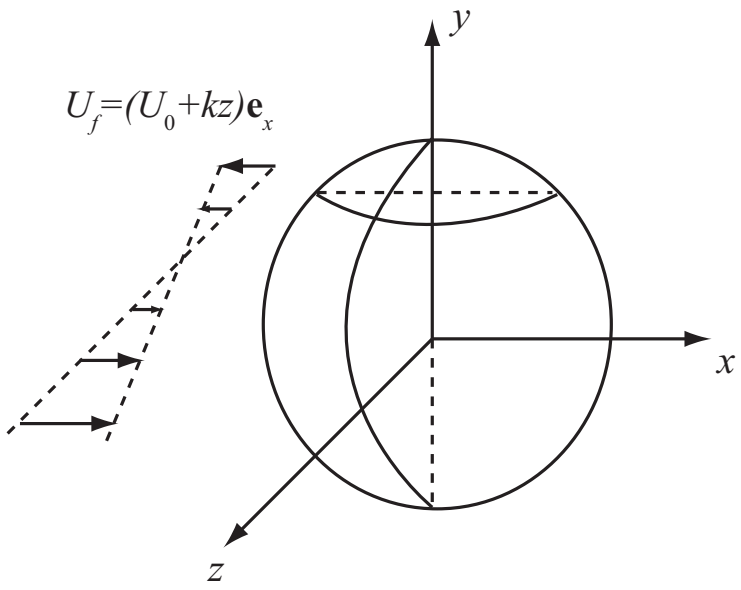

Figure 4.1: The coordinate system

points to the flow direction while the z axis coincides with the gradient of the flow field, as shown in Fig. 4.1.

The boundary condition remote from the sphere is that the influence of the presence of the sphere vanishes, i.e. the velocity $\mathbf{u}$ approaches $(U+kz)\mathbf{e_x}$ as $\mathbf{r}$ goes to infinity. On the surface of the sphere, the Maxwell slip boundary condition allowing for velocity slip is enforced. It requires that the velocity jump in the tangential direction be linearly proportional to the shear force on the surface of the sphere [Basset 1888; Lamb 1945; Lockerby et al. 2004; Lauga et al. 2007], or

$$\beta(\mathbf{u}-(\mathbf{u}\cdot\mathbf{n})\mathbf{n}) = \boldsymbol{\tau}\cdot\mathbf{n} - (\mathbf{n}\cdot\boldsymbol{\tau}\cdot\mathbf{n})\mathbf{n} \quad \text{at} \quad r=R \tag{4.2}$$

where, in a slightly rarefied gas, β is inversely proportional to the mean free path of the air λ. The classical Maxwell slip boundary condition states that $\beta = (\sigma/(2-\sigma))(\mu/\lambda)$ where σ is a constant related to the material property of the sphere, and it needs to be determined

experimentally. For a hydrophobic or porous surface β is related to the slip length λ_s. The last boundary condition is the continuity of the normal velocity on the surface of the sphere:

$$\mathbf{u}\cdot\mathbf{n}=0 \quad \text{at} \quad r=R \tag{4.3}$$

As shown by Saffman [Saffmann 1965], the force on the sphere can be expressed as

$$\mathbf{F}=-\int p\frac{\mathbf{r}}{r}dS-\int\frac{\mathbf{u}}{r}dS-r\frac{d}{dr}\int\frac{\mathbf{u}}{r}dS-\rho\int\mathbf{u}\frac{\mathbf{u}\cdot\mathbf{r}}{r}dS \tag{4.4}$$

where the integrals are performed on any spherical surface concentric to the sphere and with $r\geq R$. When the integrals are calculated on the surface of the sphere, i.e. with $r=R$, the last term vanishes due to the boundary condition Eq. (4.3).

Since the Reynolds number of interest here is quite small, the right hand side of Eq. (4.1), due to the inertial effect, is also very small. Thus the inertia will only introduce a small correction to the solution of corresponding creeping flow, which satisfies Eq. (4.1) with a zero right hand side. Therefore the solution can be expand in the order of Reynolds number, or, correspondingly, the inverse of the viscosity. Since the lift force is actually a first order effect, terms of an order higher than 1 are neglected in the expansion. We use superscripts (0) and (1) to denote zeroth and first order solutions. For example, the velocity is $\mathbf{u}=\mathbf{u}^{(0)}+\mathbf{u}^{(1)}$.

Substituting the expansion of each quantity into Eq. (4.1), we find the zeroth order solution satisfies the equation of creeping flow and is subject to the above three boundary conditions. The solution is obtained here by using Lamb's general solution [Lamb 1945]. Following Lamb's original notation, the general solution of the creeping flow is

$$\begin{aligned}\mathbf{u}^{(0)}=&(U+kz)\mathbf{e}_x+\frac{1}{\mu}\sum\left\{\frac{r^2}{2(2n+1)}\nabla p_n\right.\\&\left.+\frac{nr^{2n+3}}{(n+1)(2n+1)(2n+3)}\nabla\frac{p_n}{r^{2n+1}}\right\}\\&+\sum\{\nabla\phi_n+\nabla\chi_n\times\mathbf{r}\}\end{aligned} \tag{4.5}$$

and

$$p^{(0)}=\sum\frac{p_n}{r^n} \tag{4.6}$$

Here p_n, ϕ_n and χ_n are solid spherical harmonics and satisfy

$$xu+yv+zw=\frac{1}{\mu}\sum\frac{nr^2p_n}{2(2n+3)}+\sum n\phi_n \tag{4.7}$$

$$x\xi+y\eta+z\zeta=\sum n(n+1)\chi_n \tag{4.8}$$

where $\{u,v,w\}$ and $\{\xi,\eta,\zeta\}$ are the velocity and vorticity of the flow, respectively. When the velocity remote from the sphere is used in Eq. (4.7)-(4.8), we find that only p_0, p_{-2}, p_{-3}, ϕ_{-2}, ϕ_{-3} and χ_{-2} need to be considered. The determination of these nonzero terms involves

the application of the boundary conditions and is quite cumbersome. The final results are

$$p_{-2} = -\frac{3}{2}\mu U R \frac{2\mu + \beta R}{3\mu + \beta R}\frac{x}{r} \tag{4.9}$$

$$p_{-3} = -\frac{36\mu^2 R^3 + 11\mu\beta R^4 + 11\beta^2 R^5}{\mu - \frac{5}{2}\beta R - \frac{\beta^2}{2\mu}R^2}\frac{kxz}{r} \tag{4.10}$$

$$\phi_{-2} = -\frac{1}{4}U R^3 \frac{\beta R}{3\mu + \beta R}\frac{x}{r} \tag{4.11}$$

$$\phi_{-3} = -\frac{12\mu R^5 + 6\beta R^6 + 5\frac{\beta^2}{\mu}R^5}{20\mu - 50\beta R - 5\frac{\beta^2}{\mu}R^2}\frac{kxz}{r} \tag{4.12}$$

$$\chi_{-2} = \frac{\beta R^4}{3\mu + \beta R}(\Omega - \frac{1}{2}k)\frac{y}{r^3} \tag{4.13}$$

The term p_0 is shown to be an undetermined constant, whose value is not of concern since we will only encounter its gradient in the following derivation.

Making use of Eq. (4.4), we find the drag force is

$$\mathbf{F}^{(0)} = \frac{2\mu + \beta R}{3\mu + \beta R} 6\pi\mu U R \mathbf{e}_x \tag{4.14}$$

and the torque is

$$\mathbf{T}^{(0)} = \frac{\beta R}{3\mu + \beta R} 8\pi R^3 (\frac{1}{2}k - \Omega)\mathbf{e}_y \tag{4.15}$$

Due to the linearity of the equation of creeping flow, no lift forces can exist at this order. Thus, we need to solve the first order system, which satisfies Eq. (4.1) with its right hand side replaced by $\mathbf{Q} = \rho\mathbf{u}^{(0)} \cdot \nabla\mathbf{u}^{(0)}$. As shown by Saffman [Saffmann 1965], the non-zero integrals involved in Eq. (4.4) are related to $\mathbf{Q}$ by

$$\int p^{(1)}\frac{\mathbf{r}}{r}dS = \sum \frac{\mathbf{b}_n r^{n+1}}{(n+1)(n-2)} + \mathbf{A} + \mathbf{B}r^3 \tag{4.16}$$

$$\int \frac{\mathbf{u}^{(1)}}{r}dS = \sum \frac{\mathbf{a}_n r^{n+1}}{n(n+1)} + \sum \frac{\mathbf{b}_n r^{n+1}}{n(n+1)(n-2)} + \mathbf{C}r + \mathbf{D} + \frac{1}{2}\mathbf{B}r^3 \tag{4.17}$$

Here the terms containing $\mathbf{a}_n$ and $\mathbf{b}_n$ correspond to a particular solution of Eq. (4.1) with a non-zero right hand side $\mathbf{Q}$, and $\mathbf{a}_n$ and $\mathbf{b}_n$ are obtained from

$$\int \mathbf{Q}dS = \sum \mathbf{a}_n r^n \tag{4.18}$$

$$\int \mathbf{r}\nabla \cdot \mathbf{Q}dS = \sum \mathbf{b}_n r^n \tag{4.19}$$

The other terms in Eqs. (4.16)– (4.17) are general solutions of Eq. (4.1) with a zero right hand side and $\mathbf{A}$, $\mathbf{B}$, $\mathbf{C}$ and $\mathbf{D}$ are unknown constants to be determined by boundary conditions. These terms dominate the lift force due to a non-uniform flow field [Saffmann 1965].

4.3 Lift force due to a nonuniform flow field

Legendre and Magnaudet's solution, based on an order analysis, shows that the terms containing $\mathbf{a}_n$, $\mathbf{b}_n$ and $\mathbf{B}$ are at least one order smaller than the others [Legendre and Magnaudet 1997]. Thus, the two integrals, after terms of smaller orders are neglected, become

$$\int p^{(1)} \frac{\mathbf{r}}{r} dS = \mathbf{A} \tag{4.20}$$

$$\int \frac{\mathbf{u}^{(1)}}{r} dS = \mathbf{C}r + \mathbf{D} \tag{4.21}$$

To get the lift force, we need to solve for the velocity field near the sphere and match it with the far field solution to determine $\mathbf{A}$, $\mathbf{C}$ and $\mathbf{D}$. This process is actually not necessary due to an observation first presented by Lengendre and Magnaudet [Legendre and Magnaudet 1997]. The basic idea is that only a relation between $\mathbf{A}$, $\mathbf{C}$ and $\mathbf{D}$ is needed since $\mathbf{C}$ can be determined from the far field solution, which itself is obtained from McLaughlin's results, as shown below. Since the particular solution containing $\mathbf{A}$, $\mathbf{C}$ and $\mathbf{D}$ satisfies the same equation and boundary conditions on the sphere as the zeroth order solution, the relationship between $\mathbf{A}$, $\mathbf{C}$ and $\mathbf{D}$ is obtained by a comparison with the zeroth order solution, for which,

$$\int p^{(0)} \frac{\mathbf{r}}{r} dS = -2\pi\mu U R \frac{2\mu + \beta R}{3\mu + \beta R} \mathbf{e}_x \tag{4.22}$$

$$\int \frac{\mathbf{u}^{(0)}}{r} dS = 4\pi U (r - \frac{2\mu + \beta R}{3\mu + \beta R} R) \mathbf{e}_x \tag{4.23}$$

Comparing Eqs. (4.20)– (4.23), we get

$$\mathbf{A} = -\frac{2\mu + \beta R}{3\mu + \beta R} \frac{\mu R}{2} \mathbf{C} \qquad \mathbf{D} = -\frac{2\mu + \beta R}{3\mu + \beta R} R\mathbf{C} \tag{4.24}$$

Thus using Eq. (4.24) in Eq. (4.4), we get

$$F_z = \frac{2\mu + \beta R}{3\mu + \beta R} \frac{3\mu R}{2} C_z \tag{4.25}$$

The determination of C_z requires solving for the velocity field far from the sphere, which satisfies

$$\rho(U + kz) \frac{\partial \mathbf{v}}{\partial x} + \rho k (\mathbf{v} \cdot \mathbf{e}_z) \mathbf{e}_x = -\nabla p + \mu \nabla^2 \mathbf{v} - \mathbf{F}^0 \delta(\mathbf{r}) \tag{4.26}$$

where $\mathbf{v} = \mathbf{u} - (U + kz)\mathbf{e}_x$. The effect of the presence of the sphere on the far field solution is included here as a point force opposite to the drag force on the sphere.

Due to the linearity of Eq. (4.26), C_z can be obtained from Eq. (4.26) based on McLaughlin's results [McLaughlin 1991] and

$$C_z = \frac{1}{\pi^2} |\mathbf{F}^{(0)}| \sqrt{\frac{k\rho}{\mu}} J \mathrm{sgn}(k) \tag{4.27}$$

where J is an integral which approaches 2.255 when Saffman's restriction holds and has been numerically evaluated by McLaughlin.

From Eqs. (4.14), (4.25) and (4.27), we obtain the Saffman force

$$\mathbf{F}^{slip}_{saffman} = \frac{9}{\pi}\frac{(2\mu+\beta R)^2}{(3\mu+\beta R)^2}\mu R^2 U\sqrt{\frac{k\rho}{\mu}}J\mathrm{sgn}(k)\mathbf{e}_z \tag{4.28}$$

For a sphere moving in a slightly rarefied gas, the continuum theory with a first order slip boundary condition is only applicable for Knudsen numbers, corresponding to $\mu/\beta R$ here, up to 0.1, beyond which the kinetic theory is needed. But as a check of our results, we consider the case where the Knudsen number approaches infinity. In this case the problem is the same as that for a spherical gas bubble moving in a weak shear flow, which has already been studied by Lengendre and Magnaudet [Legendre and Magnaudet 1997]. Our results show that the Saffman force is reduced to 4/9 of its value when no slip exists on the surface of the sphere, which agrees with the results of Lengendre and Magnaudet.

For a sphere with hydrophobic or porous surfaces, it is more convenient to express all of the results in terms of slip length $\lambda_s = \mu/\beta$:

$$\mathbf{F}_{drag} = 6\pi\mu U R\frac{2\lambda_s + R}{3\lambda_s + R}\mathbf{e}_x \tag{4.29}$$

$$\mathbf{F}^{slip}_{saffman} = \frac{9}{\pi}\frac{(2\lambda_s+R)^2}{(3\lambda_s+R)^2}\mu R^2 U\sqrt{\frac{k\rho}{\mu}}J\mathrm{sgn}(k)\mathbf{e}_z \tag{4.30}$$

$$\mathbf{T} = \frac{R}{3\lambda_s + R}8\pi R^3(\frac{1}{2}k - \Omega)\mathbf{e}_y \tag{4.31}$$

Figure 4.2 shows how the forces and the torque change with $\mu/\beta R$ that corresponds to the Knudsen number for a sphere moving in a rarefied gas and λ_s/R for a sphere with hydrophobic or porous surfaces. Although the Knudsen number should be less than 0.1 for our formulae to apply, there is no limit on λ_s/R. Thus the abscissa in Fig. 4.2 goes from 0.01 to 10. Both the forces and the torque decrease with Knudsen number with the torque decreasing fastest and the drag force slowest. The drag force is the same as that for a stationary sphere lying in an otherwise uniform flow with velocity $\mathbf{U}$.

4.4 Effect of lift force on a particle's motion in the HDI

In previous studies [Zhang and Bogy 1997a; Shen et al. 2004], the Saffman force was calculated through Eq. (2.3) which is derived from continuum theory with no-slip boundary conditions on the surface of the sphere and is not guaranteed to apply to a particle moving in the HDI. In order to fully understand Saffman force on a particle moving in a rarefied gas, we must solve the full Boltzmann equation which is not manageable even from the view point of numerical solutions, so we here estimate the accuracy of using Eq. (2.3) to calculate

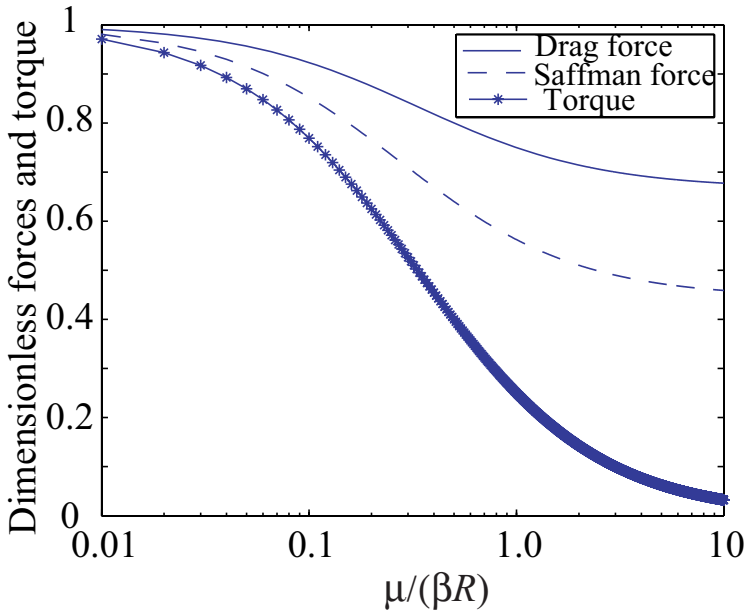

Figure 4.2: The drag and lift forces as well as the torque on a sphere with slip flow. Each quantity is nondimensionalized by its value with no slip. Kn $= \mu/\beta R$ for a sphere moving in a rarefied gas and Kn $= \lambda_s/R$ for a sphere with hydrophobic or porous surfaces.

Saffman force based on Eqs. (3.18) and (4.28). The ratio of Saffman force predicted by Eq. (3.19) and that by Eq. (2.3) is

$$\frac{Eq.\ (3.19)}{Eq.\ (2.3)} \sim \frac{\rho U_{f0} R_0^2 \lambda G}{\mu R_0^2 U_{f0} \sqrt{|G|\rho_g/\mu}} = \sqrt{\frac{\lambda G}{U_{f0}}} \sqrt{\frac{\lambda U_{f0}}{\mu}} \tag{4.32}$$

where ρ is the air density, U_{f0} is the air velocity relative to the center of the sphere, R_0 is the sphere's radius, λ is the mean free path, G is the gradient of the air flow field, μ is the air viscosity.

Given that $\lambda G/U_{f0} \ll 1$ implicit in the use of Chapman-Enskog velocity distribution function, Eq. (4.32) shows that Eq. (2.3) over predicts the Saffman force. However, for our situation, Saffman force is only important for particles with a radius larger than 100nm. Most of this kind of particles move in the recess region where the air gap thickness is about several micrometers. Since the air pressure in the recess region is close to the ambient pressure, the mean free path of air here is close to 65nm and the Knudsen number for a particle of a diameter of 200nm is about 0.3, making Eq. (4.28) a good formula to estimate the Saffman force on the sphere. From Fig. 4.2, we see that the Saffman force for a Knudsen number of 0.3 is about 0.85 times its value for a continuum fluid, and Eq. (2.3) still over predicts the Saffman force. However, the numerical simulation based on Eq. (4.28) instead of Eq. (2.3) does not show much difference. Although the number of particles contaminated on the slider is slightly different for these two cases, there is not noticeable pattern change for the particle contamination profile. We thus conclude that the current particle contamination code is sufficiently accurate despite the fact that it over predicts Saffman force on a particle moving in the HDI.

4.5 Summary and conclusion

The Saffman force on a sphere with slip at its surface in a weak shear flow is investigated in this chapter. The Maxwell slip boundary condition is used to model the velocity jump on the surface of the sphere. By solving the Navier-Stokes equation with this boundary condition, we obtain analytical formulae for the lift and drag forces as well as the torque. It is shown that the formulae for a sphere with no-slip at its surface apply when different correction factors are added for each formula. Based on the information obtained from this and the last chapters, we conclude that the current particle contamination code is sufficiently accurate despite the simple model it uses.

Chapter 5

Particle contamination on a TFC slider

5.1 Introduction

As an approach to increase HDDs' areal density and improve their reliability, the thermal flying height control sliders have been developed and introduced into commercial HDDs [Meyer et al. 1999]. In these sliders, a heating element is integrated near the read-write transducer. When power is applied to this heating element, the slider protrudes near the transducer due to its thermomechanical expansion properties, which decreases the slider's flying height at the transducer, as shown in Fig. 5.1. In this approach, the slider's temperature is raised higher than that of the disk, and therefore the temperature in the HDI is not uniform. This non-uniform temperature field induces a force, the so called thermophoretic force, on particles moving in the HDI. This force points opposite to the temperature gradient direction and is due to the different mobility of gas molecules on different parts of the surface of the particle since the temperature is a macroscopic manifestation of the gas molecules' speeds [Talbot et al. 1980; Guha 2008].

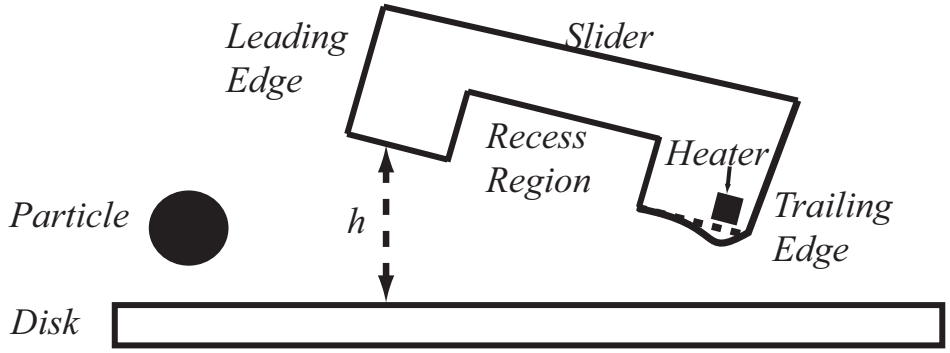

Figure 5.1: A particle moving into the HDI between a TFC slider and a disk. The slider's flying height, h, at the leading edge is around 300nm while that at the trailing edge can be as low as 10nm. A coordinate system is set up with the z axis perpendicular to the disk. Note: This figure is not to scale

For particle contamination on traditional sliders without a heating element as considered in Chapters 2–4, the air flow in the HDI is assumed to be isothermal since the slider and the disk are at the same temperature and no non-uniform temperature field exists in the HDI according to the linearized Boltzmann equation [Sone 2006]. For the TFC slider, the non-uniform temperature field in the HDI induces a thermophoretic force on the particles, and its effect on a particle's motion in the HDI and particle contamination on the slider has not yet been explored. This chapter serves to fill this gap and clarify the applicability of the current CML particle contamination simulator [Shen et al. 2004] to the TFC slider. This chapter is organized as follows. In Sec. 5.2 we discuss the calculation of the temperature field in the HDI, derive the thermophoretic force on the particle, and show how to simulate the particles' motions in the HDI. The simulation results of a particle's motion in the HDI are presented and discussed in Sec. 5.3. A summary and conclusion is given in Sec. 5.4.

5.2 Theory

5.2.1 Temperature field in the HDI

Since the air gap thickness in the HDI ranges from several nanometers to around several micrometers and the mean free path of the air is about 65nm, the air in the HDI is rarefied and the air flow in the HDI is described by the Boltzmann equation or its equivalents instead of the traditional continuum Navier-Stokes equation [Sone 2006].The exact approach to obtain the temperature field in the HDI is to solve the Boltzmann equation for the air flow between the slider and the disk at different temperatures. This approach is difficult and can not give results that are easy to implement in the CML particle contamination simulator. Since the temperature difference between the slider and the disk is much smaller than that of the slider or the disk, and the air flow speed is much less than the average thermal speed of the air molecules, which is of the same order as the speed of sound in air, the linearized Boltzmann equation is suitable for characterizing the air flow in the HDI. Based on this equation, it can be shown that the air flow problem and the temperature problem are decoupled [Sone 2006], i.e., we can neglect the air flow when calculating the temperature field in the HDI.

Due to the complexity of the (linearized) Boltzmann equation, it is still difficult to solve for the temperature field in the HDI, and an approximate approach, the method of moments [Liu and Lees 1961], is adopted here. This method can give analytical formulae, which compare well with experiments. Based on this method and the assumption that the accommodation coefficients of both the slider and the disk are equal to 1, which is a common practice in simulations related to the HDI [Zhang and Bogy 1997a,b; Shen et al. 2004; Liu and Bogy 2008], the temperature in the HDI is [Liu and Lees 1961; Lees 1965; Bird 1994]:

$$\frac{T}{T_d} = \frac{\alpha_2}{2}\sqrt{\alpha_4 - 4\beta\frac{\alpha_3}{\alpha_2}\frac{z}{h}} \tag{5.1}$$

and

$$\alpha_2 = \frac{\sqrt{(1+\beta)(L^4+2L^3+\beta)+L^2} - (L^3+2L^2-\beta-1)}{1+\beta-L^2}$$
$$\alpha_3 = 2-\alpha_2$$
$$\alpha_4 = 1-2(1+\beta)\frac{\alpha_3}{\alpha_2} + \left(\frac{\alpha_3}{\alpha_2}\right)^2$$

where $L = \sqrt{T_s/T_d}$, T_s is the slider's local temperature, T_d is the disk's temperature, $\beta = h/\lambda$, h is the air gap thickness, λ is the mean free path of air at T_d, and $z = 0$ corresponds to the disk while $z = h$ corresponds to the slider, as shown in Fig. 5.1. A typical temperature profile in the HDI is shown in Fig. 5.2.

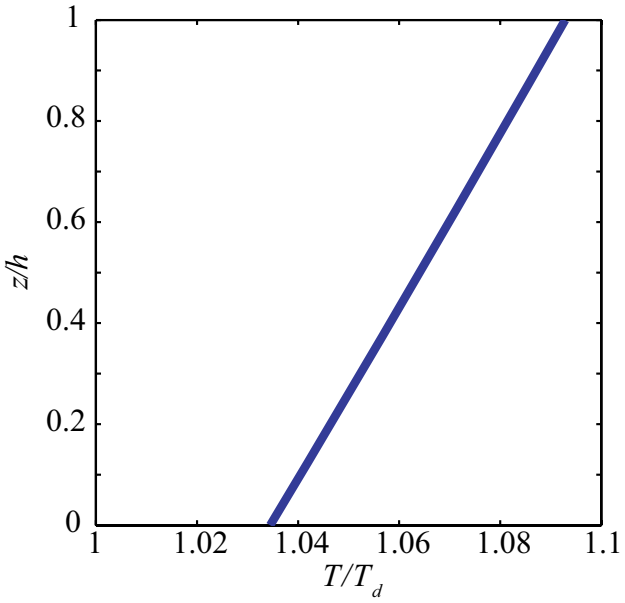

Figure 5.2: A typical temperature profile in the head-disk interface. Here $\lambda = 65$nm, $h = 1\mu$m, $T_s = 40°$C and $T_d = 20°$C. Due to the discontinuity of temperature at the boundary, the temperature near the disk is different from the temperature of the disk.

5.2.2 Thermophoretic force

The thermophoretic force is induced by the non-uniformity of the temperature field. One classical example where this force is present is in the accumulation of carbon particles on a kerosene lantern. The temperature difference between the flame and the globe produces the force which drives the particles into the globe. Since Maxwell's first investigation [Talbot et al. 1980], extensive work has been done on this topic. Brock [Brock 1962] solved the Navier-Stokes equation and the energy equation supplemented with the first order velocity and temperature slip boundary conditions, and he obtained an analytical formula for the thermophoretic force on a sphere in a non-uniform temperature field with a constant gradient.

Due to its underlying assumption of using the first order slip theory, this formula is not guaranteed to hold for a highly rarefied gas. However, when Brock's formula is applied to the latter case, it gives almost the same result as that derived by Waldmann [Waldmann 1961] for the case of a highly rarefied gas and only differs by 3% [Talbot et al. 1980]. Talbot [Talbot et al. 1980] further applied Brock's formula to an arbitrarily rarefied gas, and showed this formula agrees with experiments when appropriate values are chosen for the parameters involved in Brock's formula. For our case, Brock's formula gives [Talbot et al. 1980; Guha 2008]

$$F_T = -C_T \frac{1}{T} \frac{\partial T}{\partial z} \tag{5.2}$$

and

$$C_T = \frac{14.04\pi\mu\nu R\,(k_g/k_p + 2.18\lambda/R)}{(1 + 3.42\lambda/R)\,(1 + 2k_g/k_p + 4.36\lambda/R)}$$

where μ is the air viscosity, $\nu = \mu/\rho$, ρ is air density, R is particle radius, and k_g and k_p are thermal conductivity of the gas and the particle, respectively.

Using Eq. (5.1) in Eq. (5.2), we get the thermophoretic force on a particle moving in the HDI:

$$F_T = 2\beta C_T \frac{(1/h)(\alpha_3/\alpha_2)}{\alpha_4 - 4\beta(z/h)(\alpha_3/\alpha_2)} \tag{5.3}$$

5.2.3 Simulation of a particle's motion in the HDI

Since the volume density of particles in the HDI is much smaller than 1, collisions between particles can be neglected, and the motion of the particles is described by Newton's second law:

$$m\frac{\mathrm{d}^2\mathbf{x}}{\mathrm{d}t^2} = \mathbf{F}_{drag} + \mathbf{F}_{Saffman} + \mathbf{F}_T \tag{5.4}$$

where m is the mass of the particle and $\mathbf{x}$ is the particle's location. The first term in the right hand side of Eq. (5.4) is the drag force, which resists the motion of the particle, and the second term is the Saffman lift force, which is induced by the non-uniformity of the air flow and points in the gradient direction of the air flow. The last term is the thermophoretic force as given by Eq. (5.3). In view of the particles' small size, which is less than 1μm, other forces than those considered here can be neglected. To follow the particle's location in time, the Runge-Kutta method is used to integrate Eq. (5.4), and a suitable integration time step is chosen to ensure the convergence of the numerical method [Liu and Bogy 2008].

5.3 Results and discussions

The temperature of a TFC slider during operation only rises by less than 1°C higher than that of the disk except in the region near the transducer where the temperature can locally rise as much as 10°C [Juang et al. 2006; Aoki and Watanabe 2009]. Despite this fact, we consider here an extreme case where the slider's temperature is assumed to be uniformly 10°C higher than that of the disk, and we explore the effect of this temperature rise on the motion of particles in the HDI. For each particle moving in the HDI, two trajectories are

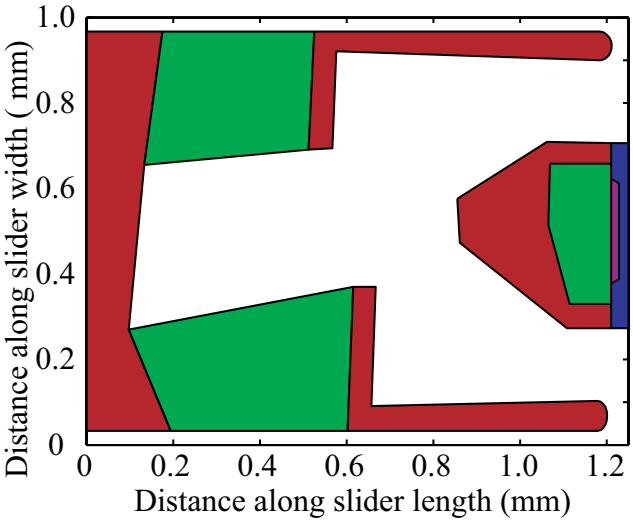

Figure 5.3: The profile of the air bearing surface used in the calculation of particle trajectories in the head-disk interface. Different color denotes different etching depth.

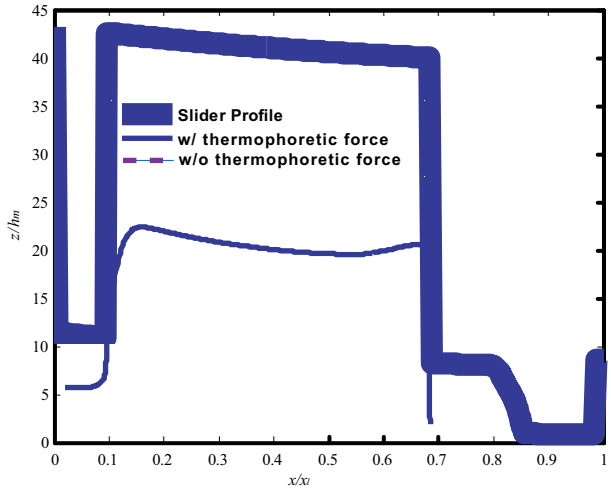

Figure 5.4: Typical particle's trajectories in the head-disk interface. The two trajectories superpose on each other. Here h_m is a nominal flying height used as a reference value to normalize z.

calculated: one with the thermophoretic force and the other one without it, the latter of which corresponds to a traditional slider without the heating element.

The profile of an air bearing surface, which is the surface of the slider facing the disk, is shown in Fig. 5.3 and is used in the following calculations. The numerical results presented in Fig. 5.4, show that these two trajectories essentially coincide with each other, which implies that the thermophoretic force is negligible even for this extreme case. To understand the reason behind this finding, we perform an order analysis and investigate the relative importance of the thermophoretic force and the Saffman force.

Since the slider's flying height at the leading edge is about 200nm and we are considering particles' motion in the HDI, only those particles with size below 200nm are of concern. Since $k_g/k_p \sim 0.024/30.9 \ll 1$ and $\mathrm{Kn} = \lambda/R > 0.3$, the k_g/k_p term can be neglected in Eq. (5.2), and Eq. (5.3) becomes

$$F_T \sim \frac{192\mu\nu}{(1+3.42\lambda/R)\,(1+4.36\lambda/R)} \frac{\alpha_3/\alpha_2}{\alpha_4 - 4(\alpha_3/\alpha_2)(z/h)} \tag{5.5}$$

From Refs. [Zhang and Bogy 1997a; Saffmann 1965], the Saffman force is

$$F_{Saffman} \sim 6.46\mu R^2 \Delta U \sqrt{G/\nu} \tag{5.6}$$

where G is the magnitude of the gradient of the non-uniform air flow and ΔU is the magnitude of the speed of the air flow relative to the center of the sphere.

From Eqs. (5.5) and (5.6), we obtain the ratio between the thermophoretic force and the Saffman force

$$\frac{F_T}{F_{Saffman}} \sim \frac{192}{6.46} \left(\frac{\nu}{U}\frac{h^{1/3}}{R^{4/3}}\right)^{3/2} \frac{1}{(1+3.42\lambda/R)\,(1+4.36\lambda/R)} \frac{\alpha_3/\alpha_2}{\alpha_4 - 4\alpha_3/\alpha_2} \tag{5.7}$$

where we take $z = h$ to get an estimation of the order of F_T, and we use U/h as an estimate of G, U as an estimate of ΔU and U is the disk's speed. Equation (5.7) further requires an estimation of α_2, α_3 and α_4, which involve $\beta = h/\lambda$ and $L = \sqrt{T_s/T_d} = \sqrt{1+l}$ where $l = (T_s - T_d)/T_d \ll 1$.

Due to the dependence of the mean free path on the local pressure, the mean free path decreases with the slider's flying height, which means $\beta \gg 1$ or $\beta \sim 1$. For either of these two cases, $\alpha_2 \sim 2$ and $\alpha_4 \sim 1 - (1+\beta)\alpha_3$, and

$$\begin{aligned}
\alpha_3 &= \frac{-\sqrt{(\beta+2)^2 + (1+\beta)\left[2l + l^2 + 2\left((1+l)^{3/2} - 1\right)\right]} + l + (1+l)^{3/2} + \beta + 1}{\beta - l} \\
&= \frac{-(\beta+2)\sqrt{1 + \frac{1+\beta}{(2+\beta)^2}\left[2l + l^2 + 2\left((1+l)^{3/2} - 1\right)\right] + \frac{l}{(2+\beta)^2}} + (1+l)^{3/2} - 1 + \beta + 2}{\beta - l} \\
&\sim \frac{-(\beta+2) - \frac{1+\beta}{2(2+\beta)}\left[2l + l^2 + 2\left((1+l)^{3/2} - 1\right)\right] - \frac{l}{2(2+\beta)} + \frac{3}{2}l + (\beta+2)}{\beta - l} \\
&\sim -\frac{\beta}{\beta+2} l
\end{aligned}$$

Then $\alpha_3/\alpha_2 \ll 1$ and $\alpha_3/(\alpha_2\alpha_4) \ll 1$. Given that the kinematic viscosity for air $\nu \sim 10^{-6}\mathrm{m}^2/\mathrm{s}$ and the disk speed $U \sim 10\mathrm{m/s}$, it can be shown from Eq. (5.7) that the thermophoretic force is always smaller than the Saffman force, and it is therefore negligible since the Saffman force itself is negligible for particles smaller than 200nm [Zhang and Bogy 1997a]. Thus we do not need to consider the thermophoretic force for calculation of a particle's trajectory in the HDI between a TFC slider and a disk, and, accordingly, for studies of particle contamination on a TFC slider Liu and Bogy [2010].

5.4 Summary and conclusion

The particle contamination on a thermal flying-height control (TFC) slider is investigated in this chapter. The temperature difference between the slider and the disk, due to local heating in the slider, induces a thermophoretic force on particles moving in the HDI. By incorporating results for the temperature field in the HDI based on the method of moments, we obtain an analytical formula for the thermophoretic force on the particles moving in the HDI. We then solve the governing equation for the particle's motion and obtain the particle's trajectory. It is found numerically that the effect of the thermophoretic force is negligible. This is further confirmed by an order analysis of the magnitude of the thermophoretic force and Saffman force. We show that the thermophoretic force is always smaller than the Saffman force and is therefore negligible since in our case they act along the same direction. The present study thus validates the use of the current CML particle contamination simulator for the investigation of particle contamination on a TFC slider.

Chapter 6

Temperature effect on a HDD slider's flying performance at steady state

6.1 Introduction

The temperature inside modern HDDs can rise to as high as 100°C. Since the temperature is related to the gas molecules' speed [Bird 1994], the temperature increase affects the motion of the air molecules in the HDI. Due to its dependence on the motion of the air molecules, the slider's flying performance is affected by the temperature change as well. This chapter focuses on two important issues of a HDD slider's flying performance at steady state: the slider's flying attitude and the shear forces on the slider and the disk. The slider's flying attitude, including the slider's flying height, pitch and roll angles, is related to the HDDs' capacity. A lower flying height and a more stable flying attitude of the slider is critical to the increase of the HDDs' capacity. The shear forces on the slider and the disk are related to the HDDs' reliability. The shear force on the lubricant has been shown to be the dominant factor determining the deformation and instability of the lubricant layer [Mate and Marchon 2000; Dai et al. 2003; Scarpulla et al. 2003; Dai et al. 2004; Marchon et al. 2005; Wu 2006a,b; Kubotera and Bogy 2007]. The deformation and instability serve as a mechanism for the transfer of the lubricant from the disk to the slider [Ma and Liu 2007], which increases the likelihood of the slider's impact on the disk and can result in wear of the disk as well as the loss of data stored on the disk.

Cha *et al.* [Cha et al. 1996] numerically solved the classical Reynolds equation for a slider with a minimum flying height around 60nm, and they qualitatively argued that an increase in temperature induced increases in both the mean free path λ and the air viscosity μ. The increases in λ and μ led to opposite effects on the slider's flying height and finally resulted in a small change in the slider's flying height. Their experiments confirmed this qualitative argument and showed that the flying height only changed by 1nm when the temperature increased by 20°C. Since the minimum flying height of the slider in the current HDDs is less than 10nm and is being reduced to less than 5nm, the classical Reynolds equation is no longer applicable, and a change of 1nm or so in the slider's flying height, if it exists, is no longer a negligible change. Zhang *et al.* [Zhang et al. 2008b] also studied the temperature effect on the slider's flying height when investigating the effect of humidity on the slider's flying performance at different temperatures. They, however, did not provide any details on how

they included the temperature effect into their simulations. Even less work has been done on the shear forces on the slider and the disk when compared to studies on the temperature effect on the slider's flying attitude. In the current ABS design program [Cox and Bogy 2007], the hard sphere model for air molecules is used to study the temperature effect on the slider's flying performance, and the analytical results based on the first order slip theory are used to calculate the shear forces on the slider and the disk. Since the hard sphere model can at most give qualitative results for the temperature dependence of air viscosity and the mean free path of air molecules, more refined models are needed. At the same time, the air gap thickness in the HDI is comparable or even less than the mean free path, and the first order slip theory does not hold in the entire HDI. Thus, a study of the temperature effect on the slider's flying performance and interface shear is needed.

In this chapter we modify the generalized Reynolds equation, which is derived from the linearized BGK-Boltzmann equation, by using a variable soft sphere (VSS) model for the air molecules to include a temperature effect on the mean free path and air viscosity. The formulae for the shear forces are also derived and serve as a basis for studying how temperature increase affects the shear forces on the slider and the disk. This chapter is organized as follows. The formulae for the shear forces on the slider and the disk are derived in Sec. 6.2. In Sec. 6.3, we review and modify the generalized Reynolds equation. Numerical results are presented and discussed in Sec. 6.4. Finally, a summary and conclusion is given in Sec. 6.5.

6.2 Shear forces on the slider and the disk

Fukui and Kaneko [Fukui and Kaneko 1988] showed that for the air flow in the HDI, a solution satisfying Eq. (1.4) and compatible with the boundary condition Eq. (1.5) can be expressed as

$$\phi = \frac{1}{p_0}\frac{\mathrm{d}p}{\mathrm{d}x}x + \frac{\xi_x}{\sqrt{2RT_0}}\phi_1(z, \xi_z, \xi_i\xi_i), \tag{6.1}$$

with ϕ_1 determined by

$$\frac{\lambda}{\sqrt{2RT_0}}\xi_z\frac{\partial\phi_1}{\partial z} = \frac{\sqrt{\pi}}{2}\left(-\phi_1 + 2\frac{U}{\sqrt{2RT_0}}\right) - \frac{\lambda}{p_0}\frac{\mathrm{d}p}{\mathrm{d}x}, \tag{6.2}$$

and

$$\begin{aligned}\phi_1|_{disk}^{\xi_2>0} &= (1-\alpha_{disk})\phi_1|_{disk}^{\xi_2<0} + 2\alpha_{disk}\frac{U}{\sqrt{2RT_0}},\\ \phi_1|_{slider}^{\xi_2<0} &= (1-\alpha_{slider})\phi_1|_{slider}^{\xi_2>0},\end{aligned} \tag{6.3}$$

where the x direction is parallel to the disk, the z direction is perpendicular to the disk, p is the local pressure, $\mathrm{d}p/\mathrm{d}x$ is the local pressure gradient, p_0 is the ambient pressure, T_0 is the ambient temperature, ξ_i is the molecule's velocity along the i direction, and U is the disk speed. From Eq. (6.1) and kinetic theory [Sone 2006], it can be shown that the shear force on the slider or the disk is a linear combination of contributions from the Couette and Poiseuille flow components.

Let us first consider the Poiseuille flow part. By setting the disk speed $U = 0$ in Eqs. (6.1), (6.2) and (6.3), we obtain a similarity solution for Poiseuille flow of a rarefied gas. Then, from the definition of the normal stress in kinetic theory [Sone 2006]

$$\begin{aligned}
\sigma_{xx} =& -p_0 - \frac{2}{\pi^{3/2}} \frac{p_0}{(2RT_0)^{5/2}} \int \xi_x^2 \phi \exp\left(-\frac{\xi_i \xi_i}{2RT_0}\right) d\boldsymbol{\xi} \\
=& -p_0 - \frac{2}{\pi^{3/2}} \frac{p_0}{(2RT_0)^{5/2}} \frac{1}{\rho_0 RT_0} \frac{\mathrm{d}p}{\mathrm{d}x} x \int_{-\infty}^{\infty}\int_{-\infty}^{\infty}\int_{-\infty}^{\infty} \xi_x^2 \exp\left(-\frac{\xi_x^2+\xi_y^2+\xi_z^2}{2RT_0}\right) d\xi_x d\xi_y d\xi_z \\
& - \frac{2}{\pi^{3/2}} \frac{p_0}{(2RT_0)^{5/2}} \frac{1}{\sqrt{2RT_0}} \int_{-\infty}^{\infty}\int_{-\infty}^{\infty}\int_{-\infty}^{\infty} \xi_x^3 \phi_1 \exp\left(-\frac{\xi_x^2+\xi_y^2+\xi_z^2}{2RT_0}\right) d\xi_x d\xi_y d\xi_z \\
=& -p_0 - \frac{\mathrm{d}p}{\mathrm{d}x} x
\end{aligned}$$

where the integral involving ϕ_1 vanishes since the limits of the integral for ξ_x are symmetric and the associated integrand is odd in ξ_x, the latter of which is further due to the oddness of ξ_x^3 and the fact that ϕ_1 is functions of y, ξ_y, ξ_x^2, ξ_y^2, ξ_z^2 but not ξ_x itself. For σ_{xy}, we have

$$\sigma_{xy} = \frac{2}{\pi^{3/2}} \frac{p_0}{(2RT_0)^{5/2}} \int \xi_x \xi_y \phi \exp\left(-\frac{\xi_i \xi_i}{2RT_0}\right) d\boldsymbol{\xi} \neq 0$$

To get σ_{xy}, we need to solve for the linearized Boltzmann equation for ϕ. However, since we are mainly interested in a macroscopic quantity, i.e. the shear force, detailed information on the velocity distribution function of the molecules moving between the slider and the disk is not of concern. So we can bypass the Boltzmann equation and instead work with the conservation equations. The conservation equations can be derived directly from the basic principle of the conservation of mass, momentum and energy, and they apply to any kind of air flow rarefied or not [Sone 2006]. These equations are not closed since they involve several unknown quantities such as the stress tensor, which needs to be determined through other means. From another point of view, these conservation equations are the first three moments of the Boltzmann equation with respect to the molecular velocity. According to the theory of partial differential equation, a partial differential equation is equivalent to a full set of all its moment equations, and, for the Boltzmann equation, these moment equations form the so called BBGKY hierarchy. Since the conservation equations are the first three components of the BBGKY hierarchy, they are not fully equivalent to the Boltzmann equation and they are not closed. The Euler equation and the Navier-Stokes equation are two special cases of the conservation equations where the stress tensor is related to the air flow velocity gradient through a constitutive relation.

Since Fukui and Kaneko [Fukui and Kaneko 1988] have shown that the air flow in the HDI is isothermal, we only need to deal here with the conservation equations of mass and momentum to get the shear force [Sone 2006]. Under the same assumptions as used by Fukui and Kaneko [Fukui and Kaneko 1988], i.e., the thickness of the air gap in the HDI is much less than the length and the width of the slider, and the air flow in the direction perpendicular to the disk is negligible, the conservation equations for a steady flow reduce

to

$$\frac{\partial}{\partial x}\left(\rho v_x\right) = 0 \tag{6.4}$$

$$\frac{\partial}{\partial x}\left(\rho v_x^2 + \sigma_{xx}\right) + \frac{\partial}{\partial z}\left(\sigma_{xz}\right) = 0 \tag{6.5}$$

where σ_{xx} and σ_{xy} are components of the stress tensor. Again, we note that Eqs. (6.4) and (6.5) are not closed due to the appearance of σ_{xy} and σ_{xx} which can only be determined by some kind of constitutive relations. We next investigate the order of each term in Eq. (6.5) and show that all the terms in Eq. (6.5) are not of the same order. Through this approach, Eq. (6.5) can be further reduced.

In the HDI, the dimensionless pressure gradient $L/p_0 \mathrm{d}p/\mathrm{d}x \ll 1$ where L is the slider's length, and all quantities can be expanded as Taylor series of this dimensionless pressure gradient. The first term in this Taylor series of each quantity is called the order of this quantity in terms of the dimensionless pressure gradient. We find that the flow velocity v_x and density gradient $\partial\rho/\partial x$ are both of the first order. Then, the first term in Eq. (6.5), $\partial(\rho v_x^2)/\partial x$, after using Eq. (6.4) to eliminate $\partial v_x/\partial x$, turns out to be $-v_x^2\partial\rho/\partial x$, which is of second order of $L/p_0 \mathrm{d}p/\mathrm{d}x \ll 1$. From the above discussion, σ_{xx} and σ_{xz} are both nonzero in the framework of the linearized Boltzmann equation, and they should be both of the first order. Thus the first therm is therefore negligible since the other terms in Eq. (6.5) are of first order. So Eq. (6.5) finally reduces to

$$-\frac{\mathrm{d}p}{\mathrm{d}x} + \frac{\partial \sigma_{xz}}{\partial z} = 0 \tag{6.6}$$

Since the accommodation coefficients of engineering surfaces are close to each other, we here assume the accommodation coefficients of the slider and the disk are the same. Then, the Poiseuille flow is symmetric with respect to the centerline $z = 0$ in our coordinate system. Under these conditions, the shear forces on the two boundaries are equal to each other, i.e. $\sigma_{xz}n_z|_{z=-h/2} = \sigma_{xz}n_z|_{z=h/2}$, and the normal directions of the two boundaries are opposite to each other, i.e. $n_z|_{z=-h/2} = -n_z|_{z=h/2}$. Thus, $\sigma_{xz}|_{z=-h/2} = -\sigma_{xz}|_{z=h/2}$. Then, integrating Eq. (6.6) from $z = -h/2$ to $z = h/2$, we get

$$\sigma_{xz}|_{z=h/2} = \frac{h}{2}\frac{\mathrm{d}p}{\mathrm{d}x} \tag{6.7}$$

Next, let us consider the Couette flow part. For plane Couette flow existing between two plates separated by h and with the lower plate fixed and the upper one moving at speed U, Sherman's interpolation formula can be used [Sherman 1963]. This formula is based on an interpolation scheme between two limits: continuum flow and free molecular flow, and it has been shown to be consistent with experiments. For plane Couette flow of a continuum fluid, the shear force on the lower plate is

$$F_{con} = \mu\frac{U}{h}, \tag{6.8}$$

while for plane Couette flow of a free molecular gas for which the gas is so rarefied that the collisions between any two molecules are negligible, the shear force on the lower plate

is [Vincenti and Kruger 1965]

$$F_{fm} = \frac{1}{2}\rho U\sqrt{\frac{2kT}{\pi m}}. \tag{6.9}$$

where μ is the dynamic viscosity, m is the mass of the air molecule, and k is the Boltzmann constant. Then according to Sherman's formula, the shear force on the lower plate in plane Couette flow of an arbitrarily rarefied gas is

$$\begin{aligned} F_c =& F_{fm}\left\{1+\frac{F_{fm}}{F_{con}}\right\}^{-1} \\ =& \frac{1}{2}\rho U\sqrt{\frac{2kT}{\pi m}}\frac{\mu}{\mu+\frac{1}{2}\rho h\sqrt{\frac{2kT}{\pi m}}}. \end{aligned} \tag{6.10}$$

Equation (6.9) is obtained by modeling the molecules as hard spheres. In view of the relationship $\mu = \rho\lambda\sqrt{2kT/(\pi m)}$ obtained from assuming the molecules as hard spheres, we can write Eq. (6.10) as

$$F_c = \mu\frac{U}{2\lambda+h} \tag{6.11}$$

Then the total shear forces on the disk and the slider are [Fukui and Yamane 2002; Liu and Bogy 2009c]

$$\tau_w|_{disk} = -\mu\frac{U}{2\lambda+h} - \frac{h}{2}\frac{\mathrm{d}p}{\mathrm{d}x} \tag{6.12}$$

$$\tau_w|_{slider} = \mu\frac{U}{2\lambda+h} - \frac{h}{2}\frac{\mathrm{d}p}{\mathrm{d}x} \tag{6.13}$$

Before we can use these two formulae to calculate the shear forces, we need to know the pressure field and the viscosity. The first one, i.e., the pressure field, can be obtained from the generalized Reynolds equation while the second one can be modeled using the variable soft sphere (VSS) model for air molecules.

6.3 The generalized Reynolds equation and the variable soft sphere (VSS) model

6.3.1 The generalized Reynolds equation

The classical Reynolds equation [Reynolds 1886], which is derived from continuum theory, does not apply to air flow in the entire HDI [Burgdorfer 1959; Hsia and Domoto 1983; Mitsuya 1993], so the Boltzmann equation or its equivalent is needed. Under the same assumptions as in the classical Reynolds equation, i.e., the thickness of the air gap in the HDI is much less than the length and the width of the slider, and the air flow in the direction perpendicular to the disk is negligible, Fukui and Kaneko [Fukui and Kaneko 1987, 1988, 1990] started with the linearized Boltzmann equation, Eq. (1.4), and derived a generalized Reynolds equation for a steady flow in the HDI [Kang et al. 1999; Chen and Bogy 2005]:

$$\frac{\partial}{\partial X}\left(Q_p PH^3\frac{\partial P}{\partial X}\right) + \frac{\partial}{\partial Y}\left(Q_p PH^3\frac{\partial P}{\partial Y}\right) = \Lambda_b\frac{\partial PH}{\partial X}, \tag{6.14}$$

where $X = x/L$, $Y = y/L$, $P = p/p_0$ is the nondimensinal pressure, p is the air pressure, p_0 is the ambient pressure, $H = h/h_0$ is the nondimensinal air gap thickness, h is the air gap thickness, h_0 is the minimum air gap thickness, Q_p is the nondimensional mass flow rate of the Poiseuille flow component, $\Lambda_b = 6\mu UL/(p_0 h_0^2)$ is the bearing number, μ is the air viscosity at the ambient state, and U is the disk speed.

The solution of Eq. (6.14) relies on two parameters: the bearing number Λ_b and the nondimensional mass flow rate Q_p. The bearing number depends on the air viscosity while the mass flow rate $Q_p = Q_p(D, \alpha)$ is a function of the accommodation coefficient α and the inverse Knudsen number $D = \sqrt{\pi}h/(2\lambda)$ where λ is the mean free path. Since both λ and μ are functions of temperature, the change in temperature affects the solution of the generalized Reynolds equation as well.

6.3.2 The variable soft sphere (VSS) Model

To investigate the dependence of the slider's flying performance on the temperature, we need the formulae for the mean free path and the air viscosity as functions of temperature. These two formulae depend on the models used for the air molecules. The simplest one is the hard sphere model, which regards the air molecules as rigid spheres with interaction between each other happening only at collision. One of the important quantities for collision is the angle χ [Bird 1994], as shown in Fig. 6.1.

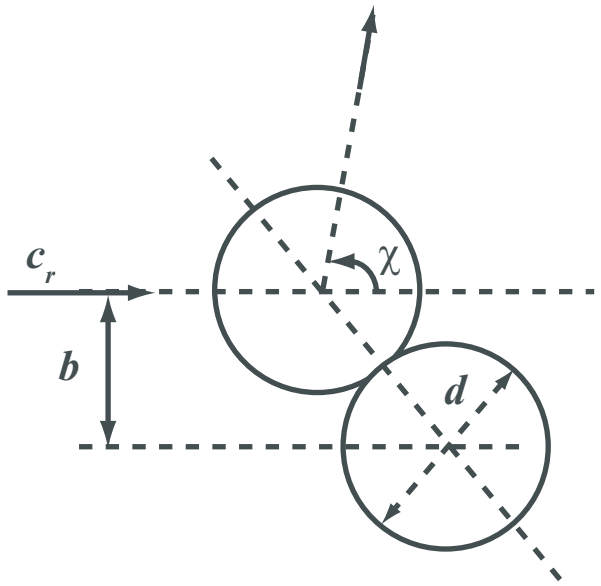

Figure 6.1: Collision between two air molecules with relative speed c_r. Here b is the projected distance, χ is the angle after collision, and d is the diameter of air molecules.

For the hard sphere (HS) model, $\chi = 2\cos^{-1}(b/d)$ where d is the diameter of air molecules and b is the projected distance. However, some macroscopic quantities calculated via the HS model, such as viscosity, can at most qualitatively agree with experimental results. The variable soft sphere (VSS) model [Koura and Matsumoto 1991, 1992] serves to improve the

deficiency in the HS model while keeping its simplicity. It is an empirical model with an empirical relation for d and χ with parameters determined by fitting the experimental results. In the VSS model, $d = d_{ref}(c_{r,ref}/c_r)^{\upsilon}$ and $\chi = 2\cos^{-1}[(b/d)^{1/\eta}]$ where c_r is the pre-collision relative speed between two pre-collision molecules, υ and η are two parameters used to fit experimental results, and the quantities with a subscript *ref* correspond to their values at a reference state. It can be shown that the mean free path for VSS molecules is [Bird 1994]

$$\lambda = \frac{kT_{ref}}{\sqrt{2}\pi d_{ref}^2 p}\left(\frac{T}{T_{ref}}\right)^{\omega+0.5}, \tag{6.15}$$

while the viscosity is

$$\begin{aligned}\mu =& \frac{5(\alpha+1)(\alpha+2)\sqrt{\pi m k}(4k/m)^{\upsilon}T^{\upsilon+0.5}}{16\alpha\Gamma(4-\upsilon)\sigma_{ref}c_{r,ref}^{2\upsilon}} \\ =& \mu_{ref}\left(\frac{T}{T_{ref}}\right)^{\omega}\end{aligned} \tag{6.16}$$

where k is the Boltzmann constant, $\omega = \upsilon + 1/2$, p is the air pressure, T is the temperature, σ is the collision cross section, and the quantities with a subscript *ref* correspond to their values at a reference state.

6.4 Results and discussion

Equations (6.14)–(6.16) involve several reference quantities. Here we choose the following reference values [Bird 1994; Lide 2008]:

$$\begin{aligned} T_{ref} = 0°\text{C}, \quad \mu_{ref} = 1.81\times10^{-5}\text{Ns/m}^2, \quad\quad d_{ref} = 4.13\times10^{-10}\text{m} \\ m = 5.6\times10^{-26}\text{kg}, \quad p_0 = 1.013\times10^{5}\text{N/m}^2 \end{aligned}$$

The finite volume method (FVM) [Lu 1997] is used to solve the modified generalized Reynolds equation, Eq. (6.14), and it gives the pressure field in the HDI. The shear forces on the slider and the disk are then calculated with Eqs. (6.12) and (6.13). Two designs of the air bearing surface (ABS), which is the surface of the slider facing the disk, are considered, and they are shown in Fig. 6.2. These two sliders are both Femto sliders (with length $L = 0.85$mm and width $b = 0.7$mm).

Figure 6.3 shows the change of the slider's flying height at the read-write element with temperature for the two ABS designs. When flying over the inner track, slider A has a flying height of 7.47nm at 25°C, and it decreases to 6.02nm when the temperature increases to 95°C. When flying over the other two tracks, slider A has a higher flying height and the increase in temperature leads to a smaller change in the slider's flying height. Similar trends occur for slider B. When slider B flies over the inner track, its flying height at the read-write element decreases from 5.59nm to 4.08nm when the temperature increases from 25°C to 100°C. Compared to slider A, slider B has a lower flying height, and the temperature increase has more effect on slider B. When both sliders fly at a height less than 10nm, the temperature change induces a non-negligible change in the slider's flying height, and the lower the slider's flying height, the more the flying height decreases with the temperature.

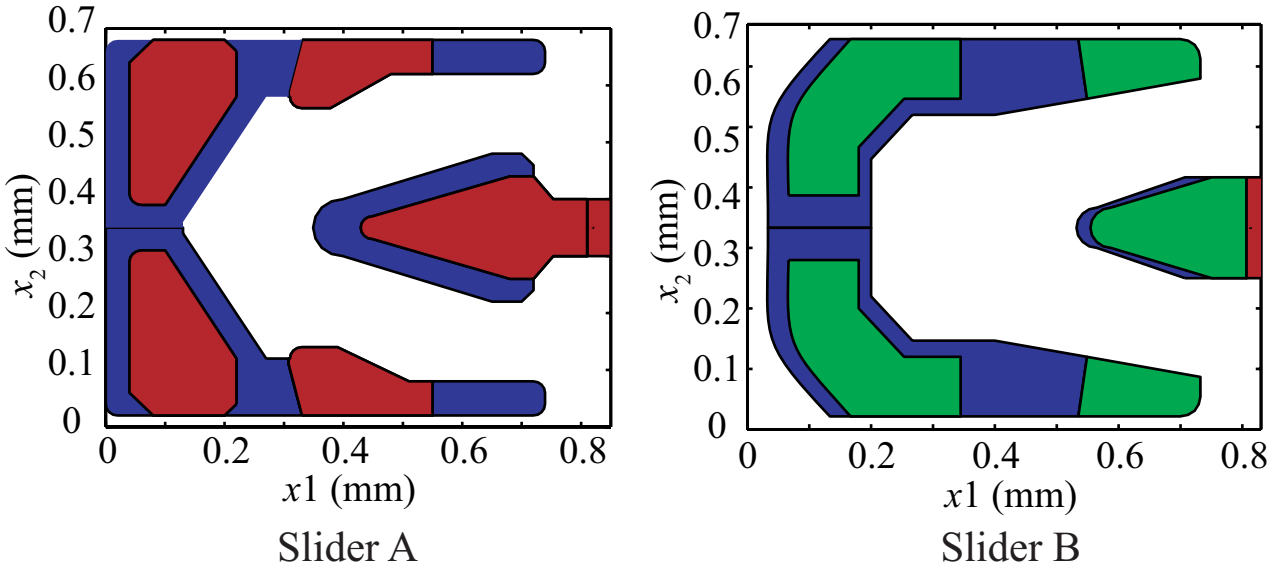

Figure 6.2: Air bearing surface (ABS) of slider A and slider B. Both sliders are Femto sliders (with length $l = 0.85$mm and width $b = 0.7$mm). Different colors correspond to difference etching depths.

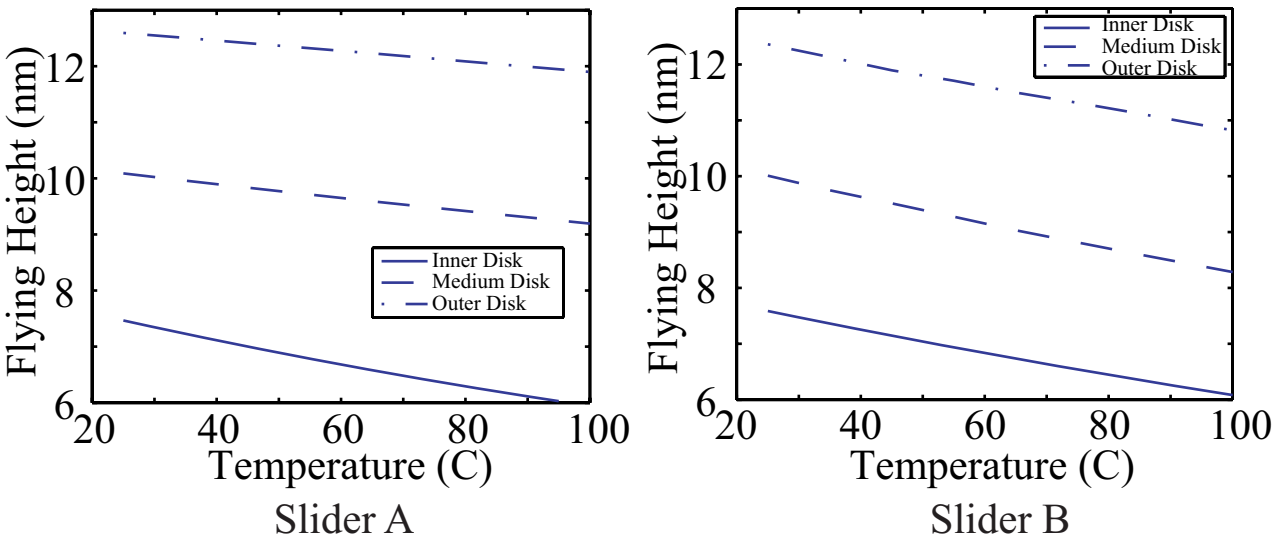

Figure 6.3: Change of the slider's flying height (FH) with temperature for the slider flying at the inner track, middle track or the outer track.

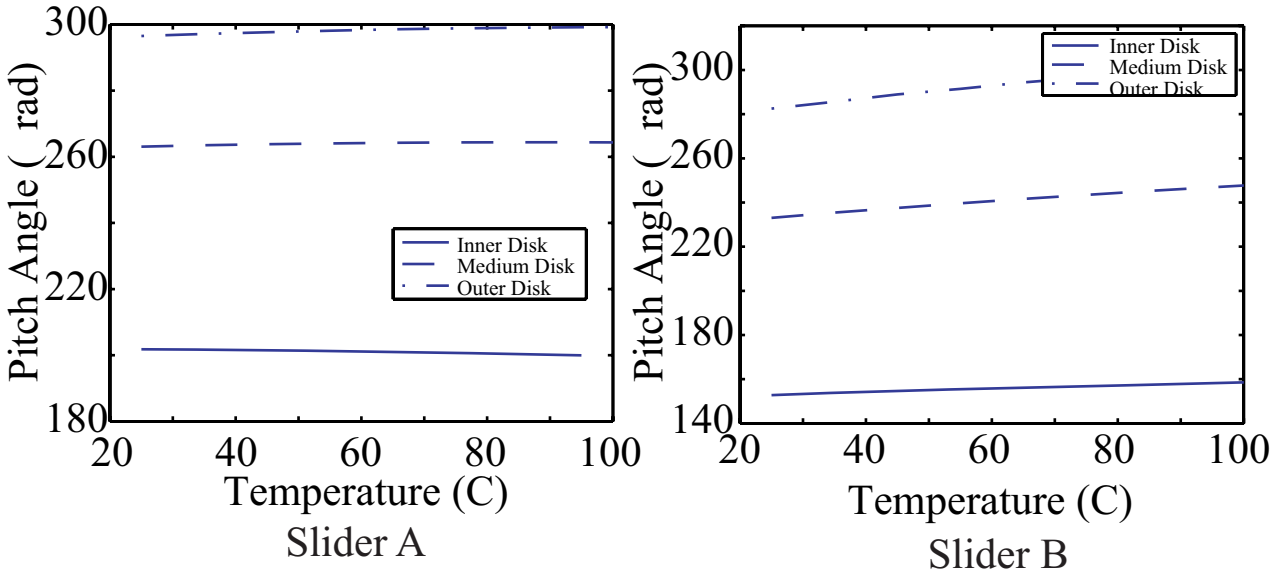

Figure 6.4: Change of pitch angle with the temperature.

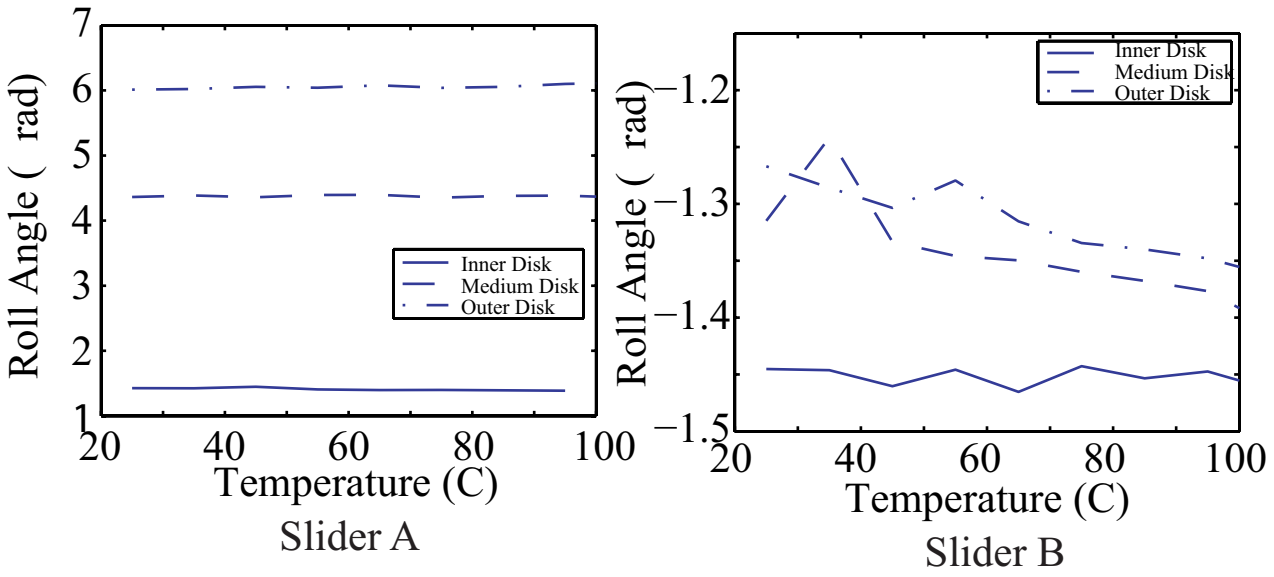

Figure 6.5: Change of roll angle with the temperature.

As shown in Eq. (6.14), the slider's flying attitude is mainly determined by two parameters: the mean free path, λ, which appears in the calculation of mass flow rate of the Poiseuille flow component Q_p, and the air viscosity at the ambient state, μ, which appears in the definition of the bearing number Λ_b. These two parameters increase with temperature, and they result in different changes in the slider's flying height: an increase in λ decreases the slider's flying height while an increase in μ increases the slider's flying height [Cha et al. 1996]. The final trend of the change of the flying attitude with temperature is a net result of these two effects. For the two ABS designs studied in this paper, the slider's flying height decreases with temperature as shown in Fig. 6.3. The changes of the other two quantities of the slider's flying attitude, i.e., the slider's pitch and roll angles, are shown in Figs. 6.4 and 6.5. Since the pitch angle depends on a balance of the moments of the pressures on the front and rear parts of the sliders' surface, the decrease in the slider's flying height with temperature leads to different changes of the pressures on the front and the rear parts of the ABS, which results in the final increase of the sliders' pitch angle with temperature, as shown in Fig. 6.4. As for the roll angle, it is determined by a balance of the moments of the pressures on the left and right sides of the slider's surface. Since the ABS's of the two sliders are symmetric with respect to the centerline, the changes of the pressure with temperature are also symmetric about the centerline and thus do not lead to noticeable changes of the roll angle. Although, for both slider A and slider B, the slider's flying height decreases with temperature it is not guaranteed that this trend holds for all sliders, and opposite trends might exist for some other sliders. When comparing the results of slider A and slider B, we find that the effect of the temperature on the slider's flying attitude also depends on the ABS designs. Thus it might be possible to design a specific ABS pattern to reduce the dependence of the slider's flying height on the temperature.

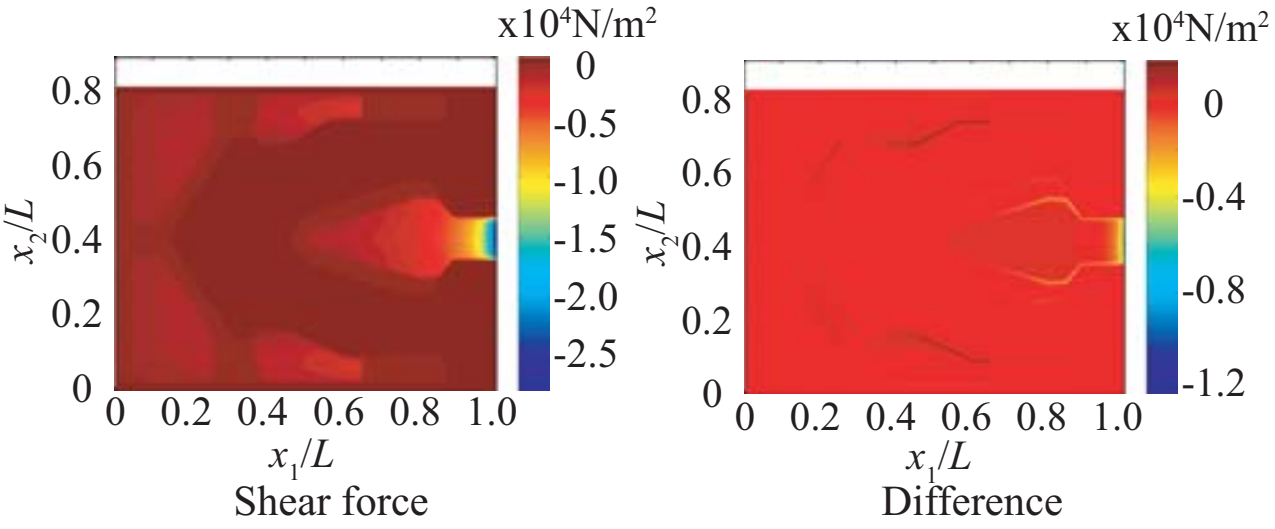

Figure 6.6: Shear force due to the Couette flow component in the head disk interface for slider A. (a) the shear force at $T = 25°$C. (b) The difference of the shear force at $T = 25°$C from that at $T = 100°$C

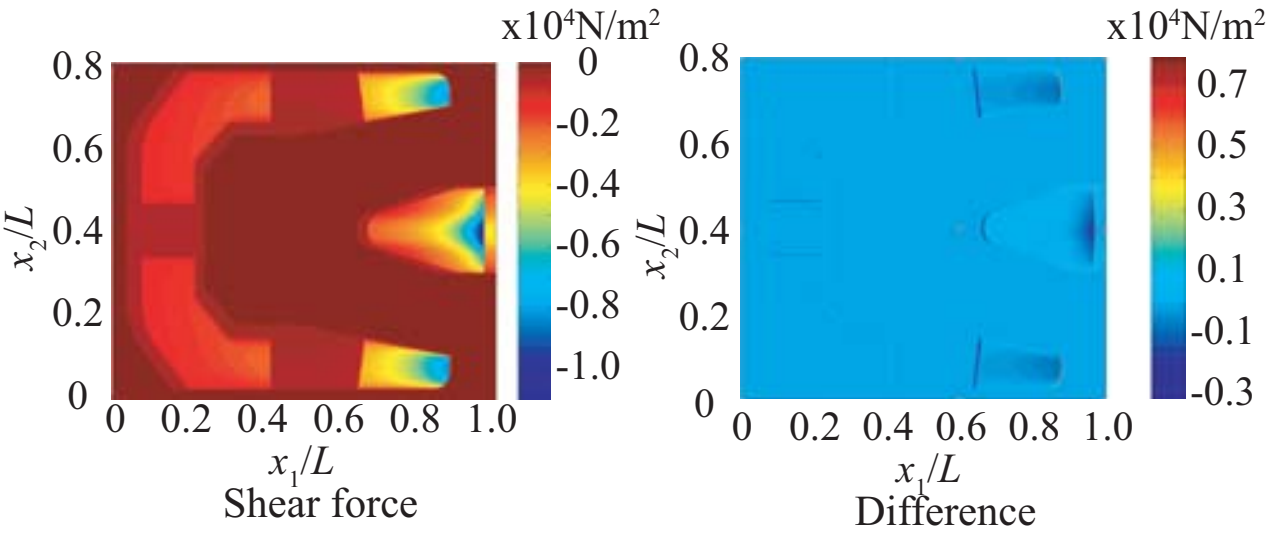

Figure 6.7: Shear force due to the Couette flow component in the head disk interface for slider B. (a) the shear force at $T = 25°$C. (b) The difference of the shear force at $T = 25°$C from that at $T = 100°$C. Note that the zero value in this figure corresponds to a different color from that in Fig. 6.6.

The shear forces on the slider and the disk are linear combinations of contributions of the Couette and Poiseuille flow components. Since the present problem has a large bearing number which is an indication of the importance of the Couette flow component compared to the Poiseuille flow component, the Couette flow component dominates the air flow. Thus only the shear forces due to the Couette flow components are presented in Figs. 6.6 and 6.7. For most regions on the ABS, the effect of temperature increase on the shear force is negligible. The noticeable effect of the temperature increase on the shear force appears at the region near the read-write element, which is a combined effect of the decrease in the slider's flying height and the increase in the slider's pitch angle induced by the temperature increase. Since the slider's flying height and its stability at the read-write element determine the HDDs' capacity, changes of the shear force beneath the read-write element could result in changes in the deformation and instability of the lubricant, which may increase the possibility of the slider's contact onto the disk and affect the reliability of the HDDs.

6.5 Summary and conclusion

An approach to studying the effect of temperature change on a HDD slider's flying attitude and the shear forces on the slider and the disk is presented in this chapter. Based on the linearized Boltzmann equation and a similarity solution proposed by Fukui and Kaneko, we show that the shear forces are linear combinations of the contributions from the Couette and Poiseuille flow components. The former contribution is calculated through Sherman's formula, which interpolates the results for continuum flow and free molecular flow and generates a general formula applicable for an arbitrarily rarefied gas. The latter contribution is

calculated through a formula derived from the conservation equations. These two formulae depend on the pressure gradient and the mean free path. The generalized Reynolds equation, proposed by Fukui and Kaneko and used to solve for the air flow field in the head disk interface, is then modified to include the temperature effect on the mean free path and the air viscosity. These modifications are based on the variable soft sphere model, which is an empirical model that gives results agreeing well with experiments. The modified generalized Reynolds equation is solved using a finite volume method, and the shear forces are calculated afterwards. Numerical results are obtained for two slider designs, and the results show that the temperature change induces non-negligible changes in the slider's flying height as well as the shear force. Since these non-negligible changes are dependent on the ABS designs, it may be possible to design some specific ABS patterns to reduce the dependence of the shear force and the slider's flying height on the temperature.

Chapter 7

Numerical prediction of a TFC slider's flying performance

7.1 Introduction

Thermal flying-height control sliders have been recently introduced into the HDD industry as an approach to increase the HDDs' capacity and reliability. Their complex structure of the heater element and transducer near the trailing edge, as shown in Fig. 1.6, prohibits analytical studies, so a numerical approach has been widely used to predict a TFC slider's flying performance, which assists in the designs of this kind of sliders.

Juang, Chen and Bogy [Juang et al. 2006], and Juang and Bogy [Juang and Bogy 2007], proposed an iterative numerical approach, which has now become standard, to calculate the TFC slider's deformation at a given heater power. This approach iterates between two steps: in the first step, the air flow field and the air pressure inside the HDI are obtained by solving the generalized Reynolds equation Eq. (6.14) for the particular ABS design and operating parameters; in the second step, the finite element method is used to calculate the slider's deformation induced by the power applied to the heater element with the heat flux and the air pressure on the ABS being boundary conditions. Juang and Bogy [Juang et al. 2006] originally neglected the slider's deformation induced by the air pressure on the ABS. This effect was later considered by Juang et al. [Juang et al. 2008] and numerical results for the thermally actuated flying-height as a function of the heater power agrees well with experiments, as presented in Ref. [Juang et al. 2008].

Based on the iterative approach, Zhang et al. [Zhang et al. 2008a] studied how the ABS designs affect the TFC slider's performances, such as flying attitude, and found several general guidelines to improve them: reducing the air bearing pressure, reducing the size of the thermo-mechanical actuation area, and decoupling the peak air bearing pressure area from the thermo-mechanical actuation area. Li *et al.* [Li et al. 2009] later studied how to design the thermal insulator to improve the TFC sliders' efficiency. They found that reducing the insulator's thermal conductivity and increasing its thickness are helpful. Aoki and Watanabe [Aoki and Watanabe 2009] numerically and experimentally studied how the power applied to the heater element affects the distance between the transducer and the disk. They found that the relationship between them is nonlinear and the distance is mainly affected by the slider's thermal protrusion.

The heat flux on the ABS serves as a boundary condition determining the temperature field inside the slider, which determines the slider's protrusion and deformation. Thus, accurate calculation of heat flux is critical to successfully predicting of TFC sliders' flying performance. The first model to calculate the heat flux was proposed by Zhang and Bogy [Zhang and Bogy 1999], who solved the Navier-Stokes equation with the velocity and temperature jump boundary conditions and obtained an analytical formula. This model was further improved by Chen, Suk and Bogy [Chen et al. 2000] to include the work done by pressure gradient. Zhang and Bogy [Zhang and Bogy 1999] and Chen, Suk and Bogy [Chen et al. 2000] found that heat conduction dominates the heat flux on the slider when the slider's temperature is different from the disk's. Their formula for the heat conduction is now widely used in practical simulation of the protrusion of thermally actuated sliders, and simulation based on this formula compares well with experimental results. However, since both of theses two works are based upon the continuum theory, it is not guaranteed that these formulae are applicable for an arbitrarily rarefied gas. To check their applicability, Ju [Ju 2000] used the direct simulation Monte Carlo (DSMC) method to numerically analyze the heat conduction and viscous dissipation due to the Couette flow part of the gas flow in the HDI. His results showed that heat conduction predicted by Zhang and Bogy's model, to a good degree, agrees with numerical results and that viscous dissipation due to the Couette flow part can be calculated by an empirical formula. Since the heat flux on the slider also has other contributions than those discussed by Ju. Shen and Chen [Shen and Chen 2008] started with a linearized BGK-Boltzmann equation to analyze this problem. They showed that the total heat flux can be divided into two parts: heat conduction and viscous dissipation due to Couette and Poiseuille flows. Their results are, however, not fully consisted with the classical results based on the linearized Boltzmann equation which, as shown later in this chapter, is not sufficient to characterize the heat transfer in the HDI. Thus, a refined model for heat flux is thus needed and the accuracy of the currently used model to predict TFC sliders' flying performance needs to be clarified.

In this chapter, we separately analyze the heat conduction and viscous dissipation using different approaches. For the heat conduction, we extend the classical definition of the mean free path by including the effects of the presence of the boundaries, i.e., the slider and the disk. Our results agree better with the numerical ones based on the linearized Boltzmann equation. For the viscous dissipation, we adopt a different approach from previous researchers. Here, we instead work with the conservation equations derived from the Boltzmann equation and use the intrinsic symmetry of the Couette and Poiseuille flows, which permits us to simplify the conservation equations and obtain analytical formulae for viscous dissipation in both flows. This approach bypasses the complexity involved in solving the full Boltzmann equation.

This chapter is organized as follows. Section 7.2 investigates the heat conduction between a slider and a disk at different temperatures. Section 7.3 investigates the viscous dissipation due to the Couette flow part and the Poiseuille flow part, whose importance is compared to the heat conduction part in Sec. 7.4. Section 7.5 investigates the accuracy of the currently used model for predicting a TFC slider's flying performance by comparing the predictions based on the currently used heat flux model and that based on the new model proposed here.

7.2 Heat conduction between a slider and a disk

The first attempt to get a conduction heat flux model was to solve the energy equation with the temperature jump boundary condition [Zhang and Bogy 1999; Chen et al. 2000; Ju 2000]. This boundary condition states that the temperature difference between the gas next to the boundary and the boundary is proportional to the local temperature gradient. Through this approach, Zhang and Bogy [Zhang and Bogy 1999] and Chen and Suk and Bogy [Chen et al. 2000], among others, showed that the conduction heat flux at the bearing surface is,

$$q = -k\frac{T_s - T_d}{h + 2\frac{2-\sigma_T}{\sigma_T}\frac{2\gamma}{\gamma+1}\frac{1}{\mathrm{Pr}}\lambda} \tag{7.1}$$

where k is the thermal conductivity of the air, T_s is the slider's temperature, T_d is the disk's temperature, h is the local flying height of the slider, σ_T is the thermal accommodation coefficient, γ is the heat capacity ratio of the air, λ is the local mean free path of the air, $\mathrm{Pr} = \nu/\alpha_T$ is the Prandtl number of the air, ν is kinetic viscosity of the air, and α_T is thermal diffusivity of the air.

The mean free path appearing in Eq. (7.1) is usually calculated from the classical definition which states that the mean free path is the average distance traveled by gas molecules between two collisions at the equilibrium state where the gas molecules are assumed to move freely in the whole space without any boundaries. This condition, however, is not satisfied in the present case where the slider and the disk will constraint the motion of gas molecules moving in between [Peng et al. 2004]. Thus, the classical definition of the mean free path needs to be modified here to take into account of the effects of the presence of the two boundary plates.

The modified mean free path is calculated here in two steps. In the first step, we calculate the distance one molecule can travel when moving between two plates, and, in the second step, the modified mean free path is taken as the average value of the distance each molecule can travel in the gas film. According to its definition, the mean free path is the *average* distance a molecule can travel between two collisions. To make our derivation easier to understand, we assume that only when $d < \lambda$, where d is the distance of the molecule from the boundary along the molecule's velocity direction as shown in Fig. 7.1, is the distance the molecules can move freely different from λ. As in the derivation of the classical mean free path, we further assume the gas molecules are isotropic in the velocity space. Then, as shown in Fig. 7.1, only when the angle θ between the molecular velocity and the normal of the boundary is less than $\arccos(d/\lambda)$, is the distance the molecule can travel freely different from λ and turns out to be $d/\cos\theta$. The probability of the molecule's collision with the boundary at an angle θ and in a solid angle $\mathrm{d}\omega = \sin\theta \mathrm{d}\theta\mathrm{d}\phi$ is $(\sin\theta\mathrm{d}\theta)/2$, where ϕ is the azimuthal angle. Based on this, the average distance a molecule moving near a boundary can travel when $d < \lambda$ is,

$$\lambda_1 = \int_0^{\arccos(d/\lambda)} \frac{d}{\cos\theta}\frac{\sin\theta}{2}\mathrm{d}\theta + \int_{\arccos(d/\lambda)}^{\pi} \lambda\frac{\sin\theta}{2}\mathrm{d}\theta = \frac{\lambda}{2}\left[1 + \frac{d}{\lambda} - \frac{d}{\lambda}\ln\left(\frac{d}{\lambda}\right)\right] \tag{7.2}$$

Similarly, the average distance a molecule can travel between two boundaries when $h - d < \lambda$

and $d < \lambda$ as shown in Fig. 7.1 is

$$\begin{aligned}\lambda_2 =& \int_0^{\arccos(d/\lambda)} \frac{d}{\cos\theta}\frac{\sin\theta}{2}\mathrm{d}\theta + \int_{\arccos(d/\lambda)}^{\arccos((h-d)/\lambda)} \lambda\frac{\sin\theta}{2}\mathrm{d}\theta + \int_{\arccos((h-d)/\lambda)}^{\pi} \frac{h-d}{\cos\theta}\frac{\sin\theta}{2}\mathrm{d}\theta \\ =& \frac{\lambda}{2}\left[\frac{h}{\lambda} - \frac{d}{\lambda}\ln\left(\frac{d}{\lambda}\right) - \frac{h-d}{\lambda}\ln\left(\frac{h-d}{\lambda}\right)\right] \end{aligned} \tag{7.3}$$

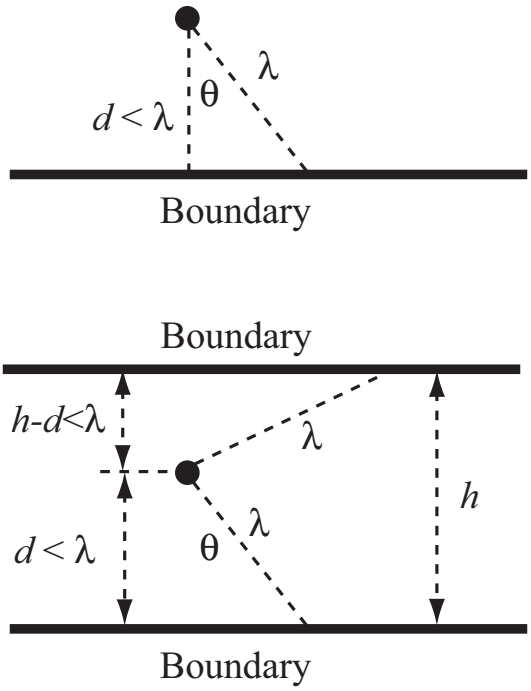

Figure 7.1: One molecule moves close to one boundary (a) and two boundaries (b).

In view of the above, we can average among all of the molecules moving between two boundary plates to get the modified mean free path. Since each molecule moves at a different distance from one of the boundaries, they do not feel the effect of the boundaries at the same level. Some of them are affected by only one boundary if they satisfy $(d-\lambda)(h-d-\lambda) < 0$, some of them are affected by two boundaries if they satisfy $d < \lambda$ and $h - d < \lambda$, and the others are not affected by any boundary. Here we assume that the gas molecules are uniformly distributed between two boundaries. After some algebra, we get the modified mean free path of the gas molecules moving between two boundary plates as,

$$\lambda_m = \begin{cases} \lambda\left(1 - \frac{1}{4}\frac{\lambda}{h}\right), & h \geq \lambda \\ \lambda\left(\frac{3}{4}\frac{h}{\lambda} - \frac{h}{2\lambda}\ln\left(\frac{h}{\lambda}\right)\right), & h < \lambda \end{cases} \tag{7.4}$$

Replacing the original mean free path with the modified mean free path Eq. (7.4) in Eq. (7.1), we obtain a new model to calculate heat conduction between the slider and the disk. Since this new gas film heat conduction model is still based on the temperature jump theory, it is not guaranteed to be applicable when the Kundsen number is high. Figure 7.2 compares

predictions based on the original and the new models with results obtained from numerically solving the linearized Boltzmann equation [Bassanini et al. 1968]. The results based on the new model (solid lines) agree well with numerical results from the linearized Boltzmann equation, while results based on the original definition of the mean free path [Zhang and Bogy 1999] overpredict the heat flux, especially for the inverse Knudsen number $D < 1$ where $D = \sqrt{\pi}h/(2\lambda)$.

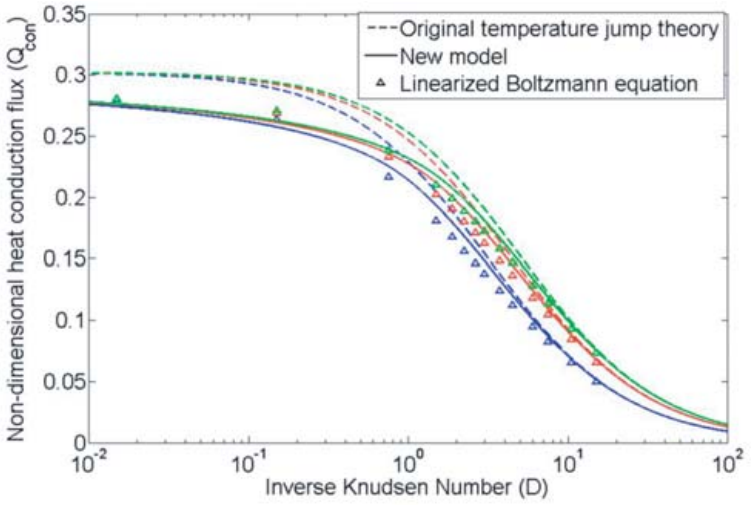

Figure 7.2: Heat conduction predicted by the original model, the new model with the modified mean free path and numerical results from the linearized Boltzmann equation. The non-dimensional heat flux $Q = q/[\rho_0\sqrt{2RT_0}(T_s - T_d)/T_0]$

7.3 Viscous heating

Similar to other problems in rarefied gas dynamics, the exact approach to address viscous heating is to solve the Boltzmann equation, which, as discussed in Sec. 1.3, is very complex and difficult to solve. Given the disk's relatively small speed, the linearized Boltzmann equation is sufficient to describe the gas flow in the HDI, and it has also been used to study viscous heating in the HDI [Shen and Chen 2008].

In the approach of the linearized Boltzmann equation, the molecular velocity distribution function f is expanded on the basis of the Maxwellian distribution function f_0 as $f = f_0(1+\phi)$ as discussed in Sec. 1.3, and the non-dimensional heat flux Q_z is calculated through

$$Q_z = \int\int\int \xi_z(\zeta_x^2 + \zeta_y^2 + \zeta_z^2)\phi\pi^{-3/2}\exp(-\zeta_x^2 - \zeta_y^2 - \zeta_z^2)\mathrm{d}\zeta_x\mathrm{d}\zeta_y\mathrm{d}\zeta_z - \frac{5}{2}U_z \qquad (7.5)$$

where $\zeta_i = \xi_i/\sqrt{2RT_0}$ is the dimensionless molecular velocity and U_z is the dimensionless macroscopic velocity. In kinetic analyses of molecular gas lubrication, it is generally agreed that the flow velocity in the film thickness direction is negligibly small [Fukui and Kaneko 1988; Shen and Chen 2008], resulting in $U_z = 0$. Based on Sone's similarity solution [Sone

2006], it can be shown that the first term in Eq. (7.5) vanishes as well. Hence, the heat transfer flux $Q_z = 0$ for molecular gas lubrication between two boundary plates at the same temperature, which means that the linearized BGK-Boltzmann equation gives a zero heat flux perpendicular to the boundary when viscous heating is considered. The same conclusion is arrived at when the linearized Boltzmann equation with the hard-sphere molecular model is solved [Sone 2006]. The results obtained from the linearized Boltzmann equation are thus inconsistent with others, and it is deemed to be insufficient to study viscous heating. Here, we propose to use the conservation equations, which are derivable from the Boltzmann equation, and intrinsic properties of Couette and Poiseuille flow. This approach bypasses the difficulties in solving the full Boltzmann equation

7.3.1 Viscous heating in Couette flow

Couette flow is a flow confined between two boundaries moving relative to each other as shown in Fig. 7.3. In continuum theory, the viscous dissipation is solely induced by the flow. When a gas is rarefied, the gas slips near the boundary, i.e., the gas velocity at the boundary is different from that of the boundary, and the friction force at the boundary will do some work. Thus viscous dissipation in a flow of a rarefied gas has two contributions: one is due to the flow and the other is due to work done by the friction force at the boundary Springer [1971].

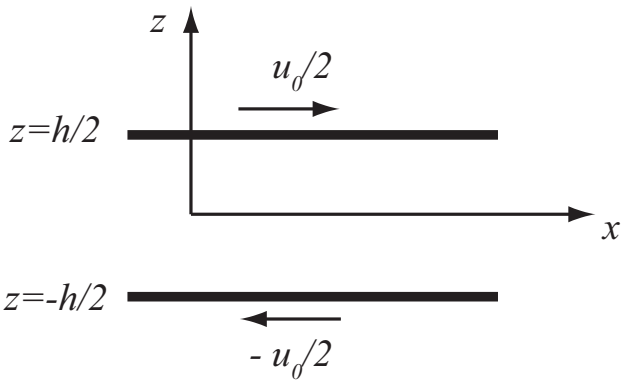

Figure 7.3: Couette flow confined between two boundaries moving relative to each other at a speed of u_0

Let us first consider the contribution from the gas flow. For the Couette flow part in the HDI, flow velocity perpendicular to the streamwise direction is negligible and the film thickness is much smaller than its length, so that the energy conservation equation reduces to

$$\frac{\partial}{\partial z}\left(\tau_{zx} v_x - q_z\right) = 0 \tag{7.6}$$

where the x direction is along the boundary, the z direction is perpendicular to the boundary, τ_{zx} is one component of the shear stress tensor, and q_z is the heat flux perpendicular to the boundary.

By integrating Eq. (7.6) from the lower boundary $z = -h/2$ to the upper boundary $z = h/2$ shown in Fig. (7.3), we get

$$\tau_{zx}|_{z=h/2} v_x|_{z=h/2} - \tau_{zx}|_{z=-h/2} v_x|_{z=-h/2} = q_z|_{z=h/2} - q_z|_{z=-h/2} \tag{7.7}$$

Given the geometry arrangement in Fig. 7.3, Couette flow is skew symmetric with respect to the center line, and we have $q_z|_{z=-h/2} = -q_z|_{y=h/2}$, $u_x|_{y=-h/2} = -u_x|_{y=h/2}$ and $\tau_{xz}|_{z=h/2} = \tau_{xz}|_{z=h/2}$. Here we also use the assumption that the accommodation coefficients of the two boundaries are the same, which is widely used in solving the generalized Reynolds equation in the HDI. Then we can arrive at

$$q_z|_{z=h/2} = \tau_{xz}|_{z=h/2} \cdot u_x|_{z=h/2} \tag{7.8}$$

Note that $u_x|_{y=h/2}$ is the velocity of the gas next to the boundary

The second contribution, due to the friction work, is $\tau_{xy}|_{y=h} \cdot u_{slip}$. By combining the two contributions, we get the total heat flux on the boundary

$$q_z = \tau_{xz}|_{z=h/2} \left(u_{slip} + u_x\right)|_{z=h/2} = \tau_{xz}|_{y=z} \frac{u_0}{2} \tag{7.9}$$

The shear stress can be obtained from the moment method [Vincenti and Kruger 1965], and we can finally obtain

$$q_y|_{y=h} = \frac{1}{4} \rho U^2 \sqrt{\frac{8RT}{\pi}} \frac{\lambda}{d + 2\lambda} \tag{7.10}$$

where R is the gas specific constant and T is the boundary's temperature. This is exactly the same empirical formula proposed by Ju [Ju 2000] to fit his DSMC results for viscous heating in the Couette flow. Ju originally argued that the difference between Eq. (7.8) and Eq. (7.9) is due to the difference between the less frequent intermolecular collisions and collisions between the fluid molecules and the plates. However, as shown in our derivation, Eq. (7.8) and Eq. (7.9) correspond to heat transfer in different cases and the main difference is caused by the gas slip on the boundary.

7.3.2 Viscous heating in Poiseuille flow

Poiseuille flow is a flow confined between two boundaries and driven by a pressure gradient as shown in Fig. 7.4 Viscous dissipation in Poiseuille flow of a rarefied gas also has two contributions: one is due to the flow and the other is due to the work done by the friction force. Again, we first work with the conservation equations to get the first contribution. Due to the pressure gradient, all flow quantities for Poiseuille flow, such as flow velocity and pressure, change along the flow, which is different from Couette flow. Thus, the conservation equations for Poiseuille flow are more complex than for Couette flow, and we need to use more techniques than for Couette flow.

Under the same assumption as for Couette flow, the full set of conservation equations for

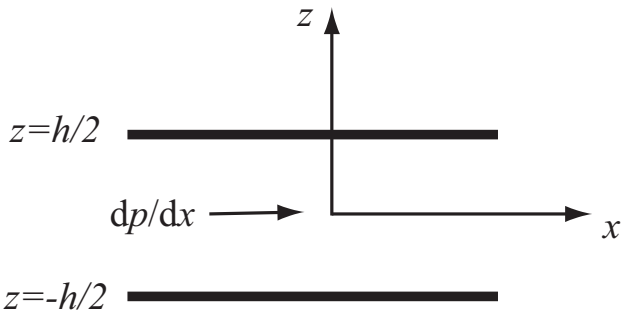

Figure 7.4: Poiseuille flow confined between two boundaries and driven by a pressure gradient of $\mathrm{d}p/\mathrm{d}x$

Poiseuille flow reduces to

$$\frac{\partial}{\partial x}\left(\rho v_x\right) = 0 \tag{7.11}$$

$$\frac{\partial}{\partial x}\left(\rho v_x^2 + \tau_{xx}\right) + \frac{\partial}{\partial z}\left(\sigma_{xz}\right) = 0 \tag{7.12}$$

$$\rho v_x \frac{\partial h}{\partial x} + \rho v_x^2 \frac{\partial v_x}{\partial x} = \frac{\partial}{\partial x}\left(\tau_{xx} v_x - q_x\right) + \frac{\partial}{\partial z}\left(\tau_{zx} v_x - q_z\right) \tag{7.13}$$

Using Eq. (7.11) in Eq. (7.12) and Eq. (7.13), we can eliminate the derivatives of v_x and obtain

$$-v_x^2 \frac{\partial \rho}{\partial x} + \frac{\partial \sigma_{xx}}{\partial x} + \frac{\partial \sigma_{xz}}{\partial z} = 0 \tag{7.14}$$

$$\rho v_x \frac{\partial h}{\partial x} - v_x^3 \frac{\partial \rho}{\partial x} = v_x \frac{\partial \tau_{xx}}{\partial x} - \frac{1}{\rho}\tau_{xx} v_x \frac{\partial \rho}{\partial x} - \frac{\partial q_x}{\partial x} + \frac{\partial}{\partial z}\left(\tau_{zx} v_x - q_z\right) \tag{7.15}$$

Now we use the same idea as used in Sec. 6.2 to consider the order of each term appearing in Eqs. (7.14) and (7.15). For the Poiseuille flow part in the HDI, the dimensionless pressure gradient is assumed to be small, i.e., $(h_m/p_0)\mathrm{d}p/\mathrm{d}x \ll 1$ where h_m is the reference air gap thickness. This assumption underlies the derivation of the generalized Reynolds equation. Then all quantities such as velocity and pressure can be expanded as Taylor series of the dimensionless pressure gradient. The first non-zero term in the series is regarded as the order of the quantities. Then, with the help of kintic theory, we find that ρ is of the zeroth order, v_x and $\partial\rho/\partial x$ are both of the first order. Thus the first term in Eq. (7.15), proportional to $v_x \partial h/\partial x$, is higher than second order. The second term on the left hand side of Eq. (7.15) involves v_x^3 and is again higher than second order. Since $\partial\tau_{xx}/\partial x$ is higher than first order while v_x and $\partial\rho/\partial x$ are both of first order, the first two terms on the right hand side are both higher than second order. Then, only retaining in Eq. (7.15) the terms of the lowest order, i.e., the second order, we reduce the energy equation to

$$\frac{\partial q_y}{\partial y} = \frac{\partial}{\partial y}\left(\tau_{yx} v_x\right) - \frac{\partial q_x}{\partial x} \tag{7.16}$$

Integrating Eq. (7.16) from the lower boundary $z = -h/2$ to the upper boundary $z = h/2$, we get

$$q_z|_{z=h/2} - q_z|_{z=-h/2} = \tau_{xy}|_{z=h/2} v_x|_{z=h/2} - \frac{\partial}{\partial x}\int_{-h/2}^{h/2} q_x dz \tag{7.17}$$

The geometry arrangement in Fig. 7.4 is now symmetric with respect to $z = 0$, and, similar to Couette flow, we have

$$\begin{aligned} \tau_{zx}|_{z=-h/2}\mathbf{n}_{z=-h/2} =& \sigma_{zx}|_{z=-h/2}\mathbf{n}_{z=-h/2} \\ q_z|_{z=-h/2}\mathbf{n}_{z=-h/2} =& q_y|_{z=-h/2}\mathbf{n}_{z=-h/2} \\ \mathbf{n}_{z=-h/2} =& -\mathbf{n}_{z=h/2} \end{aligned} \tag{7.18}$$

Thus, $\sigma_{zx}|_{z=-h/2} = -\sigma_{zx}|_{z=-h/2}$ and $q_z|_{z=-h/2} = q_z|_{z=h/2}$. and Eq. (7.17) becomes

$$q_z|_{z=h/2} = \tau_{xz}|_{z=h/2} v_x|_{z=h/2} - \frac{1}{2}\frac{\partial}{\partial x}\int_{-h/2}^{h/2} q_x dz \tag{7.19}$$

The second term thus poses a challenge in evaluating q_z. However, as shown by the numerical studies [Wang and Li 2004], the derivative of $\int_{h/2}^{-h/2} q_x dy$ along the flow is negligible. Then $q_z|_{z=h/2} = \tau_{xz}|_{z=h/2} v_x|_{z=h/2}$. Although this formula is the same as obtained by Sheng and Chen [Shen and Chen 2008], our derivation is totally different from theirs. Shen and Chen's method is based on the linearized Boltzmann equation, which, by the classical approach, is incapable of dealing with the heat dissipation [Fukui and Kaneko 1988]. Shen and Chen used the general formula for heat transfer, instead of the linearized version as used in classical treatment [Sone 2006]. Since this general formula involves an integration of ϕ and the linearized Boltzmann equation only gives information on the linear terms in ϕ, the calculation of the heat dissipation, as shown above, is a second order effect. Shen and Chen implicitly used the assumption that the contribution of second order terms in ϕ to the integration is negligible, which is hard to verify, and then they arrived at Eq. (7.19). In contrast, our present derivation only deals with macroscopic quantities and conservation equations, which bypass the Boltzmann equation, and does not need any assumptions on ϕ. From the shear stress for Poiseuille flow, Eq. (6.7), we finally arrive at

$$q_y = \frac{h}{2}\frac{\partial p}{\partial x} v_x|_{z=h/2} \tag{7.20}$$

which reduces the evaluation of q_y to that of the slip velocity v_x and significantly reduces the work of Shen and Chen in the evaluation of q_y from $q_y = \tau_{xy} v_x$, where both τ_{xy} and v_x are obtained from the linearized Boltmzann equation.

The second contribution due to friction work is $\frac{h}{2}\frac{\partial p}{\partial x} v_{slip}|_{y=h/2}$, and the total heat flux on the upper boundary is

$$\frac{h}{2}\frac{\partial p}{\partial x}\left(v_{slip}|_{z=h/2} + v_x|_{z=h/2}\right) = 0 \tag{7.21}$$

since the velocity of the upper boundary $z = h/2$ is zero.

7.4 Importance of heat dissipation compared to heat conduction

7.4.1 Importance of heat dissipation due to the Couette flow part

The total heat flux including heat conduction and heat dissipation due to Couette flow is [Ju 2000]

$$q = -k\frac{T_s - T_d}{h + 2\frac{2-\sigma_T}{\sigma_T}\frac{2\gamma}{\gamma+1}\frac{1}{\mathrm{Pr}}\lambda} + \frac{1}{8}\rho U^2\sqrt{\frac{8RT_0}{\pi}}\frac{\lambda}{h+2\lambda} \tag{7.22}$$

where ρ is the density of the air, U is the disk's linear speed, T_0 is the ambient temperature, and R is the specific gas constant. Replacing Eq. (7.1) by Eq. (7.22) in our code does not produce any difference in the final results. This can be explained by comparing the order of the two terms in Eq. (7.22). As an estimation, we choose $\mathrm{Pr} = 2/3$, $\gamma = 1.4$, $\sigma_T = 1$, $T_0 = 300\mathrm{K}$, $k = 0.025\mathrm{W/(m\cdot K)}$, and $R = 287\mathrm{J/(kg\cdot K)}$. Since air density is proportional to pressure and mean free path is inversely proportional to pressure, $\lambda\rho = \lambda_0\rho_0$ where $\lambda_0 = 65\mathrm{nm}$, $\rho_0 = 1.204\mathrm{kg/m^3}$, and quantities with a subscript 0 refer to their values at the ambient state. Then the ratio of the second term, representing the contribution of heat dissipation, to the first one, representing the contribution of heat conduction, becomes

$$2\times 10^{-4}\frac{U^2}{T_s - T_d}\frac{h + 14\lambda/9}{h+2\lambda} \sim 2\times 10^{-4}\frac{U^2}{T_s - T_d} \tag{7.23}$$

As shown by numerical results, the heat transfer on the ABS is only significant near the transducer. For typical commercial HDDs, U is on the order of 10m/s and the temperature difference near the transducer $T_s - T_d$ is within 10K, which makes the ratio in Eq. (7.23) on the order of $10^{-3} - 10^{-2}$. Thus the contribution of heat dissipation is negligible and only contribution of heat conduction needs to be considered, agreeing with our numerical results.

7.4.2 Importance of heat dissipation due to the Poiseuille flow part

As discussed in the last section, the heat dissipation due to the Poiseuille flow part vanishes. As a companion to our theoretical analysis, we here use the direction simulation Monto Carlo (DSMC) method to numerically investigate heat dissipation in Poiseuille flow confined by two boundaries at different tempertures.

The DSMC method does not solve the Boltzmann equation, but it is equivalent to solving the Boltzmann equation [Bird 1994]. By using one particle to represent a large amount of real molecules, the DSMC method, compared to molecular dynamics (MD) methods, can investigate problems of macroscopic scale, and it is also faster than the MD method, which makes DSMC method the *de facto* numerical method in rarefied gas dynamics. Here we use the DS2V/3V program suite [Bird 2005] to perform DSMC simulation.

The case we consider has a distance between two boundaries $h = 60\mathrm{nm}$, which gives a Knudsen number $\mathrm{Kn}=\lambda/h \sim 1$ since the mean free path of air in standard condition is around 65nm. Let us first consider isothermal Poiseuille flow between two boundaries at the same temperature to check the accuracy of our numerical results. Figure 7.5 shows the

pressure distribution in Poiseuille flow, which changes linearly along the flow. This agrees with our assumption that the dimensionless pressure gradient is very small.

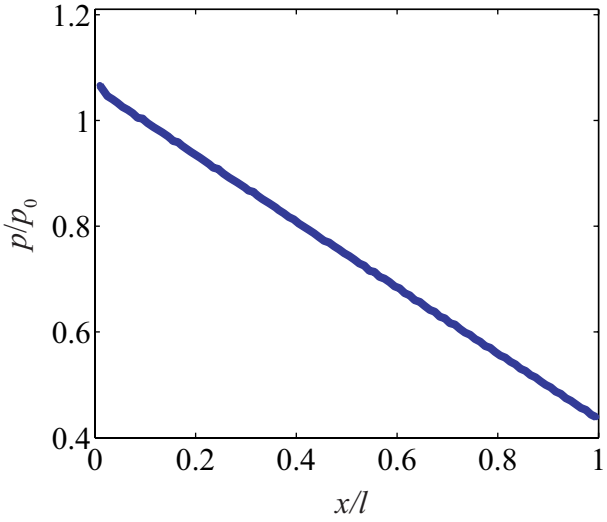

Figure 7.5: Pressure in isothermal Poiseuille flow.

Figure 7.6 compares the shear force calculated by Eq. (6.7) and that by DSMC. Despite the scattering of the data due to the statistical nature of the DSMC method, the theoretical prediction agrees with numerical results. Figure 7.7 shows the heat flux on the boundary calculated by the DSMC method. The numerical results fluctuate around 0 with a fluctuation as high as $4 \times 10^4 \mathrm{W/m^2}$. To check whether viscous dissipation is important compared to heat conduction, we perform a DSMC investigation of the Poiseuille flow confined between two boundaries at different temperatures, and the results are shown in Fig. 7.8. The heat flux now has two contributions: heat conduction and viscous dissipation. We note that the total heat flux is on the order of $10^7 \mathrm{W/m^2}$, which is much higher than the maximum fluctuation appearing in Fig. 7.7. Thus, viscous dissipation due to Poiseuille flow is negligible, agreeing with our analytic analysis.

7.5 Accuracy of the currently used heat conduction model

As discussed above, heat conduction dominates the heat flux on the slider's surface, and, as shown in Fig. 7.2, the heat flux predicted by the first order slip theory differs from widely accepted data by about 10% when the Knudsen number is larger than 10. Since calculating the TFC sliders' deformation is a nonlinear process, it is unknown *a priori* how much error this 10% difference will finally cause for the TFC slider's flying performance, which raises some concerns about the accuracy of numerical predictions based on the current model.

The calculation of a TFC sliders' flying performance involves modeling the complex structure of the heating element and the read-write transducer and calculating the slider's deformation based on its thermoelastic properties, for which iterative approaches have been

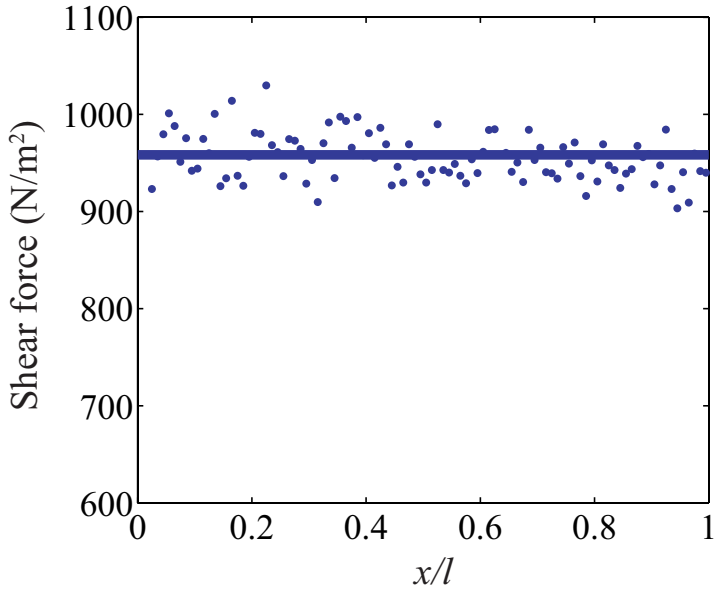

Figure 7.6: Comparison of the shear force on the boundary predicted by the analytical formula Eq. (6.7) and that by the DSMC method.

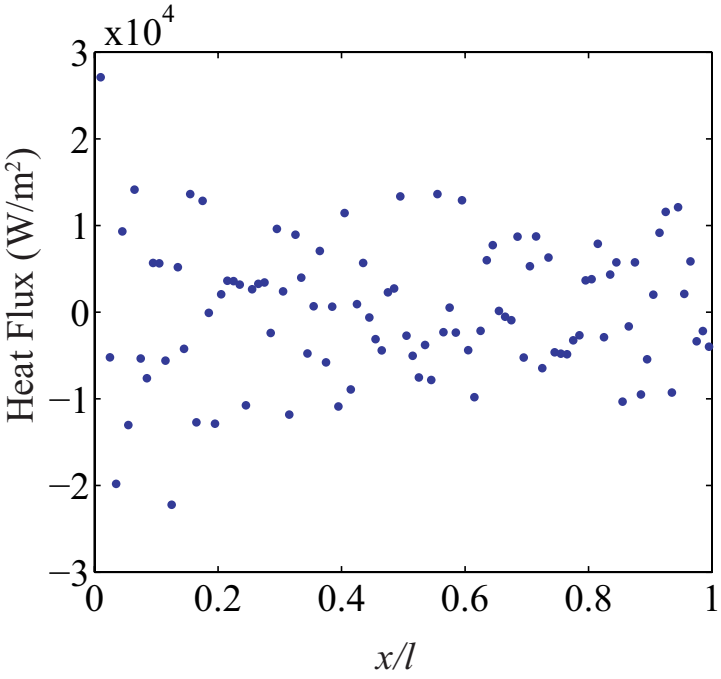

Figure 7.7: Heat flux on the boundary of an isothermal Poiseuille flow calculated by the DSMC method.

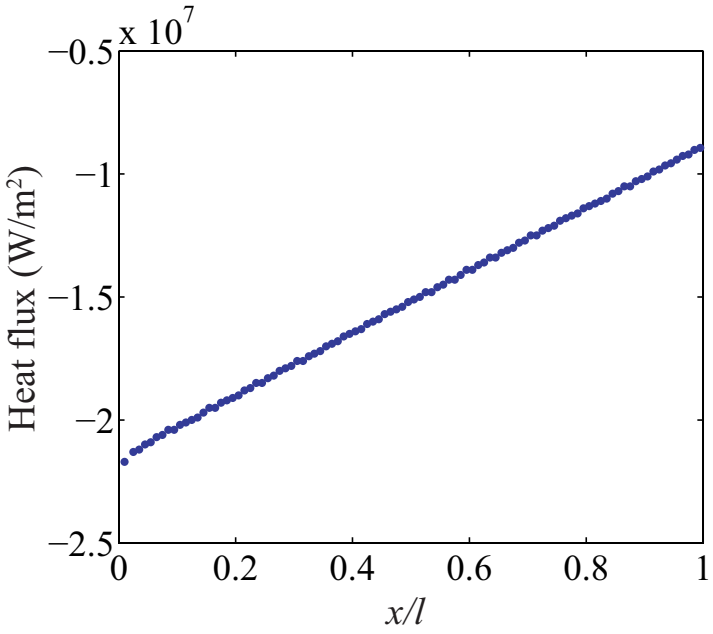

Figure 7.8: Heat flux on the boundary of a non-isothermal Poiseuille flow calculated by the DSMC method.

used and proven to be effective [Juang et al. 2006; Li et al. 2009; Zheng and Bogy 2009b]. This approach iterates between two steps: in the first step, the air flow field and the air pressure distribution in the HDI are calculated by using the finite volume method (FVM) to solve the generalized Reynolds equation [Lu 1997]; in the second step, the slider's deformation and the deformed ABS profile are calculated using a commercial finite element solver ANSYS [Inc. 2007] with detailed models of the heating element and read-write transducer [Zheng and Bogy 2009a].

Figure 7.9 shows the air pressure distribution on a commercial TFC slider's ABS. A pressure peak appears near the transducer, which makes the air flow underneath the transducer act as a spring with a high stiffness to stabilize the slider as it moves on the disk. This pressure peak decreases the local mean free path and local Knudsen number since the mean free path is inversely proportional to the local pressure.

Figure 7.10 shows a comparison of the reduction in the slider's flying height at the transducer resulting from the slider's thermal deformation. Both of the numerical results compare well with experiments, but the one based on Chen *et al.*'s model shows slightly less difference from the experiments. The maximum difference between the two predictions is around 0.1nm as seen from the inset.

Figure 7.11 shows the relative difference in the minimum flying height (FH) predicted by the current model and the new model. The difference increases as the slider's minimum FH decreases, but the difference, even for a minimum FH of 1.8nm, is only 7%. The main reason the difference is so small is due to the fact that the error presented in the current model appears only when the Knudsen number, defined as the ratio of the local mean free path (MFP) to the slider's local FH, is very high [Chen et al. 2009]. Since the mean free

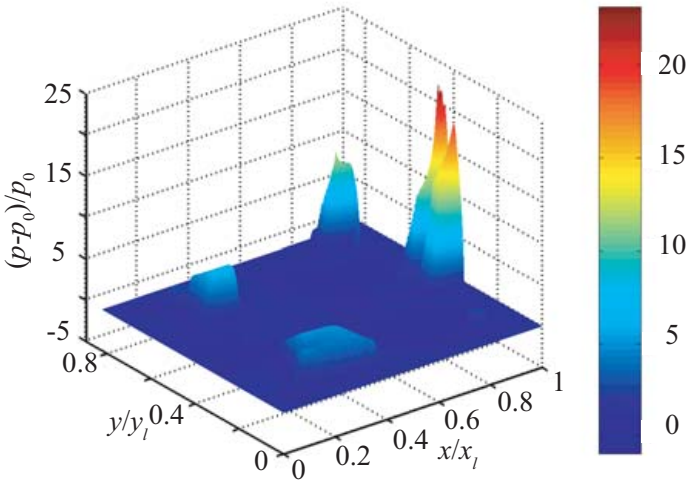

Figure 7.9: Typical air pressure distribution on the ABS of the slider. The peak is located near the transducer. x_l is the slider's length, p is the air pressure in the HDI, p_0 is the ambient pressure outside the HDI, and x and y are along the length and width directions of the slider respectively.

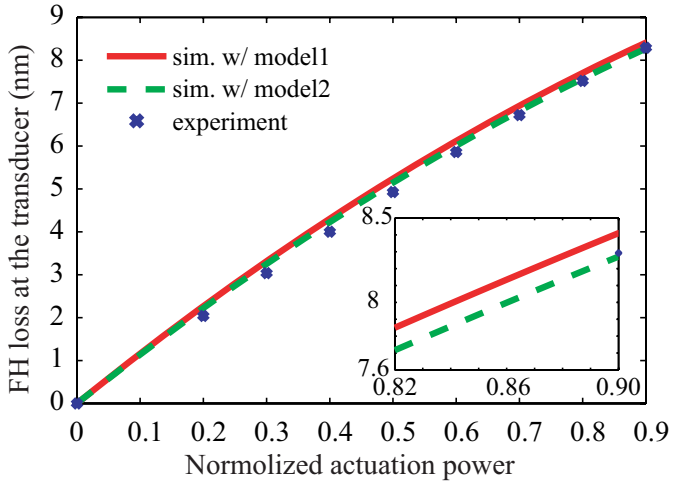

Figure 7.10: The loss of the slider's flying height at the read-write transducer. The model 1 refers to the model based on the first order slip theory as represented by Eq. (7.1) and the model 2 refers to Chen *et al.*'s model with the modified mean free path in Eq. (7.4).

path is inversely proportional to the local pressure and the pressure near the transducer is relatively quite high, the local MFP near the transducer is much smaller than the ambient MFP and therefore the Knudsen number underneath the read-write transducer is not very large. Thus, the current model does not cause much error in comparison with experiments, and the prediction based on the current model is close to that based on the more accurate new model [Liu et al. 2010a].

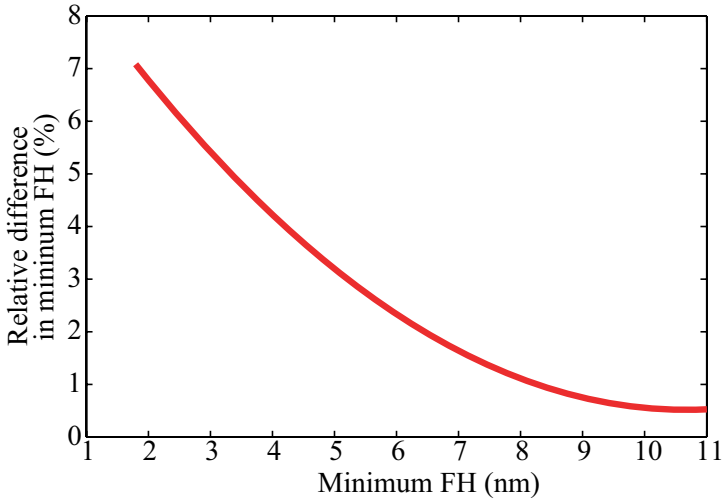

Figure 7.11: Relative difference in minimum flying height predicted by the two models.

7.6 Summary and conclusion

A new phenomenological heat transfer model in which the mean free path is modified to include the effect of collisions between molecules and boundaries has been applied to the prediction of the flying performance of thermal flying height control sliders. The air bearing cooling predicted by this model is stronger due to this modified mean free path, and this results in a reduced protrusion around the transducer. Simulation results based on the more accurate model compares well with experiments and are slightly better than those based on the traditional first order slip theory. The error induced by the current model based on the first order slip theory is less than 10% for state-of-art TFC sliders for which a pressure peak appears near the transducer and decreases the local mean free path and local Knudsen number. Unless the local Knudsen number near the transducer is quite large, the prediction based on the current model involves an error less than 10% and therefore it is sufficiently accurate. By numerical simulation and theoretical analysis, we also validate the current strategy of considering heat conduction induced by the moving air in the HDI as the dominant contributor to the heat flux on the ABS.

Chapter 8

TFC sliders in air-helium gas mixtures

8.1 Introduction

To compete with other storage devices such as flash memory, HDDs, which have served as the dominant storage device for several decades, need to have lower operational cost, better reliability and larger capacity. A key to the first goal is reducing the power consumption of HDDs during operation. The HDDs' power cost is becoming a bigger issue and could be a barrier for HDDs to continue serving as a major storage device in the future [Gurumurthi et al. 2003; Aruga et al. 2007]. More than 1/3 of this power is used to counteract the drag resisting the disk's motion and is dissipated into the HDDs' enclosure, which results in the temperature increase inside the HDD and is known as windage loss [Aruga et al. 2007]. The reliability issues faced by HDDs include the disks' corrosion and track mis-registration due to air-turbulence that introduces unpredictable vibration of the read-write head. Replacing current state-of-the-art HDDs by HDDs filled with the inert gas Helium promises to resolve most, if not all, of the above issues [Liu et al. 2010c]. In a state-of-the-art HDD, the air flow inside the HDD is turbulent and the windage loss is $W_A \propto \rho_A \nu_A^{0.2}$ where ρ_A is the air density, and ν_A is the kinematic viscosity of air. However, due to helium's low density, the gas flow inside a helium-filled HDD rotating at the same speed as the current commercial HDDs is laminar and the windage loss is $W_H \propto \rho_H \nu_H^{0.5}$, where ρ_H is the helium density and ν_H is the kinematic viscosity of helium. For the same HDD, W_H is much smaller than W_A, resulting in a much smaller temperature increase inside the helium-filled HDD. This is confirmed by experiments which showed that the maximum temperature inside an air-filled HDD is about 50°C compared to about 35°C when the HDD is filled with helium [Sata et al. 1988; Yang et al. 2009]. The laminar flow field existing in a helium-filled HDD also results in less unpredictable vibration of the head, less track mis-registration and better reliability [Aruga et al. 2007]. Many HDD companies have already utilized this known fact to operate their drives in "unsealed" gas mixtures for the servo writing process. The inert property of helium further helps to protect the disk from corrosion.

The concept of helium-filled HDDs can be traced back to 1980's [Sata et al. 1988], but no commercial products have appeared since helium is difficult to seal due to its small density. Recent years have seen much progress on hermetically sealing HDDs filled with helium, and several efficient manufacturing methods have been proposed [Money 2006; Suzuki et al. 2009; Kouno et al. 2009; Uefune et al. 2009], which makes massive production of helium-filled

HDDs much more feasible. However, filling HDDs with pure helium increases production cost, and so air-helium gas mixtures are currently being investigated as a candidate to balance performance and cost. We note that even at the current high cost, some defense related or space applications may choose a sealed drive if the advantage overrides the cost.

Among the different requirements for increasing the HDDs' capacity, reducing the distance between the read-write transducer and the magnetic disk is an important one.The state-of-the-art TFC sliders have an embedded heating element near the transducer. Supplying power to the heating element induces a temperature increase around the element, leading to the slider's thermo-elastic protrusion near the transducer and thereby produces a smaller spacing between the transducer and the disk. Putting TFC sliders in HDDs filled with an air-helium gas mixture seems to be an effective approach to increase the HDDs' capacity and reliability, to decrease their operational cost and power consumption, and to balance performance with production cost.

The flying performance of TFC sliders in air has been thoroughly investigated. Juang, Chen and Bogy [Juang et al. 2006], among others, proposed an iterative approach to numerically predict the TFC sliders' flying performance and obtained results agreeing well with experiments [Li et al. 2009]. HDDS filled with pure helium have also been investigated. Aruga *et al.* [Aruga et al. 2007] found that helium can significantly reduce the gas induced disturbance on the suspension and the read-write transducer's position errors. Zhou *et al.* [Zhou et al. 2009] numerically investigated TFC sliders' flying performance in pure helium. However, no work has been done for an air-helium gas mixture instead of air or helium. In view of the advantage of combining TFC sliders with HDDs filled with air-helium gas mixtures, we investigate how the mixture affects the TFC sliders' flying performance. The general methodology proposed in this chapter will also help to understand the performance of TFC sliders in "unsealed" gas mixtures currently used for servo writing.

This chapter is organized as follows. In Sec. 8.2, the numerical approaches used to calculate the TFC sliders' flying performance, together with the related background theories, are discussed. In Sec. 8.3, established approaches for calculating the physical properties of gas mixtures are discussed and compared with experiments. Numerical results are presented and discussed in Sec. 8.4. A summary and conclusion is given in Sec. 8.5.

8.2 Numerical approach

The iterative approach originally proposed by Juang *et al.* [Juang et al. 2006] iterates between two steps: in one step, the finite volume method is used to solve the generalized Reynolds equation for the slider's flying attitude, the air flow field and pressure distribution in the HDI for a given slider's geometry [Lu 1997]; in the other step, the finite element method (FEM) implemented in a commercial FEM solver is used to solve for the slider's deformation for a given power applied to the heater element with the previously obtained gas pressure and heat flux on the ABS being boundary conditions.

The gas flow in the HDI is characterized by the generalized Reynolds equation Eq. (6.14) and two physical properties of the gas are required for solving Eq. (6.14), namely, the viscosity μ and the mean free path λ. The heat flux on the ABS has been shown to be dominated by the heat conduction between the slider and the disk at different temperatures, which

can be calculated to sufficient accuracy by Eq. (7.1). The physical properties involved in Eq. (7.1), in addition to the mean free path and viscosity, include the thermal conductivity and heat capacities, which can be divided into two categories: the intrinsic ones including the mean free path, the viscosity and the thermal conductivity; and the extrinsic ones including the heat capacities. In the next section, we discuss how to obtain these properties for gas mixtures.

8.3 Physical properties of gas mixtures

The values of the extrinsic quantities for gas mixtures can be obtained from linear interpolation. For example, the heat capacity C_p of an air-helium gas mixture is $C_{pm} = \alpha C_{pH} + (1-\alpha)C_{pA}$ where α is the fraction of helium, and the subscripts H and A refer to the values for helium and air, respectively.

The intrinsic properties of the gas mixture can not be obtained simply from linear interpolation. Instead, we need to treat them separately. The mean free path of gas mixtures can be calculated from the following equation, which is derived from kinetic theory [Bird 1994]

$$\begin{aligned}\lambda_m =& \frac{\alpha}{\sqrt{2}\pi d_H^2 n\alpha + \pi d_{HA}^2 n(1-\alpha)\sqrt{1+\frac{M_H}{M_A}}} \\ &+ \frac{1-\alpha}{\sqrt{2}\pi d_A^2 n\alpha + \pi d_{HA}^2 n(1-\alpha)\sqrt{1+\frac{M_A}{M_H}}}\end{aligned} \tag{8.1}$$

where n is the number of molecules per unit volume, d is the molecular diameter, M is the molecular weight, the subscripts H and A refer to the corresponding values for helium and air, and $d_{HA} = (d_H + d_A)/2$.

The viscosity of the gas mixture can be obtained from Reichenberg's method [Poling et al. 2001]

$$\mu_m = K_H(1 + H_{HA}^2 K_A^2) + K_A(1 + 2H_{HA}K_H + H_{HA}^2 K_H^2) \tag{8.2}$$

with

$$\begin{aligned}K_H &= \frac{\alpha\mu_H}{\alpha + (1-\alpha)\mu_H H_{HA}[3 + (2M_A/M_H)]} \\ K_A &= \frac{(1-\alpha)\mu_A}{(1-\alpha) + \alpha\mu_A H_{HA}[3 + (2M_H/M_A)]} \\ H_{HA} &= \frac{\sqrt{M_H M_A/32}}{(M_H + M_A)^{1.5}} Z_{HA}\left(\frac{M_H^{0.25}}{\sqrt{\mu_H Z_H}} + \frac{M_A^{0.25}}{\sqrt{\mu_A Z_A}}\right)^2 \\ Z_H &= \frac{[1 + 0.36T_{rH}(T_{rH} - 1)]^{1/6}}{\sqrt{T_{rH}}} \\ Z_A &= \frac{[1 + 0.36T_{rA}(T_{rA} - 1)]^{1/6}}{\sqrt{T_{rA}}} \\ Z_{HA} &= \frac{[1 + 0.36T_{rHA}(T_{rHA} - 1)]^{1/6}}{\sqrt{T_{rHA}}}\end{aligned}$$

Table 8.1: Physical properties of air-helium gas mixtures.

α	λ_m (nm)	μ_m (μN·s/m^2)	k_m (W/(m·K))	C_{pm} (KJ/(kg·K))	C_{vm} (KJ/(kg·K))
0	67.10	18.60	0.0262	1.0064	0.7181
0.1	73.27	18.90	0.0293	1.4250	0.9591
0.2	80.72	19.21	0.033	1.8436	1.2001
0.3	89.50	19.53	0.0374	2.2622	1.4411
0.4	99.65	19.85	0.0429	2.6809	1.6821
0.5	111.25	20.17	0.0497	3.0995	1.9231
0.6	124.38	20.46	0.0586	3.5181	2.1641
0.7	139.13	20.68	0.0704	3.9367	2.4051
0.8	155.63	20.78	0.0873	4.3554	2.6461
0.9	174.02	20.63	0.1129	4.7740	2.8871
1	194.46	20.00	0.1567	5.1926	3.1282

where $T_{rH} = T/T_{cH}$, $T_{rA} = T/T_{cA}$, $T_{rHA} = T/\sqrt{T_{cA}T_{cH}}$, T is the gas temperature, and T_{cH} and T_{cA} are critical temperatures of helium and air, respectively.

The thermal conductivity of the gas mixture is obtained from the Wassiljewa equation [Poling et al. 2001].

$$k_m = \frac{\alpha k_H}{\alpha + (1-\alpha)A_{HA}} + \frac{(1-\alpha)k_A}{(1-\alpha) + \alpha A_{AH}} \tag{8.3}$$

with

$$A_{ij} = \frac{[1 + \sqrt{k_{ij}}(M_i/M_j)^{0.25}]^2}{\sqrt{8[1 + (M_i/M_j)]}}$$
$$k_{ij} = \frac{[\exp(0.04664T_{ri}) - \exp(-0.2412T_{ri})]\Gamma_j}{[\exp(0.04664T_{rj}) - \exp(-0.2412T_{rj})]\Gamma_i}$$

where $\Gamma_i = 210(T_{ci}M_i^3/P_{ci}^4)^{1/6}$, P_c is the critical pressure, and i and j can be either H or A. We note that the units used to calculate Γ_i are not all standard. Although the critical temperature T_{ci} is in Kelvin, the molecular weight M_i is in g/mol and the critical pressure P_{ci} is in bar.

Table 8.1 shows all of the relevant physical properties for different fractions of helium in the gas mixture as calculated from Eqs. (8.3), (8.1) and (8.2). The parameters required in this calculation are [Lide 2008; Lemmon et al. 2000]: d_H=0.366nm, d_A=0.215nm, M_H=28.966g/mol, M_A=4.003g/mol, T_{cH}=132.53K, T_{cA}=5.19K, P_{cH}=37.86bar and P_{cA}=2.27bar. As shown in Fig. 8.1, the mean free path of the gas mixture increases by 200% as the fraction of helium in the gas mixture α increases from 0 to 1, and the thermal conductivity of the gas mixture increases by 700%. This large increase underlies helium's ability to quickly dissipate heat generated in HDDs. The rates of change of the mean free path and the thermal conductivity also increase with α.

The viscosity of the air-helium gas mixture changes differently from the mean free path and the thermal conductivity. As shown in Fig. 8.2 and Table 8.1, the viscosity increases

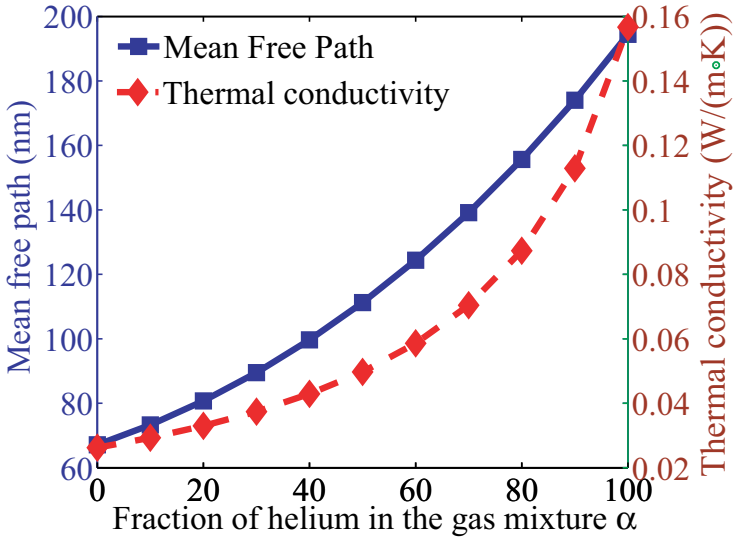

Figure 8.1: Changes of the mean free path and thermal conductivity of air-helium gas mixtures with the fraction of helium in the mixture.

until α reaches about 0.7 after which it decreases. The results from Eq. (8.2) compare well with experimental results, which are excerpted from Ref. [Johns et al. 1982], with relative error less than 5% as shown in Fig. 8.2. We also note that the maximum change in viscosity is no larger than 10%. With all the physical properties obtained, we can now proceed to study the TFC sliders flying in air-helium gas mixtures.

8.4 Results and discussion

The numerical results presented in what follows are obtained for a commercial TFC slider with a length of 0.85mm, a width of 0.7mm and a thickness of 0.23mm. Figure 8.3 shows a typical pressure distribution on the slider's ABS, which is similar, except in the neighborhood of the transducer, for all the cases no matter whether power is applied to the heater. The maximum pressure appears near the protruded area and approximately under the transducer. It acts like a high-stiffness spring helping to stablize the slider when the slider flies over rough surfaces or across tracks. The pressure is almost symmetric about the length centerline, resulting in a near-zero roll angle.

When no power is applied to the heater element, the slider's flying attitude and gas pressure on the ABS can be obtained from the generalized Reynolds equation given the force and torques on the slider applied by the suspension. Increasing the helium content in the gas mixture α increases the mean free path of the gas mixture, leading to fewer molecules in the HDI and less load carrying capability [Liu and Bogy 2009b]. Thus, for a given load, the slider's flying height without heating decreases with α, as shown in Fig. 8.4, and the maximum pressure on the ABS also decreases with α, as shown in Fig. 8.5.

After power is applied to the heater element, a nonuniform temperature field is established in the slider, and due to thermomechanical coupling, the slider deforms accordingly.

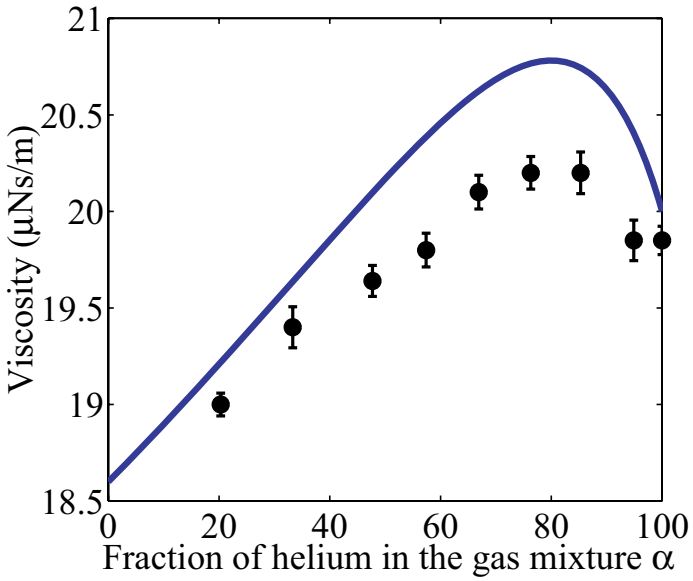

Figure 8.2: Change of the viscosity of air-helium gas mixtures with the fraction of helium in the mixture. The results obtained from Eq. (8.2) are compared with experiments excerpted from Ref. [Johns et al. 1982]. The relative error is generally within 5%.

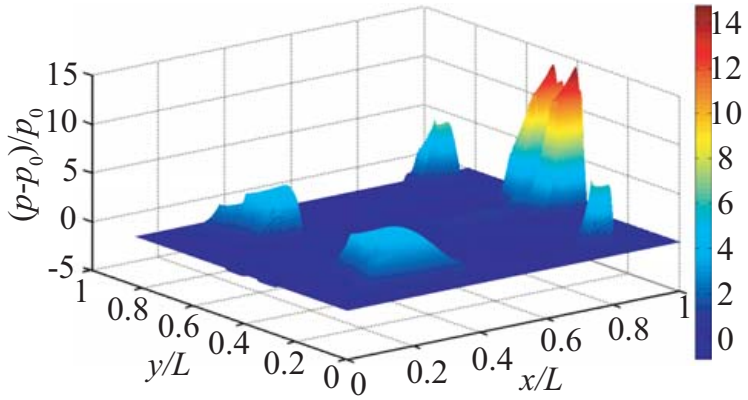

Figure 8.3: Typical pressure distribution on the TFC slider's ABS. The maximum pressure appears near the transducer.

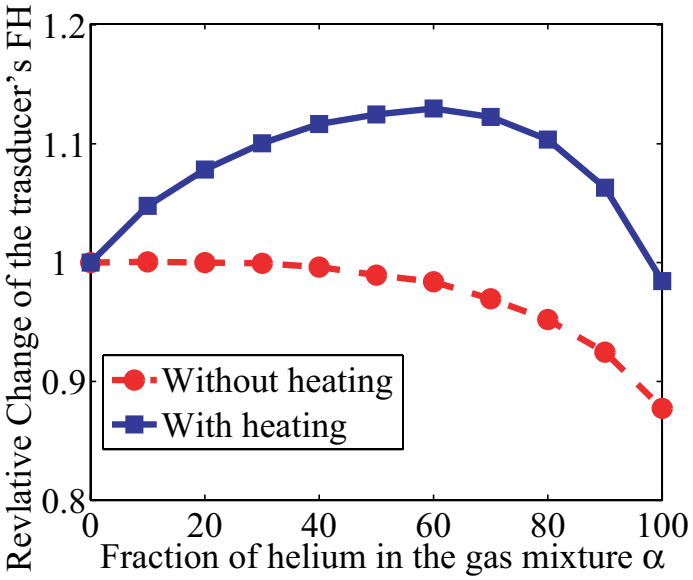

Figure 8.4: Relative change of the gap spacing under the transducer with the fraction of helium in the gas mixture, normalized to the value at $\alpha = 0$. The gap spacing at $\alpha = 0$ without power applied to the heater element is 16.1nm, and that with power is 7.2nm.

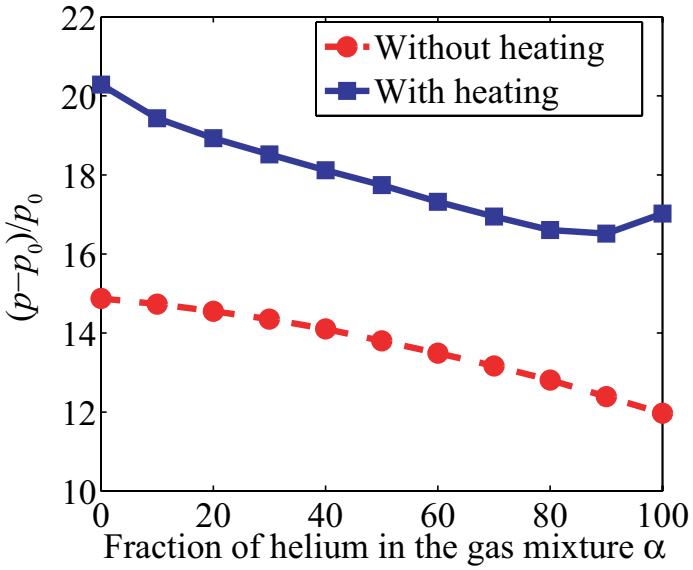

Figure 8.5: Change of the maximum pressure with the fraction of helium in the gas mixture.

Figure 8.6 shows the maximum temperature rise on the ABS at a given power for different values of α. The change of the maximum temperature rise is mainly affected by the heat flux on the ABS which serves as the boundary condition for solving the temperature field in the slider. As a simple estimation of the heat flux, we take in Eq. (7.1) $\sigma \sim 1$, $\gamma \sim 1.5$ and Pr$\sim$ 1, then

$$q \sim -k\frac{T_s - T_d}{h + 2\lambda} \tag{8.4}$$

Since the mean free path is inversely proportional to the local pressure, λ can be estimated to change by a factor of 2 given the maximum pressure shown in Fig. 8.5 and the mean free path in Table 8.1. Since the gap spacing h changes by slightly more than 10% as seen from Fig. 8.4, the denominator of Eq. (8.4) then increases by 2 fold which is consistent with the numerical calculation of the denominator of Eq. (7.1) based on information from Figs. 8.4 and 8.5 and Table 8.1. This increase, when combined with the 8-fold increase in the thermal conductivity as α increases from 0 to 1, results in the increase in the magnitude of the heat flux with α for the same difference in the temperatures of the slider and the disk, leading to more heat dissipated and a smaller maximum temperature rise as seen from the 2-fold decease of the maximum temperature rise with the gas content in Fig. 8.6.

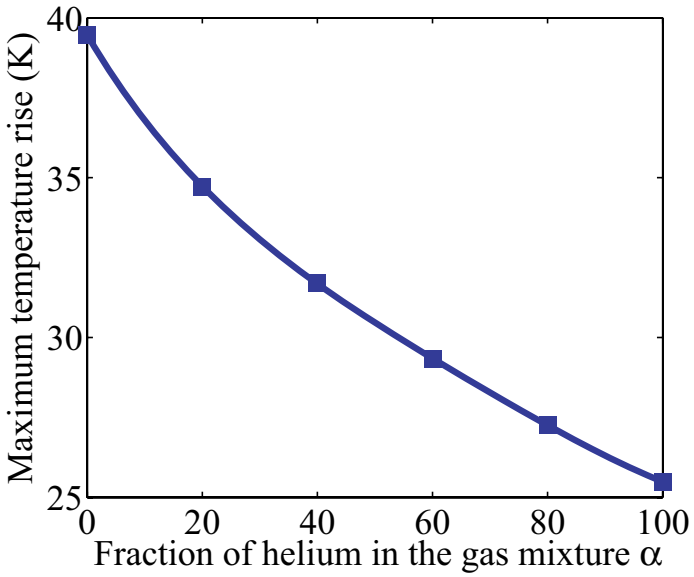

Figure 8.6: Change of the maximum temperature rise with the fraction of helium in the gas mixture.

At a given power applied to the heater element, the change of the slider's deformation with α is mainly determined by the changes of the gas pressure and heat flux on the ABS. Since the pressure's effect on the protrusion is negligible, the change of heat flux dominates. As discussed above, the magnitude of the heat flux increases with α, causing the decrease of the slider's protrusion, as shown in Fig. 8.7. However, the maximum pressure, as seen from Fig. 8.5, first decreases and then increases with the helium content.

Figure 8.7 also shows the TFC slider's flying height loss, which is defined as the difference between the slider's flying height with a given power and that with no power. With the effect

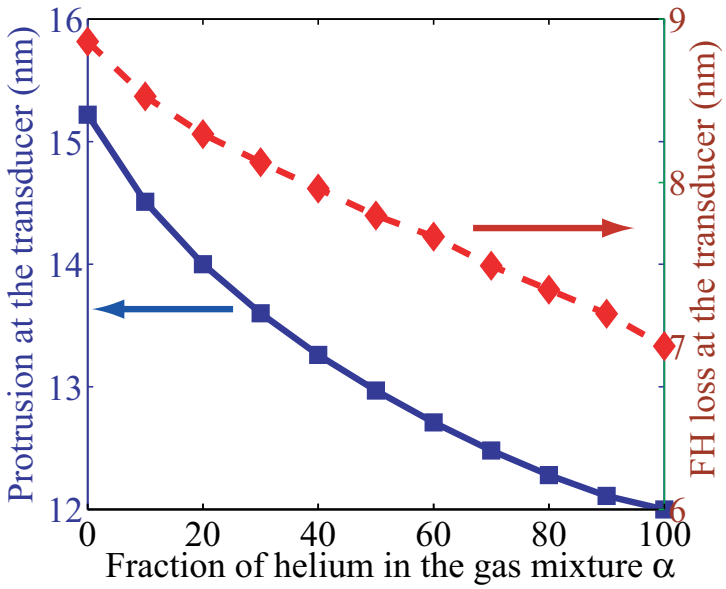

Figure 8.7: Change of the slider's protrusion at the transducer with the fraction of helium in the gas mixture.

of its transducer protrusion, the slider adjusts its flying attitude such that the total pressure on the ABS balances the load applied by the suspension. As a result, the slider's flying height loss is not equal to its protrusion, but it also decreases with the gas content. To quantitatively evaluate the effect of the thermal protrusion on the induced decrease in the slider's flying height, we plot in Fig. 8.8 the so called thermal actuation efficiency (TAE), defined as the ratio of the slider's flying height loss to its protrusion. Compared to that in air, the TAE is slightly higher in helium and, thus, slightly less power is required for a designated flying height loss. The maximum efficiency occurs when the gas mixture is composed of about 40% air and 60% helium, which increases the TAE by 2% compared with that in air. This finding brings out another advantage of using air-helium gas mixtures to fill the HDD: slightly less power is required for the same flying height loss.

The slider's flying height with heating on, $h_{w/}$, is the difference between the slider's FH with no heater power, $h_{w/o}$, as shown in Fig. 8.4, and the FH loss, h_{loss}, i.e. $h_{w/} = h_{w/o} - h_{loss}$, and $h_{w/}$ is due to the combined effects of the mean free path λ, viscosity μ and thermal conductivity k [Liu et al. 2009b]. When α is very small, the effect of λ and μ balance each other such that $h_{w/o}$ remains constant, as shown in Fig. 8.4, while the increase in k reduces h_{loss}, resulting in the initial rise of $h_{w/}$ with α, as shown in Fig. 8.4. As α increases, λ starts dominating and $h_{w/o}$ decreases, leading to the decrease of the rate of change of $h_{w/}$ and the final decrease of $h_{w/}$ when α is greater than 0.6. As α increases further, λ increases and μ starts decreasing, both of which contribute to the decrease of $h_{w/o}$, resulting in the rapid decrease in $h_{w/}$, as seen in Fig. 8.4.

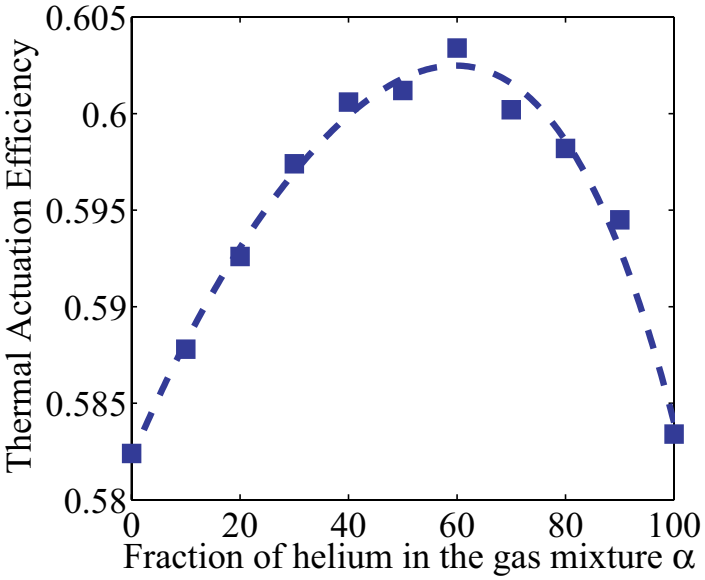

Figure 8.8: Change of the thermal actuation efficiency with the fraction of helium in the gas mixture. The square points are numerical results and the dotted line is a smooth fit of the data with a fourth order polynomial.

8.5 Summary and conclusion

This chapter investigates the flying performance of TFC sliders in air-helium gas mixtures, and it studies the performance of a commercial TFC slider flying in gas mixtures with different gas contents. The slider's flying height loss and its protrusion are shown to decrease with the helium fraction, however, the ratio between the former and the latter quantities display a complex behavior: it first increases with α and finally decreases when α is greater than about 0.6, indicating that the gas mixture of 40% air and 60% helium is the most efficient from the view point of power cost for a designated flying height decrease. The approach proposed here may serve as the basis for designing TFC sliders flying in gas mixtures, and it can also be applied to investigate related problems such as, for example, when the mixture is air and water vapor. Such application is needed in order to investigate a slider's flying performance in a humid environment.

Chapter 9

Summary and conclusion

Despite its dominant status in the information storage market, hard disk drives (HDDs) have been challenged by solid state drives (SDDS) and have lost their dominance in the low-capacity storage market with a storage capacity less than tens of Gigabytes as used in MP3 players and smart phones. Improving HDDs' performance is then critical, especially in this era, for HDDs to compete with the ever improving SSDs. This dissertation applies rarefied gas dynamics to investigate gas flow and particle flows in the HDI with application to HDDs' performance.

Hard disk drives are not free of particles, which might be generated at the manufacturing process or induced by the HDDs' wear. Numerical simulation of particle contamination on a slider helps to design special features to reduce particle contamination on the slider which may scratch the disk and induce loss of data stored on the disk. Chapters 2– 5 investigate how to improve the calculation of forces on a particle moving in the HDI which is the essential part of simulating a particle's motion in the HDI. Chapter 2 investigates the boundary effect– the presence of the slider and the disk–on drag forces experienced by a particle moving in the HDI. A correction factor to account for this effect is incorporated into the drag force formula. A contamination criterion is provided to determine when a particle contaminates a slider. The contamination profile on a specific air bearing surface is obtained, which compares well with experiments and previous investigations.

Chapter 3 analytically investigates the forces on a rotating sphere in a shear flow of a highly rarefied gas. The Chapman-Enskog distribution function is used to describe the velocity distribution of the molecules in the shear flow and a Maxwell-type boundary condition is assumed on the surface of the sphere. Analytical expressions are first obtained for the drag force as well as lift forces for the special case where the gradient of the shear flow is along the same direction as the axis of the particle's rotation. For this case, the effects of particle rotation and shear flow are shown to be decoupled. These lift forces also turn out to be in the opposite directions from their corresponding forces when the fluid is modeled as a continuum. This result is then extended to the case for which the rotation axis of the particle is not restricted with regard to its direction. The contributions to the force from rotation of the particle and nonuniformity of the flow are again shown to be decoupled. These two effects, however, do produce a coupled effect in the torque. Combined with the equation of motion, the trajectory of a spherical particle in a weak shear flow of a highly rarefied gas can be analyzed based on these analytical formulae together with appropriate initial conditions.

Chapter 4 uses a perturbation method to solve the Navier-Stokes equation with the Maxwell slip boundary condition and obtains an analytical formula for forces on spherical particles with slip boundary conditions, which act as a model for particles moving in a slightly rarefied gas. Based on the formulae derived in Chapters 3 and 4, the effect of lift forces on particle contamination on a slider is discussed.

Chapter 5 introduces the temperature-gradient dependent thermophoretic force to investigate a particle's motion in the HDI between a TFC slider and a disk where a non-uniform temperature field exists due to temperature difference between the slider and the disk, with application to particle contamination on a TFC slider. By using numerical simulation to calculate a particle's trajectory and using theoretical analysis, we show that the thermophoretic force is always negligible compared to the Saffman lift force, which points to a direction parallel to the thermophoretic force. We conclude that numerical results, for example, particle contamination profile on the ABS, obtained from the current particle contamination simulator without any thermophoretic forces included would not be significantly altered by the inclusion of these forces.

The temperature inside modern HDDs can arise to as high as 100°C during operation. Chapter 6 investigates the effects of such a high temperature on the slider's flying attitude and the shear forces on the slider and the disk. An analytical formula for the shear force is derived for an arbitrarily rarefied gas. This formula happens to have the same form as that derived from the continuum theory with the first order slip boundary condition, which validates previous studies based on the latter formula. The generalized Reynolds equation is modified to take into account the temperature effect on the mean free path as well as the viscosity. Numerical results are obtained for two different ABS designs. It is shown that the temperature increase results in non-negligible changes in the slider's flying height and the shear forces. These changes could further induce changes in the deformation and instability of the lubricant layer and thereby affect the reliability of the hard disk drives.

Thermal flying-height control (TFC) sliders have been recently introduced into in commercial HDDs to increase the HDDs' capacity and reliability. The design of this new class of sliders depends on the numerical prediction of their flying performance, which requires a model for heat flux on the TFC slider's ABS. The currently used heat flux model is based on a first order slip theory and is believed to lack sufficient accuracy due to its limitation of applicability. Chapter 7 proposes a new model for the heat flux, which considers both the heat conduction and viscous dissipation. The predicted heat conduction by the new model shows better agreement with numerical results of the linearized Boltzmann equation than existing models derived from the temperature jump theory. The viscous dissipation of plane Couette flow as well as that of plane Poiseuille flow in the gas film is analyzed using the energy conservation equation instead of the linearized Boltzmann equation, which is incapable of calculating the viscous dissipation at the boundaries. The new model gives simple analytical expressions for the heat flux contributed by heat conduction and viscous dissipation, and it shows that heat conduction dominates the heat flux. It is found that the numerical results for a TFC slider's flying performance based on the current model have a relative error less than 10% for state-of-art sliders, and, thus, the currently used model is sufficiently accurate.

Filling hard disk drives with air-helium gas mixtures instead of pure air or pure helium can balance performance improvement, such as reduced power cost, increased capacity and

improved reliability, against cost increase. Chapter 8 employs established approaches to calculate the physical properties of the air-helium gas mixtures and proposes a consistent approach to investigate a TFC slider's flying performance in these environments. It is found that at a fixed heater power the slider's flying height first increases and then decreases with the helium content in the gas mixture due to the combined effects of changes in the mean free path, viscosity and thermal conductivity of the gas mixture with helium content. It is shown that the smallest power required for a designated flying height appears when the gas mixture is composed of about half helium and half air. These findings together with the proposed approach are useful for future designs of sliders in air-helium mixtures, and the proposed numerical approach can also find application in investigating a slider's flying performance in a humid environment.

Bibliography

K. Aoki and T. Watanabe. Nonlinearity of thermal spacing control in hard disk drives. *IEEE Trans. Magn.*, 45:816–821, 2009.

K. Aruga, M. Suwa, K. Shimizu, and T. Watanabe. A study on positioning error caused by flow induced vibration using helium-filled hard disk drives. *IEEE Trans. Magn.*, 43: 3750–3755, 2007.

P. Bassanini, C. Cercignani, and C. D. Pagani. Influence of the accommodation coefficient on the heat transfer in a rarefied gas. *Int. J. Heat Transfer*, 11:1359–1369, 1968.

A. B. Basset. *A Treatise on Hydrodynamics*. Deighton, Bell and Co., Cambridge, UK, 1888.

G. K. Batchelor. *An Introduction to Fluid Dynamics*. Cambridge University Press, Cambridge, UK, 1967.

P. L. Bhatnagar, E. P. Gross, and M. Krook. A model for collision processes in gases. I. Small amplitude processes in charged and in neutral one-component systems. *Phys. Rev.*, 94:511–525, 1954.

G. A. Bird. *Molecular Gas Dynamics and the Direct Simulation of Gas Flows*. Oxford University Press, New York, 1994.

G. A. Bird. The DS2V/3V program suite for DSMC calculations. In M. Capitelli, editor, *Rarefied Gas Dynamcis: 24th Internatioinal Symposium*, pages 541–546, New York, 2005. AIP.

K. I. Borg, L. H. Söderholm, and H. Essén. Force on a spinning sphere moving in a rarefied gas. *Phys. Fluids*, 15:736–741, 2003.

J. R. Brock. On the theory of thermal forces acting on aerosol particles. *J. Colloid Sci.*, 17: 768–780, 1962.

A. Burgdorfer. The influence of the molecular mean free path on the performance of hydrodynamic gas lubricated bearing. *ASME J. Basic Engn.*, 81:94–100, 1959.

G. W. Burr, B. N. Kurdi, J. C. Scott, C. H. Lam, K. Gopalakrishnan, and R. S. Shenoy. Overview of candidate device technologies for storage-class memory. *IBM J. Res. & Dev.*, 52:449–464, 2008.

C. Cercignani. *Rarefied Gas Dynamics: From Basic Concepts to Actual Calculations*. Cambridge University Press, New York, 2000.

C. Cercignani, C. D. Pagani, and P. Bassanini. Flow of a rarefied gas past an axisymmetric body. II. Case of a sphere. *Phys. Fluids*, 11:1399–1403, 1968.

E. Cha, C. Chiang, J. Enguero, and J. J. K. Lee. Effect of temperature and attitude on flying height. *IEEE Trans. Magn.*, 32:3729–3731, 1996.

D. Chen and D. B. Bogy. A comparison of two rarefaction models in the compressible Reynolds equation used in air bearing design for hard disk drives. CML Technical Report 2005-10, Computer Mechanics Laboratory, Department of Mechanical Engineering, University of California, Berkeley, 2005.

D. Chen, N. Liu, and D. B. Bogy. A phenomenological heat transfer model for the molecular gas lubrication system in hard disk drives. *J. Appl. Phys.*, 105:084303, 2009.

L. Chen, D. B. Bogy, and B. Strom. Thermal dependence of MR signal on slider flying state. *IEEE Trans. Magn.*, 36:2486–2489, 2000.

B. J. Cox and D. B. Bogy. The CML Air Bearing Design program (CMLAir), Version 7 User Manual. CML Technical Report 2007-12, Computer Mechanics Laboratory, Department of Mechanical Engineering, University of California, Berkeley, 2007.

R. G. Cox and S. K. Hsu. The lateral migration of solid particles in a laminar flow near a plane. *Int. J. Multiphas Flow*, 3:201–222, 1977.

Q. Dai, R. E. Knigge, R. J. Waltman, and B. Marchon. Time evolution of lubricant-slider dynamic interactions. *IEEE Trans. Magn.*, 39:2459–2461, 2003.

Q. Dai, F. Hendriks, and B. Marchon. Modeling the washboard effect at the head/disk interface. *J. Appl. Phys.*, 96:696–703, 2004.

A. Dubinsky and T. Elperin. Comment on "Force on a spinning sphere moving in a rarefied gas" and "On the inverse Magnus effect in free molecular flow". *Phys. Fluids*, 16:3832–3832, 2004.

P. S. Epstein. On the resistance experienced by spheres in their motion through gases. *Phys. Rev.*, 23:710–733, 1924.

R. F. Freitas and W. W. Wilcke. Storage-class memory: the next storage system technology. *IBM J. Res. & Dev.*, 52:439–447, 2008.

S. Fukui and R. Kaneko. Analysis of ultra-thin gas film lubrication based on linearized Boltzmann equation (influence of accommodation coefficient). *JSME Int. J.*, 30:1660–1666, 1987.

S. Fukui and R. Kaneko. Analysis of ultra-thin gas film lubrication based on linearized Boltzmann equation: First report–Derivation of a generalized lubrication equation including thermal creep flow. *ASME J. Trib.*, 110:253–261, 1988.

S. Fukui and R. Kaneko. A database for interpolation of Poiseuille flow-rates for high Knudsen number lubrication problems. *ASME J. Trib.*, 112:78–83, 1990.

S. Fukui and K. Yamane. DSMC/MGL comparison of stresses on slider air bearing with nanometer spacings. *IEEE Trans. Magn.*, 38:2153–2155, 2002.

P. Ganatos, S. Weinbaum, and R. Pfeffer. A strong interaction theory for the creeping motion of a sphere between plane parallel boundaries. Part I. Perpendicular motion. *J. Fluid Mech.*, 99:739–753, 1980.

A. J. Glodman, R. G. Cox, and H. Brenner. Slow viscous motion of a sphere parallel to a plane wall–I. Motion through a quiescent fluid. *Chem. Eng. Sci.*, 22:637–651, 1967.

E. Grochowski and R. D. Halem. Technological impact of magnetic hard disk drives on storage systems. *IBM Systems J.*, 42:338–346, 2003.

A. Guha. Transport and deposition of particles in turbulent and laminar flow. *Ann. Rev. Fluid Mech.*, 40:311–341, 2008.

S. Gurumurthi, A. Sivasubramaniam, M. Kandemir, and H. Franke. Reducing disk power consumption in servers with DRPM. *IEEE Computer*, 36:59–66, 2003.

J. Happel and H. Brenner. *Low Reynolds Number Hydrodynamics*. Martinus Nijhoff, The Hague, Netherlands, 1983.

J. M. Harker, D. W. Brede, R. E. Pattison, G. R. Santana, and L. G. Taft. A quarter century of disk file innovation. *IBM J. Res. Develop.*, 25:677–689, 1981.

HGST. http://www.hgst.com/hdd/research, 2010.

Y. T. Hsia and G. A. Domoto. An experimental investigation of molecular rarefaction effects in gas lubricated bearings at ultra-low clearances. *ASME J. Lub. Tech.*, 105:120–130, 1983.

ANSYS Inc. *ANSYS 11.0 User's Manual*, 2007.

INSIC. http://www.insic.org, 2010.

J. N. Israelachvili. *Intermolecular and Surface Forces*. Academic Press, New York, 2nd edition, 1992.

S. G. Ivanov and A. M. Yanshin. Forces and moments acting on bodies rotating about a symmetry axis in a free molecular flow. *Fluid Dynamics*, 15:449–453, 1980.

D. P. Johns, J. J. Pretto, and J. A. Streeton. Measurement of gas viscosity with a Fleisch pneumotachograph. *J. Appl. Physiol.*, 53:290–293, 1982.

Y. S. Ju. Thermal conduction and viscous heating in microscale Couette flows. *ASME J. Heat Transfer*, 122:817–818, 2000.

J. Y. Juang and D. B. Bogy. Air-bearing effects on actuated thermal pole-tip protrusion for hard disk drives. *ASME J. Trib.*, 129:570–578, 2007.

J. Y. Juang, D. Chen, and D. B. Bogy. Alternate air bearing slider designs for areal density of 1Tb/in^2. *IEEE Trans. Magn.*, 42:241–246, 2006.

J. Y. Juang, T. Nakamura, B. Knigge, Y. S. Luo, W.-C. Hsiao, K. Kuroki, F.-Y. Huang, and P. Baumgart. Numerical and experimental analyses of nanometer-scale flying height control of magnetic head with heating element. *IEEE Trans. Magn.*, 44:3679–3682, 2008.

S. C. Kang, R. M. Crone, and M. S. Jhon. A new molecular gas lubrication theory suitable for head-disk interface modeling. *J. Appl. Phys.*, 85:5594–5596, 1999.

S. Kim and S. J. Karrila. *Microhydrodynamics*. Dover, New York, 2005.

M. K. Kogan. *Rarefied Gas Dynamics*. Plenum Press, New York, 1969.

K. Kouno, A. Aoyagi, K. Ichikawa, and T. Nakamiya. Manufacturing method of hermetic connection terminal used in a disk drive device having hermetically sealed enclosure and disk drive device. U.S. Patent No. 2009/0168233 A1, July 2009.

K. Koura and H. Matsumoto. Variable soft sphere molecular model for inverse-power-law or Lennard-Jones potentail. *Phys. Fluids A*, 3:2459–2465, 1991.

K. Koura and H. Matsumoto. Variable soft sphere molecular model for air species. *Phys. Fluids A*, 4:1083–1085, 1992.

M. Kröger and M. Hütter. Unifying kinetic approach to phoretic forces and torques onto moving and rotating convex particles. *J. Chem. Phys.*, 125:044105, 2006.

M. K. Kryder and C. S. Kim. After hard drives–What comes next? *IEEE Trans. Magn.*, 45:3406–3413, 2009.

H. Kubotera and D. B. Bogy. Effect of various physical factors on thin lubricant film migration on the flying head slider at the head-disk interface of hard disk drives. *J. Appl. Phys.*, 102:054309, 2007.

M. Kurita and K. Suzuki. Flying-height adjustment technologies of magnetic head sliders. *IEEE Trans. Magn.*, 40:332–336, 2004.

H. Lamb. *Hydrodynamics*. Dover, New York, 1945.

E. Lauga, M. P. Brenner, and H. A. Stone. Microfluidics: The non-slip boundary condition. In C. Tropea, J. Foss, and A. Yarin, editors, *Handbook of Experimental Fluid Dynamics*, New York, 2007. Springer-Verlag.

L. Lees. Kinetic theory description of rarefied gas flow. *J. Soc. Ind. Appl. Math.*, 12:278–311, 1965.

D. Legendre and J. Magnaudet. A note on the lift force on a spherical bubble or drop in a low-Reynolds-number shear flow. *Phys. Fluids*, 9:3572–3574, 1997.

E. W. Lemmon, R. T. Jacobsen, S. G. Penoncello, and D. G. Friend. Thermodynamic properties of air and mixtures of nitrogen, argon, and oxygen from 60 to 2000K at pressures to 2000MPa. *J. Phys. Chem. Ref. Data*, 29:331–385, 2000.

H. Li, C.-T. Yin, and F. E. Talke. Thermal insulator design for optimizing the efficiency of thermal flying height control sliders. *J. Appl. Phys.*, 105:07C122, 2009.

Z. Li and H. Wang. Drag force, diffusion coefficient, and electric mobility of small particles. I. Theory applicable to the free-molecule regime. *Phys. Rev. E*, 68:061206, 2003a.

Z. Li and H. Wang. Drag force, diffusion coefficient, and electric mobility of small particles. I. Application. *Phys. Rev. E*, 68:061207, 2003b.

D. R. Lide. *CRC Handbook of Chemistry and Physics*. CRC Press, Boca Raton, FL, 2008.

B. Liu, J. Yu, and S. A. Rice. Direct measurements of constrained Brownian motion of an isolated sphere between two walls. *Phys. Rev. E*, 62:3909–3919, 2000.

C. Y. Liu and L. Lees. Kinetic theory description of plane compressible Couette flow. In L. Talbot, editor, *Rarefied Gas Dynamics*, pages 391–428, New York, 1961. Academic Press.

N. Liu and D. B. Bogy. Forces on a rotating particle in a shear flow of a highly rarefied gas. *Phys. Fluids*, 20:107102, 2008.

N. Liu and D. B. Bogy. Boundary effect on particle motion in the head disk interface. *Tribol. Letters*, 33:21–27, 2009a.

N. Liu and D. B. Bogy. Tempearture effect on a HDD slider's flying performance. *Tribol. Letters*, 35:105–112, 2009b.

N. Liu and D. B. Bogy. Air bearing shear force in the head-disk interface of hard disk drives. *Tribol. Letters*, 35:121–125, 2009c.

N. Liu and D. B. Bogy. Particle contamination on a thermal flying-height control (TFC) slider. *Tribol. Letters*, 37:93–97, 2010.

N. Liu, J. Zheng, and D. B. Bogy. Forces on a spherical particle with an arbitrary axis of rotation in a weak shear flow of a highly rarefied gas. *Phys. Fluids*, 21:047102, 2009a.

N. Liu, J. Zheng, and D. B. Bogy. Thermal flying-height control sliders in hard disk drives filled with air-helium gas mixtures. *Appl. Phys. Lett.*, 95:213505, 2009b.

N. Liu, J. Zheng, and D. B. Bogy. Predicting the flying height of a thermal flying-height control slider in operation. *J. Appl. Phys.*, 2010a. in press.

N. Liu, J. Zheng, and D. B. Bogy. Thermal flying-height control sliders in hard disk drives. CML Technical Report 2010-01, Computer Mechanics Laboratory, Department of Mechanical Engineering, University of California, Berkeley, 2010b.

N. Liu, J. Zheng, and D. B. Bogy. Thermal flying-height contrl sliders in air-helium gas mixtures. CML Technical Report 2010-02, Computer Mechanics Laboratory, Department of Mechanical Engineering, University of California, Berkeley, 2010c.

V. C. Liu, S. C. Pang, and J. Howard. Sphere drag in flows of almost-free molecules. *Phys. Fluids*, 8:788–796, 1965.

L. Lobry and N. Ostrowsky. Diffusion of Brownian particles trapped between two walls: Theory and dynamic-light-scattering measurements. *Phys. Rev. B*, 53:12050–12056, 1996.

D. A. Lockerby, J. M. Reese, D. R. Emerson, and R. W. Barber. Velocity boundary condition at solid walls in rarefied gas calculations. *Phys. Rev. E*, 70:017303, 2004.

E. Loth. Lift of a solid spherical particle subject to vorticity and/or spin. *AIAA J.*, 46: 801–809, 2008.

S. Lu. *Numerical Simulation of Slider Air Bearings*. PhD thesis, Department of Mechanical Engineering, University of California, Berkeley, 1997.

Y. Ma and B. Liu. Lubricant transfer from disk to slider in hard disk drives. *Appl. Phys. Lett.*, 90:143516, 2007.

B. Marchon, Q. Dai, V. Nayak, and R. Pit. The physics of disk lubricant in the continuum picture. *IEEE Trans. Magn.*, 41:616–620, 2005.

C. M. Mate and B. Marchon. Shear response of molecularly thin liquid films to an applied air stress. *Phys. Rev. Lett.*, 85:3902–3905, 2000.

M. R. Maxey. The equation of motion for a small rigid sphere in a nonuniform unsteady flow. *ASME FED*, 166:57–62, 1993.

M. R. Maxey and J. J. Riley. Equation of motion for a small rigid sphere in a nonuniform flow. *Phys. Fluids*, 26:883–889, 1983.

J. B. McLaughlin. Inertial migration of a small sphere in linear shear flows. *J. Fluid Mech.*, 224:261–274, 1991.

D. W. Meyer, P. E. Kupinski, and J. C. Liu. Slider with temperature responsive transducer positioning. U.S. Patent No. 5,991,113, Nov. 1999.

Y. Mitsuya. Modified Reynolds equation for ultra-thin film gas lubrication using 1.5-order slip-flow model and considering surface accommodation coefficient. *ASME J. Trib.*, 115: 289–294, 1993.

J. B. Money. Hermetically sealed mobile hard disk drive utilizing a base made of a ceramic substrate. U.S. Patent No. 7,042,675 B2, May 2006.

PCGuide. http://www.pcguide.com/ref/hdd/op/index-c.html, 2010.

Y. Peng, X. Lu, and J. Luo. Nanoscale effect on ultrathin gas film lubrication in hard disk drive. *ASME J. Trib.*, 126:347–352, 2004.

B. E. Poling, J. M. Prausnitz, and J. O'Connell. *The Properties of Gases and Liquids*. McGraw-Hill, New York, 5th edition, 2001.

O. Reynolds. On the theory of lubrication and its application to Mr. Beauchamp Tower's experiments, including an experimental determination of the viscosity of olive oil. *Phil. Trans.*, 177:157–234, 1886.

S. I. Rubinow and J. B. Keller. The transverse force on spinning spheres moving in a viscous liquid. *J. Fluid Mech.*, 11:447–459, 1961.

P. G. Saffmann. The lift force on a small sphere in a slow shear flow. *J. Fluid Mech.*, 22: 385–400, 1965.

I. Sata, K. Otani, S. Oguchi, and K. Hoshiya. Characteristics of heat transfer in helium-filled disk enclosures. *IEEE Trans. CHMT*, 11:571–575, 1988.

M. A. Scarpulla, C. M. Mate, and M. D. Carter. Air shear driven flow of thin perfluoropolyether polymer films. *J. Chem. Phys.*, 118:3368–3375, 2003.

S. A. Schaaf and P. L. Chambré. *Flow of Rarefied Gases*. Princeton University Press, 1961.

S. Shen and G. Chen. A kinetic theory analysis on the heat transfer in hard drive air bearing. *J. Appl. Phys.*, 103:054304, 2008.

X. J. Shen and D. B. Bogy. Particle flow and contamination in slider air bearings for hard disk drivers. *ASME J. Trib.*, 125:358–363, 2003.

X. J. Shen, M. Suk, and D. B. Bogy. Study of transverse flow effects on particle flows and contamination of air bearing sliders. *ASME J. Trib.*, 126:745–750, 2004.

F. S. Sherman. A survey of experimental results and methods for the transition regime of rarefied gas dynamics. In C.L. Brundin, editor, *Rarefied Gas Dynamics*, volume II, pages 228–260, New York, 1963. Academic Press.

Y. Shiroishi, K. Fukuda, I. Tagawa, H. Iwasaki, S. Takenoiri, H. Tanaka, H. Mutoh, and N. Yoshikawa. Future options for hdd storage. *IEEE Trans. Magn.*, 45:3816–3822, 2009.

Y. Sone. *Molecular Gas Dynamics: Theory, Techniques, and Applications*. Birkhäuser, Boston, 2006.

G. S. Springer. Heat transfer in rarefied gases. In J. P. Hartnett and T. F. Irvine Jr., editors, *Advances in Heat Transfer*, volume 7, pages 163–218, New York, 1971. Academic Press.

L. D. Stevens. The evolution of magnetic storage. *IBM J. Res. Develop.*, 25:663–675, 1981.

H. Suzuki, T. Nakamiya, and T. Kouno. Data storage device. U.S. Patent No. 2009/0097163 A1, April 2009.

L. Talbot, R. K. Cheng, R. W. Schefer, and D. R. Willis. Thermophoresis of particles in a heated boundary layer. *J. Fluid Mech.*, 101:737–758, 1980.

Y. Tang, S. Y. Hong, N. Y. Kim, and X. Che. Overview of flying height control applications in perpendicular magnetic recording. *IEEE Trans. Magn.*, 43:709–714, 2007.

K. Uefune, T. Hayakawa, Y. Hirono, and M. Muranishi. Manufacturing method of base and manufacturing method of disk drive device. U.S. Patent No. 2009/0241322 A1, Oct. 2009.

M. Van Dyke. *Perturbation Methods in Fluid Mechanics*. The Parabolic Press, Stanford, CA, annoted edition, 1975.

W. G. Vincenti and C. H. Kruger. *Introduction to Physical Gas Dynamics*. Wiley, New York, 1965.

L. Waldmann. On the motion of spherical particles in nonhomogeneous gases. In L. Talbot, editor, *Rarefied Gas Dynamics*, pages 323–344, New York, 1961. Academic Press.

R. L. Wallace. The reproduction of magnetically recorded signals. *Bell Syst. Tech. J.*, 30: 1145–1173, 1951.

C.-T. Wang. Free molecular flow over a rotating sphere. *AIAA J.*, 10:713–714, 1972.

M. Wang and Z. Li. Mirco- and nanoscale non-ideal gas poiseuille flows in a consistent Boltzmann algorithm model. *J. Micromech. Microeng.*, 14:1057–1063, 2004.

P. D. Weidman and A. Herczynski. On the inverse Magnus effect in free molecular flow. *Phys. Fluids*, 16:L9–L12, 2004.

Wikipedia. http://en.wikipedia.org/wiki/Early_IBM_disk_storage#IBM_350, 2010.

R. Wood. Future hard disk drive systems. *J. Magn. Magn. Mater.*, 321:555–561, 2009.

L. Wu. Lubricant dynamics under sliding condition in disk drives. *J. Appl. Phys.*, 100: 024505, 2006a.

L. Wu. A two-dimensional model for the interaction between lubricant droplet on the slider surface and air flow within the head/disk interface of disk drives. *J. Appl. Phys.*, 99: 08N101, 2006b.

J. Yang, C. P. Tan, and E. H. Ong. Thermal analysis of helium-filled enterprise disk drive. *Microsyst. Technol.*, 2009. Submitted.

S. Zhang and D. B. Bogy. Effects of lift force on the motion of particles in the recessed regions of a slider. *Phys. Fluids*, 9:1265–1272, 1997a.

S. Zhang and D. B. Bogy. Motion of particles in a slider/disk interface including lift force and wall effect. *IEEE Trans. Magn.*, 33:3166–3168, 1997b.

S. Zhang and D. B. Bogy. A heat transfer model for thermal fluctuation in a thin slider/disk air bearing. *Int. J. Heat Mass Transfer*, 42:1791–1800, 1999.

S. Zhang, S.-C. Lee, D. Kim, J. Ferber, B. Strom, and G. Tyndall. Air bearing surface designs in consideration of thermo-mechanical actuation efficiency. *ASME J. Trib.*, 130: 041901, 2008a.

S. Zhang, B. Strom, S. C. Lee, and G. Tyndall. Simulating the air bearing pressure and flying height in a humid environment. *ASME J. Trib.*, 130:011008, 2008b.

J. Zheng and D. B. Bogy. Thermal fly-height control (TFC) code user's manual. CML Technical Report 2009-06, Computer Mechanics Laboratory, Department of Mechanical Engineering, University of California, Berkeley, 2009a.

J. Zheng and D. B. Bogy. Effects of altitude on the thermal flying height actuation. CML Technical Report 2009-08, Computer Mechanics Laboratory, Department of Mechanical Engineering, University of California, Berkeley, 2009b.

W. D. Zhou, B. Liu, S. K. Yu, and W. Hua. Inert gas filled head-disk interface for future extremely high density magnetic recording. *Tribol. Letters*, 23:179–186, 2009.